

AN ABSTRACT OF THE THESIS OF

Michael Matthews Hall for the degree of Doctor of Philosophy in Chemistry presented on July 31, 1996. Title: A Search for New Substrate Materials for High Temperature Superconducting Thin Films.

Abstract Approved: Redacted for Privacy
Arthur W. Sleight

Three approaches to the development of new substrate materials for high temperature superconducting thin films have been investigated, and the results are described. Films of mixed perovskites were grown on MgO as buffer layers, Sr was substituted into LaAlO₃ in an attempt to transform the symmetry from rhombohedral to cubic, and syntheses of new oxyfluoride perovskites were attempted. The films and compounds synthesized exhibit desirable substrate properties, and the methods employed for synthesis are suitable for larger scale production.

Thin films of Sr₂GaTaO₆ (SGT) and Sr₂AlTaO₆ (SAT) were grown epitaxially on a (100) MgO substrate by RF magnetron sputtering. The morphology of these films as a function of sputtering variables was investigated with SEM and AFM, and the crystallinity characterized by x-ray diffraction 2θ and φ scans. Thin films of SGT and SAT were deposited on a LaAlO₃ substrate/YBa₂Cu₃O_{7-x} (YBCO) film structure to investigate the effects of these materials on superconductor performance. On and off-axis sputtered SGT was found to grow epitaxially on YBCO. The on-axis SGT film protected YBCO from chemical etching. T_c of the

superconductor was ~80K after on-axis SGT deposition, and ~87K after off-axis deposition.

Systematic changes in the structure of rhombohedral (space group $R\bar{3}c$) compounds in the solid solution $(La_{1-x}Sr_x)AlO_{3-y}$ ($x=0-0.35$) were studied by powder x-ray diffraction. The unit cell and fractional atomic coordinates were found to move closer to cubic symmetry from Rietveld refinements of x-ray diffraction patterns. Materials appeared to be metrically cubic at $x=.25$ by x-ray diffraction. Neutron diffraction however, showed the compound to remain rhombohedral at this stoichiometry.

Syntheses of the compounds A_2MgBO_5F ($A=Ca, Sr, Ba; B=Nb, Ta$) were attempted to prepare new perovskites with similar lattice constants to common high temperature superconductors. Single phase products in the Ba/Mg/Nb/O/F and Ba/Mg/Ta/O/F systems were obtained, were found to crystallize in space group $Pm\bar{3}m$, and to be intermediate in composition between the target .5Mg/.5B cation ratios and the known compounds $BaMg_{.33}Nb_{.66}O_3$ and $BaMg_{.33}Ta_{.66}O_3$.

**A Search for New Substrate Materials for High Temperature
Superconducting Thin Films**

by

Michael Matthews Hall

A THESIS

submitted to

Oregon State University

**in partial fulfillment of
the requirements for the
degree of**

Doctor of Philosophy

**Presented July 31, 1996
Commencement June 1997**

Doctor of Philosophy thesis of Michael Matthews Hall presented on July 31, 1996

APPROVED:

Redacted for Privacy

Major Professor, representing Chemistry

Redacted for Privacy

Chair of Department of Chemistry

Redacted for Privacy

Dean of Graduate School

I understand that my thesis will become part of the permanent collection of Oregon State University libraries. My signature below authorizes release of my thesis to any reader upon request.

Redacted for Privacy

Michael Matthews Hall, Author

ACKNOWLEDGMENT

Though I held the primary responsibility of ensuring that the work presented in this thesis proceeded in a timely manner, I could not have finished without the help and support of many others who each contributed to the effort in one way or another. I would like to take this opportunity to acknowledge with great appreciation those whose assistance was particularly important in helping me achieve this end.

My advisor, Dr. Arthur W. Sleight, who, through his generous support, guidance, and ideas gave me the opportunity to earn this degree.

Dr. Laura L. H. King, for giving me a great start on my graduate studies, and for her assistance in helping me on my various projects.

Dr. John S. O. Evans, for his patience, candor in editing, and generosity with his time.

Pat Woodward and Dr. Seung-Tae Hong for all of the assistance in the lab, computer support, and patience with my many questions.

The rest of the Sleight research group, past and present, for their friendship and help: Dr. Ruiping Wang, Dr. Richard Mackey, Dr. Mark Kennard, Dr. Mary Thundathil, Dr. Vince Korthuis, Dr. Phong Nguyen, Dr. Sasirehka Kodialam, Paul Bacon, Maddy Thangaraju, Ivana Radosavljevic, and Ju-Zhou Tao.

My family, whom I love, for dealing so well with my desire to live so far away from home.

And Ellen, for making the writing of this thesis so much more bearable.

TABLE OF CONTENTS

	<u>Page</u>
1. Introduction to Research	1
1.1 Introduction	1
1.2 References	28
2. $A_2BB'O_6$ Double Perovskite Thin Films as Buffer Layers for High Temperature Superconducting Thin Films	32
2.1 Introduction	32
2.2 Experimental	34
2.2.1 RF Magnetron Sputtering	34
2.2.2 Target Preparation	37
2.2.3 Dielectric Thin Film Preparation and Film Analysis	38
2.2.4 Multilayer Film Preparation	40
2.3 Results	41
2.3.1 A_2MgWO_6 Films	41
2.3.2 Sr_2BNbO_6 Films (B=Al, Ga)	45
2.3.3 Sr_2GaTaO_6 Films	50
2.3.3.1 Optimization of Substrate Temperature	50
2.3.3.2 Optimization of Gas Composition	52
2.3.3.3 Effect of MgO Substrate Temperature on SGT Physical Properties	54
2.3.4 Sr_2AlTaO_6 Films	64
2.3.5 $YBa_2Cu_3O_7$ /Double Perovskite Thin Film Multilayer Structures	71
2.4 Discussion	78
2.5 Conclusions	85
2.6 References	87

TABLE OF CONTENTS (Continued)

	<u>Page</u>
3. Structural Studies of the Solid Solution $(La_{1-x}Sr_x)AlO_{3-y}$	88
3.1 Introduction	88
3.2 Experimental.....	94
3.3 Results.....	96
3.4 Discussion	121
3.5 Conclusions	128
3.6 References.....	130
4. Synthesis and Study of Oxyfluoride Perovskites	132
4.1 Introduction	132
4.2 Experimental.....	135
4.3 Results.....	138
4.3.1 X-ray Powder Diffraction Patterns	138
4.3.2 X-ray Powder Refinements	142
4.3.2.1 Ba/Mg/Nb/O/F	142
4.3.2.2 Ba/Mg/Ta/O/F	145
4.3.3.3 Ba/Mg/Nb/O	147
4.3.3.4 Ba/Mg/Ta/O	149
4.4 Discussion	151
4.5 Conclusions	157
4.6 References.....	159
5. Summary.....	161
Bibliography	164
Appendix	169

LIST OF FIGURES

Figure	Page
1.1 (a) The ideal perovskite structure.....	7
1.2 (a) Structure of the oxide superconductors $\text{YBa}_2\text{Cu}_3\text{O}_7$ and (b) $\text{Tl}_2\text{Ba}_2\text{CaCu}_2\text{O}_8$	9
1.3 (a) A schematic of a microstrip transmission line.	18
1.4 The double perovskite structure.	23
2.1 Schematics of (a) on-axis, and (b) off axis sputtering geometries.	36
2.2 X-ray diffraction patterns from (a) a ceramic Sr_2MgWO_6 target and (b) the thin film sample SMW 1 on (100) MgO.	43
2.3 X-ray diffraction patterns from (a) a ceramic Ca_2MgWO_6 target and (b) the thin film sample on (100) MgO.	44
2.4 Small second phase peaks of (a) a CMW film x-ray pattern in comparison with (b) the target material.	46
2.5 X-ray diffraction patterns of (a) a SAN thin film in comparison to (b) the bulk phase.	48
2.6 X-ray diffraction patterns of (a) SGN thin films showing the variation of the film orientation with deposition temperature. ...	49
2.7 X-ray phi scans of SGT 1 (top), 2, 3, and 4, arranged top to bottom.	56
2.8 10 micron x 10 micron area SEM images of (a) SGT 1, (b) SGT 2, (c) SGT 3, and (d) SGT 4.	59
2.9 0.5 micron x 0.5 micron area SEM images of (a) SGT 1, (b) SGT 2, (c) SGT 3, and (d) SGT 4.	60
2.10 AFM images of (a) SGT 1 (vertical scale = 10 nm/division), (b) SGT 2 (20 nm/division), (c) SGT 3 (25 nm/division), and (d) SGT 4 (50 nm/division).	61
2.11 (a) Two-theta x-ray diffraction scan of SGT 2 showing the series of (h00) reflections, and Williamson-Hall plot of (b) SGT 2 film x-ray data.	63

LIST OF FIGURES (Continued)

Figure	Page
2.12 10 micron x 10 micron area SEM images of (a) SAT 1 (650 °C), (b) SAT 2 (675 °C), and (c) SAT 3 (700 °C).	68
2.13 0.5 micron x 0.5 micron area SEM images of (a) SAT 1 (650 °C), (b) SAT 2 (675 °C), and (c) SAT 3 (700 °C).	69
2.14 AFM images of (a) SAT 1 (vertical scale=30 nm/division), (b) SAT 2 (10 nm/division), and (c) SAT 3 (20 nm/division).	70
2.15 SEM photographs of (a) YBCO/SGT 1, (b) YBCO/SGT 2 (both on-axis, and (c) YBCO/SGT 4 (off-axis).	74
2.16 T_c plot of SGT films deposited on a LaAlO_3 substrate/YBCO film structure by (a) on axis and (b) off-axis sputtering.	75
2.17 SEM photographs from YBCO/SGT film etch tests.	76
2.18 Phi-scans of YBCO and SGT (220) peaks showing the growth orientation of the film relative to the substrate for the on-axis (top traces) and off-axis (bottom traces) films.	78
3.1 (a) The rhombohedral unit cell of LaAlO_3 , and (b) the extended structure, showing the similarity to the ideal perovskite structure (given in Figure 1.1).	90
3.2 Two-theta x-ray diffraction scans of the $(42\bar{2})$ and (642) peaks for various compositions of $(\text{La}_{1-x}\text{Sr}_x)\text{AlO}_{3-y}$, demonstrating the decrease in peak splitting as strontium concentration increases.	97
3.3 (a) Plot of the lattice constant and lattice angle vs. strontium concentration in reaction mixture.	99
3.4 (a) Refined Sr concentration vs. x, and (b) Oxygen position vs. x in $(\text{La}_{1-x}\text{Sr}_x)\text{AlO}_{3-y}$	102
3.5 (a) Al-O-Al bond angle and (b) O-Al-O bond angles as a function of x in $(\text{La}_{1-x}\text{Sr}_x)\text{AlO}_{3-y}$	106
3.6 A plot of the (a) La-O and (b) the Al-O bond distances as a function of x in $(\text{La}_{1-x}\text{Sr}_x)\text{AlO}_{3-y}$	108
3.7 Strain in $(\text{La}_{1-x}\text{Sr}_x)\text{AlO}_{3-y}$ crystallites as a function of x.	110

LIST OF FIGURES (Continued)

<u>Figure</u>	<u>Page</u>
3.8 X-ray powder diffraction scans of high angle peaks of $(\text{La}_{1-x}\text{Sr}_x)\text{AlO}_{3-y}$ samples of $x=0, 0.11,$ and $0.35,$ to demonstrate the seemingly cubic symmetry of the $x=0.35$ powder.	113
3.9 Comparisons of calculated and observed peak intensities from Rietveld refinements performed on $\text{La}_{.65}\text{Sr}_{.35}\text{AlO}_{3-y}$ performed in (a) Pm3m, and (b) R-3c (starting from $x=0.17$ values), demonstrating the slight error in the calculated peak intensities for the rhombohedral case.	114
3.10 (a) Observed x-ray powder diffraction pattern from $\text{La}_{.75}\text{Sr}_{.25}\text{AlO}_{3-y},$ and (b) difference patterns from Pm3m (top) and R3c (bottom).	117
3.11 (a) Observed neutron diffraction pattern from $\text{La}_{.75}\text{Sr}_{.25}\text{AlO}_{3-y},$ and (b) difference patterns from Pm3m (top) and R3c (bottom).	119
3.12 Energy level diagram of AlO_6 octahedral network in LaAlO_3 (19).	126
4.1 (a) X-ray powder diffraction patterns of 2Ba/Mg/Nb/O/F and 2Ba/Mg/Nb/O reaction mixtures, showing the similarities between the oxide and oxyfluoride patterns, as well as the slight peak broadening in the oxide (inset).	139
4.2 X-ray powder diffraction patterns for (a) 2Sr/Mg/Ta/O/F and 2Sr/Mg/Ta/O, and (b) 2Ca/Mg/Ta/O/F and 2Ca/Mg/Ta/O. .	141
4.3 Observed (+), calculated (—), and difference (bottom) powder x-ray diffraction patterns of the 2Ba/Mg/Nb/O/F product refinement.	144
4.4 Observed (+), calculated (—), and difference (bottom) powder x-ray diffraction patterns of the 2Ba/Mg/Ta/O/F refinement. .	145
4.5 Observed (+), calculated (—), and difference (bottom) powder x-ray diffraction patterns generated from 2Ba/Mg/Nb/O reaction product.	147
4.6 Observed (+), calculated (—), and difference (bottom) powder x-ray diffraction patterns generated from 2Ba/Mg/Ta/O reaction product.	149

LIST OF TABLES

<u>Table</u>	<u>Page</u>
1.1 Some compounds used or suggested for use as substrate materials for HTSC thin films (common HTSC compounds included for comparison).	4
1.2 Physical Properties of the Most Commonly Used Substrates	11
1.3 Physical Properties of Double Perovskites	24
2.1 Deposition Conditions for Sr ₂ MgWO ₆ and Ca ₂ MgWO ₆ Thin Films	42
2.2 Deposition Conditions for Sr ₂ AlNbO ₆ and Sr ₂ GaNbO ₆ Thin Films	47
2.3 X-Ray Diffraction and Composition Data for SGT Film Temperature Optimization Depositions	51
2.4 Results of Sputtering Gas Optimization Studies	53
2.5 Substrate Temperature and X-Ray Analysis for SGT 1-4	54
2.6 Film Thickness Data for SGT 1-4	55
2.7 Film Composition Data for SGT 1-4	56
2.8 Statistics from SEM Images of SGT 1-4	59
2.9 Growth Conditions and X-Ray Peak Analysis for SAT Films	65
2.10 Electron Microprobe Analysis Data for SAT Films	66
2.11 Statistics form SEM Images of SAT 1, 2, and 3	67
2.12 Growth Conditions and Results of LaAlO ₃ / YBa ₂ Cu ₃ O ₇ /SGT and SAT Thin Film Multilayers (x=2.5 inches except where noted)	72
2.13 Predicted Polarizabilities and Dielectric Constants of Sr ₂ BB' O ₆ Double Perovskites (B=Al, Ga; B'=Nb, Ta).....	80
3.1 Refined Lattice Parameters for (La _{1-x} Sr _x)AlO _{3-y}	98
3.2 Fractional and Positional Variables, and Refinement Statistics, for (La _{1-x} Sr _x)AlO _{3-y}	101

LIST OF TABLES (Continued)

<u>Table</u>	<u>Page</u>
3.3 Isotropic Thermal Parameters and Impurity Phase/Phase Fraction for $(\text{La}_{1-x}\text{Sr}_x)\text{AlO}_{3-y}$	104
3.4 Bond Angles as a Function of x in $(\text{La}_{1-x}\text{Sr}_x)\text{AlO}_{3-y}$	105
3.5 Bond Distances as a Function of x in $(\text{La}_{1-x}\text{Sr}_x)\text{AlO}_{3-y}$	107
3.6 Strain Analysis of $(\text{La}_{1-x}\text{Sr}_x)\text{AlO}_{3-y}$	110
3.7 Results of $\text{La}_{.65}\text{Sr}_{.35}\text{AlO}_{3-y}$ X-Ray Refinement in $R\bar{3}c$ and $Pm\bar{3}m$	112
3.8 Results of $\text{La}_{.65}\text{Sr}_{.25}\text{AlO}_{3-y}$ X-Ray Refinement in $R\bar{3}c$ and $Pm\bar{3}m$	116
3.9 Results from Neutron Diffraction Refinement of $\text{La}_{.75}\text{Sr}_{.25}\text{AlO}_{3-y}$	118
3.10 Peaks Visible in Neutron Diffraction Data and Rhombohedral Space Group with No Corresponding Peak in Cubic Space Group	120
4.1 Summary of 2Ba/Mg/Nb/O/F Product Refinements	143
4.2 Atomic Coordinates, Fractional Occupancies, and Thermal Parameters from 2Ba/Mg/Nb/O/F Refinements (Top Table from .5Mg/.5Nb Starting Occupancy, Bottom from EMPA)	143
4.3 Summary of 2Ba/Mg/Ta/O/F Product Refinements	146
4.4 Atomic Coordinates, Fractional Occupancies, and Thermal Parameters from 2Ba/Mg/Ta/O/F Refinements (Top Table from .5Mg/.5Nb Starting Occupancy, Bottom from EMPA)	146
4.5 Summary of 2Ba/Mg/Nb/O Refinements	148
4.6 Atomic Coordinates, Fractional Occupancies, and Thermal Parameters from 2Ba/Mg/Nb/O Refinements (Top Table from .5Mg/.5Nb Starting Occupancy, Bottom from EMPA)	148
4.7 Summary of 2Ba/Mg/Ta/O Refinements	150

LIST OF TABLES (Continued)

<u>Table</u>	<u>Page</u>
4.8 Atomic Coordinates, Fractional Occupancies, and Thermal Parameters from 2Ba/Mg/Ta/O Refinements (Top Table from .5Mg/.5Nb Starting Occupancy, Bottom from EMPA)	150

A Search For New Substrate Materials for High Temperature Superconducting Thin Films

Chapter 1

Introduction to Research

1.1 Introduction

The discovery of high temperature oxide superconductors in the middle and late nineteen eighties (1-6) led to much research on both bulk and thin film applications for these materials. Films in particular were interesting due to the extremely high critical current densities, on the order of 10^6 A/cm², that could be obtained in these materials (7). Work in thin film synthesis soon revealed that the physical properties of the films were greatly dependent upon film quality. In general, single crystal films demonstrated superior normal conductivity and superconductivity in comparison with polycrystalline films. It has been suggested (8) that the suppressed conductivities in the polycrystalline films are probably due to their highly granular morphology, in which good quality superconducting grains are surrounded by material of poorer quality, which may be oxygen deficient, at the boundaries. As a result of these observations, considerable research on how to grow superconducting films of the highest quality has been performed. The best films consist of large grains, leading to fewer grain boundaries, and are epitaxial, which implies that the film grows as a single crystal with a particular crystallographic orientation relative to the substrate, or the material onto which the film is deposited.

Although many different high temperature superconducting oxides have been synthesized and characterized, they can be classified by a small number of general formulas (9). One common class is described by the formula $\text{RBA}_2\text{Cu}_3\text{O}_{7-x}$, where R is a rare earth element, typically yttrium. Another class, of which many members are known, can be represented by the general formula $(\text{AO})_m\text{M}_2\text{Ca}_{n-1}\text{Cu}_n\text{O}_{2n+2}$, where M is barium or strontium, and A is either Bi, Tl, Bi/Tl, Bi/Pb, Tl/Pb, or Hg. The materials of primary interest in applied thin film technology research are $\text{YBa}_2\text{Cu}_3\text{O}_{7-x}$ (or YBCO) and $\text{Tl}_2\text{Ba}_2\text{CaCu}_2\text{O}_8$ (referred to as the TBCCO 2212 phase). YBCO, with a superconducting critical temperature (T_c , or the temperature at which a material transforms from the normal conducting to the superconducting state) of about 95K, is of interest for its high critical current density, and the 2212 TBCCO for its relative ease of synthesis as a thin film and its high T_c of 110K. Many different techniques, such as physical sputtering (10), metal organic chemical vapor deposition (11), thermal coevaporation (12), laser ablation (13,14), and molecular beam epitaxy (15) have been employed to grow films of these materials. For every technique used, studies show that many variables affect the quality of the deposited film. Common variables include substrate temperature, gas pressure, and gas composition in the growth chamber. These are quite different for each technique, and the reasons behind the choice of the best conditions for any technique are purely empirical. For all methods of film growth, however, one factor is well understood and invariant among deposition technologies: a good substrate material is absolutely necessary for the synthesis of a good epitaxial film.

For a substrate material to be a good choice for a given film, it must adhere strictly to a list of desirable physical and chemical properties. If these criteria are not met, films and devices grown and patterned on the substrate may not perform reliably and reproducibly. The substrate should have a good lattice match to the film material (16). The thermal expansion characteristics of the substrate should match those of the film as closely as possible, and the substrate should have no phase transitions between the film synthesis temperature and the device operating temperature. Typical temperatures for film growth range from 700 to over 1100 K, depending on which growth technology is used, and devices made from these films must be operated below the superconducting transition temperature. The substrate lattice should be cubic to minimize the possibility of off-orientation growth and twinning of single crystals or films of the substrate material. The substrate should be chemically inert at elevated temperatures to prevent any unwanted chemical reactions with the components of the growing film. And finally, because the primary application for which these films are being developed is for use in microwave electronics, a material with a low dielectric constant and low dielectric loss at microwave frequencies is necessary to fabricate devices of the highest efficiency.

Many different materials have been either suggested for use as, or tested as, substrate materials, but most of these compounds belong to a narrow range of structural classes. A list of these materials and some of their structural information is given in Table 1.1. Most are of the perovskite structure, which is given in Figure 1.1. The ideal structure is cubic, space group $Pm3m$, and has the general formula ABO_3 , where the total of the oxidation states of the A and B cations is +6. The A cation is

Table 1.1

Some compounds used or suggested for use as substrate materials for HTSC thin films (common HTSC compounds included for comparison).

Compound (and references)	Symmetry	Growth Face Dimension (Å)¹
YBa ₂ Cu ₃ O ₇	Orthorhombic	a=3.84, b=3.88
Tl ₂ Ba ₂ CaCu ₂ O ₈	Tetragonal	a=3.857
Perovskites		
YAlO ₃ (17)	Orthorhombic	3.72
LaAlO ₃ (12,15,19,21)	Rhombohedral	3.79
YbFeO ₃ (18)	Orthorhombic	3.84
NdAlO ₃ (12)	Rhombohedral	3.74
NdGaO ₃ (12,14,19,22)	Orthorhombic	3.87
PrGaO ₃ (20)	Orthorhombic	3.87
LiNbO ₃ (16)	Rhombohedral	3.88
LaGaO ₃ (12,19,21)	Orthorhombic	3.89
SrTiO ₃ (12,19,21,23)	Cubic	3.91
LiBaF ₃ (12)	(?)	3.98
KMgF ₃ (16)	Cubic	3.98
KTaO ₃ (24)	Cubic	3.99
BaTiO ₃ (18)	Tetragonal	3.99
BaZrO ₃ (16)	Cubic	4.18
Mixed Perovskite (25)		
Ca ₂ AlNbO ₆	Orthorhombic	3.82
Ca ₂ AlTaO ₆	Orthorhombic	3.82
Ca ₂ GaNbO ₆	Orthorhombic	3.86
Ca ₂ GaTaO ₆	Orthorhombic	3.86
La ₂ MgGeO ₆	Orthorhombic	3.88
Sr ₂ AlNbO ₆	Cubic	3.897
Sr ₂ AlTaO ₆ (26,27)	Cubic	3.897
Sr ₂ MgMoO ₆	Tetragonal	3.939
Sr ₂ GaNbO ₆	Cubic	3.947
Sr ₂ GaTaO ₆	Cubic	3.949
Ba ₂ YSbO ₆	Cubic	4.21
Binary Compounds		
ZrO ₂ (Y stabilized) (21)	Cubic	3.61
Al ₂ O ₃ (sapphire) (19)	Rhombohedral	3.63
CeO ₂ (film) (28)	Cubic	3.83
SiO ₂ (α-quartz) (16)	Hexagonal	---2

Table 1.1 (continued)

CaF ₂ (16)	Cubic	3.81
MgO (19,21,22,29,30)	Cubic	4.21
Si film/Al ₂ O ₃ (31)	Hexagonal	
MgF ₂ (16)	Tetragonal	a, b = 4.16; c = 3.04
K₂NiF₄ Structure		
NdAlCaO ₄ (14,21,32)	Tetragonal	3.688
LaSrAlO ₄ (33)	Tetragonal	
LaSrGaO ₄ (34)	Tetragonal	3.843
Solid Solutions(35)		
0.7[Sr(Al ₅ Nb _{.5})O ₃] + 0.3(LaAlO ₃)	Cubic	3.86
0.7[Sr(Al ₅ Ta _{.5})O ₃] + 0.3(LaAlO ₃)	Cubic	3.87
0.7[Sr(Al ₅ Nb _{.5})O ₃] + 0.3(NdGaO ₃)	Cubic	3.88
0.7[Sr(Al ₅ Ta _{.5})O ₃] + 0.3(NdGaO ₃)	Cubic	3.89
Other Structures²		
Mg ₂ TiO ₄ (film) (36)	Cubic	4.22
Ba ₂ SiO ₄ (16)	Orthorhombic	
Ca ₂ Al ₂ SiO ₇ (16)	Tetragonal (gehlenite)	
Ca ₂ Ga ₂ SiO ₇ (16)	Tetragonal (gehlenite)	
Y ₃ Fe ₃ Ga ₂ O ₁₂ (16)	Cubic (garnet)	
MgAl ₂ O ₄ (16)	Cubic (spinel)	
LaMgAl ₁₁ O ₁₉ (16)	Hexagonal (magnetoplumbite)	

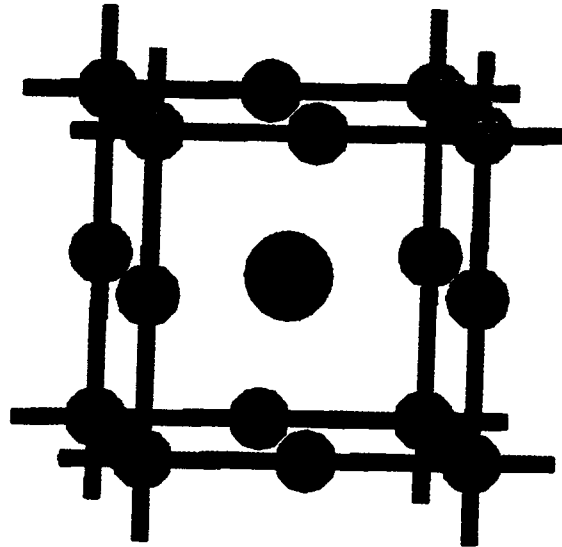
¹The growth face dimension (d) is calculated to give an easy comparison of lattice spacings between the substrate and superconducting materials. This value is not necessarily the lattice constant of a compound. The calculations used to derive these values are as follows. A) Perovskite, orthorhombic, growth face is (110): $d = [(a_0+b_0)/2][1/(2^{1/2})]$. B) Perovskite, rhombohedral, growth face is rhombohedrally indexed (110): $d = a_0/(2^{1/2})$. C) Perovskite, tetragonal and cubic, growth face is (100): $d = a_0$. D) Double Perovskite, orthorhombic, Growth face is (110): $d = [(a_0+b_0)/2][1/(2^{1/2})] / 2$. E) Double Perovskite, tetragonal and cubic, growth face is (100): $d = a_0/2$. F) For binary compounds and the K₂NiF₄ structure, the same calculations have been used as for the simple perovskites. Where no obvious correlation to the simple perovskite structure or the lattice dimensions of the high temperature superconductors exists, the actual lattice constants are given.

²Most of these structures have unit cell dimensions such that no simple correlation to the high temperature superconductor unit cells is possible, yet the periodicity of the lattice still may be suitable to encourage epitaxial growth of films on these materials. Refer to R. Guo *et al* (16) for further information.

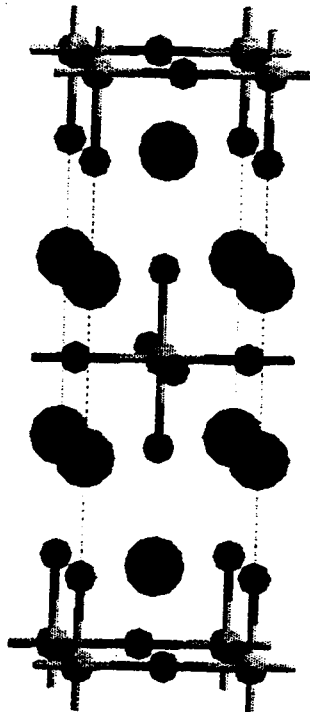
coordinated by 12 oxygens, and is usually in an oxidation state of +1 to +3. The B cation is octahedrally coordinated by oxygen atoms, and generally has an equal or greater oxidation state than the A cation, although exceptions, such as BaLiF_3 , are known. The BO_6 octahedra are corner sharing, and the A cation occupies the interstitial sites in the octahedral framework. A geometrical factor labeled the tolerance factor characterizes the ratio of the distance from the center of the A cation to the edge of the unit cell and the distance from the center of the B cation to the cell edge. It is given by

$$t = \frac{r_a + r_o}{\sqrt{2}(r_b + r_o)} \quad (1.1)$$

where r_a , r_b , and r_o are the ionic radii of the A cation, B cation, and the particular anion (typically oxygen, although others are also common). If the tolerance factor is 1, this implies that all of the ions, if considered to be hard bodies, are just touching in the ideal cubic structure. If the tolerance factor is greater than 1, the A cation is larger, and the oxygen atoms are pushed apart more. This expands the structure, but, if the tolerance factor is not greatly over 1, usually does not result in a new structure. In fact, when considering synthesis of new perovskites, a tolerance factor of between about 1.01 and 1.05 is considered a good indication that the material will be cubic, if synthesis is successful. Above this, a hexagonal instead of cubic structure tends to be adopted. A value below about .975 usually results in a material with an orthorhombic structure. Between .975 and 1.01, the structure is less easy to predict. Some materials in this range are expanded along one of the 3-fold axes in the cubic space group, lowering the symmetry to



(a)



(b)

Figure 1.1 (a) The ideal perovskite structure. (b) K_2NiF_4 , a related structure which has also been investigated for use as a substrate.

rhombohedral. It is also possible for tetragonal and orthorhombic structures to occur in materials with tolerance factors in this range.

The reason for the focus on perovskite substrate materials is the structural similarity between them and the high temperature superconducting oxides. The structures of $\text{YBa}_2\text{Cu}_3\text{O}_7$ and $\text{Tl}_2\text{Ba}_2\text{CaCu}_2\text{O}_8$ are given in Figure 1.2. In the TBCCO compound, the barium and calcium layers are perovskite related. In YBCO, all layers have an approximate perovskite structure, although the yttrium is coordinated by only 8 oxygen atoms. The a-b planes of both structures have similar dimensions as the simple perovskites, although the c axis is greatly expanded. Theoretical structural studies have been performed to model the effect the structure of the substrate has on the epitaxy of a growing YBCO film (16). The conclusions of the study were that, although not independent of each other, similarities in crystal structure between the film and substrate were a more important consideration than just similarities in the unit cell dimensions. Keeping this conclusion in mind, next consider that the superconducting currents in these compounds flow best in the a-b plane. If a film were to grow with the a-b plane normal to the substrate surface, the conductivity in the device plane would be much lower than desired. Therefore, it is necessary to synthesize the superconducting films with the c axis normal to the substrate surface. Because the structure in the a-b plane of both superconductors is that of a perovskite, it is logical to use a perovskite substrate to encourage growth of the film with c-axis orientation. Other common structures related to perovskite, such as the K_2NiF_4 structure, also shown in Figure 1.1, have also been investigated for use as substrates.

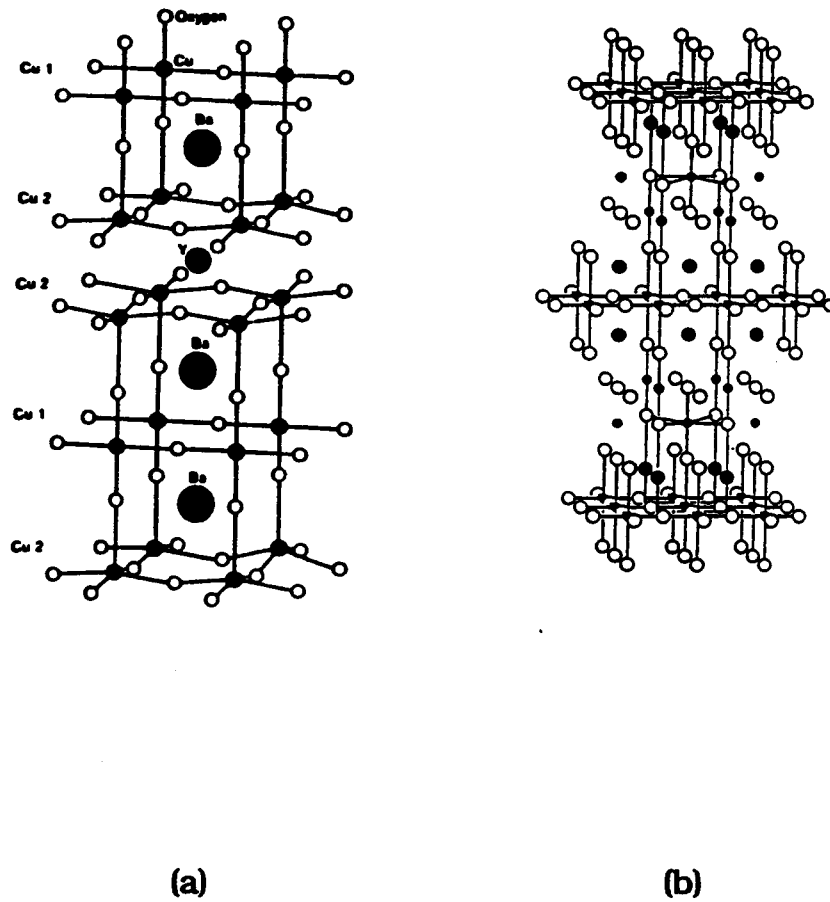


Figure 1.2 (a) Structure of the oxide superconductors $\text{YBa}_2\text{Cu}_3\text{O}_7$ and (b) $\text{Tl}_2\text{Ba}_2\text{CaCu}_2\text{O}_8$. The c axis in both figures is toward the top of the page. The materials have essentially the same periodic structure as the simple perovskites in the a-b plane.

Table 1.2 lists some of the relevant physical properties of the most commonly used substrate materials. All of these materials demonstrate at least some of the desirable properties mentioned above, but also have shortcomings, some of which are severe. Lanthanum gallate, LaGaO_3 , has perhaps the closest lattice match and thermal expansion characteristics to YBCO of any of the materials commonly used. [Other simple perovskites do come closer, such as NdGaO_3 , with $a_0 = 3.85$, but are not used for other reasons, such as reactivity. Films grown on neodymium gallate have extremely poor superconducting properties, possibly due to reactions between the substrate and growing film (12)]. However, a phase transition occurs in lanthanum gallate at 100°C that is accompanied by a sudden volume change in the unit cell. Above this temperature, the material is rhombohedral; below, it is orthorhombic. Films grown on this substrate crack along the substrate pseudocubic (110) and (101) planes upon cooling. The cracks break up the superconducting planes, resulting in grain boundaries and increasing the apparent resistivity of the film.

Magnesium oxide has also been very popular as a substrate. The primary advantages of it are the relative ease with which large single crystals of the material are grown and the low cost of these crystals. Despite the relatively large lattice mismatch of MgO and the superconductors, films grown on MgO have proven to be better than those on more closely geometrically matched substrates. However, they are consistently inferior to films grown on lanthanum aluminate and strontium titanate. Rocking curve studies (see reference 37 for a description of rocking curve analysis) have shown that YBCO grown on MgO possesses poorer orientation normal to the substrate surface than

Table 1.2

Physical Properties of the Most Commonly Used Substrates

Substrate	Growth Face Dimension (Å)¹	$\Delta l / l$ ($\times 10^{-6}/^{\circ}\text{C}$) (YBCO= 11)	Relative Dielectric Constant (ϵ_r)	$\tan\delta$ @ 77K, 10 GHz	Melting Point ($^{\circ}\text{C}$)
ZrO ₂ (+Y ₂ O ₃)	3.63 (-5.5 %)	8-10	29	74.2 e-5	~2715
LaAlO ₃	3.79 (-1.6 %)	~10	23	2 e-5	2726
LaGaO ₃	3.89 (1.1 %)	10.6	25	1.8 e-3 (300K, 1 MHz)	2296
SrTiO ₃	3.91 (1.4 %)	10.4	300	2.1 e-5 (300K)	2626
MgO	4.21 (9.4 %)	8	10	0.62 e-5	2852

¹Dimension of lattice plane closest to that of YBCO (the pseudo-cubic lattice constant for the perovskites), and % difference between this value and YBCO (2212) a-b plane dimensions.

films grown on LaAlO₃ or SrTiO₃ (21). The most likely explanation for this is the difficulty encountered in trying to keep the MgO surface clean and smooth for film deposition. MgO quickly reacts with adsorbed H₂O to form amorphous Mg(OH)₂. This layer can be sputter etched or thermally decomposed prior to the use of the substrate, but these treatments leave behind a pitted or polycrystalline surface nonconductive to the growth of good quality epitaxial films. Small crystallites on the substrate surface may modify the nucleation of, or cause structural defects in, the growing film. Substrates must be stored in an inert liquid (often mineral oil or methanol), cleaned immediately before use, and exposed to the atmosphere minimally while pumping down on the deposition chamber. Despite these precautions, the surface will quickly

be coated with impurities even when under vacuum. A monolayer of adsorbed gas atoms forms on the surface of a solid at a rate of $1 \text{ cm}^2/\text{second}$ at a pressure of 10^{-6} torr. Because it is so difficult to minimize the exposure of a substrate to air before film growth, it is advantageous to use a substrate that is chemically stable in air. Attempts have been made to passivate the MgO surface by a vapor phase reaction with TiO_2 , resulting in the growth of an Mg_2TiO_4 buffer layer (36). The critical temperature (T_c) of YBCO grown on the Mg_2TiO_4 surface was suppressed to 85 K. Most likely, the suppression was due to a residual roughness left in the Mg_2TiO_4 surface, which could have possibly hindered the epitaxial growth of the superconducting film, resulting in grain boundaries. Because the TiO_2 must react with the MgO to form the buffer layer, either Mg must diffuse up through the growing layer, or Ti must diffuse down to the growth interface. Either case is likely to result in new defects, and will not likely correct all of the defects already present on the original MgO surface.

As mentioned previously, the best films are consistently synthesized on either strontium titanate or lanthanum aluminate substrates. Both of these materials are easy to grow as large single crystals, and are readily available commercially in a variety of crystallographic orientations as polished crystals. They are more stable to air exposure than MgO, and have lattice dimensions and thermal expansion characteristics quite close to those of the superconductors. However, even these compounds, the best found to date, have shortcomings that prevent them from being good enough for use in passive microwave circuits, which are the primary applications for which these materials are being developed. To understand why this is the case,

a brief discussion of the dielectric constant and loss tangent, and how they relate to microwave power transmission and passive circuit design, is necessary.

Before introducing the dielectric constant, the definition of a *dielectric* must be given: A dielectric is an electrically insulating or non-conducting medium. The dielectric constant of a material is a quantification of how the dielectric reacts electrically to an applied field. To understand the nature of this reaction, the concept of polarizability must be introduced. All materials contain small charges due to the presence of electrons, ions, and dipoles. When an electric field is applied, these charges react by polarizing along the direction of the field, and the degree of the reaction is described and quantified by the *polarizability* of the material. The polarizability consists of four components, which all have a different frequency response. The long range movement of ions in a crystal, as well as the migration of defects such as low mobility interstitial ions, comprise the *space charge* (α_s) component of the total polarizability. Because of their relatively high mass, these charges cannot respond to a quickly changing electric field. As a result, the space charge component relaxes out of the total polarizability when the applied field reaches radio frequencies. The *dipolar polarizability* (α_d) is the polarization component due to the orientation of permanent dipoles in the structure, such as those present in ferroelectric materials. These relax out at microwave frequencies. The third component of the total polarizability is the *ionic polarizability* (α_i). This is the slight distortion of the structure that results when an applied field moves the ions in the structure slightly off of their lattice positions. In contrast to the space charge polarizability, the ionic polarizability is

the short-range displacement of ions off their ideal lattice sites, rather than longer range migrations. This polarizability relaxes out in the infrared frequency range, leaving the *electronic polarizability* (α_e), or the response of the electron cloud around the atoms or ions in the structure to the applied field, as the only component (38). This continues into x-ray frequencies before finally relaxing out. The *relative dielectric constant*, ϵ_r , of a material is the ratio of the degree of polarization it undergoes in an electric field relative to the polarization of air, and is also known as the relative permittivity. To measure this quantity, one simply measures the charge stored on a set of capacitor plates at a particular voltage and frequency with, and then without, the dielectric material between the plates. The dielectric constant is the ratio of the charged stored on the plates with the dielectric between them to the charged stored without the dielectric, and is related to the polarizability of a material by the Clausius-Mossotti relation

$$\epsilon_r = \frac{V_m + 2\alpha_t b}{V_m - \alpha_t b} \quad (1.2)$$

where V_m is the molar volume in \AA^3 , α_t is the total polarizability due to the ionic and electronic contributions, and b is a geometrical factor, assumed to be $4\pi/3$ for a cubic material (39). From this equation, it is evident that a larger polarizability will result in a higher dielectric constant. R. D. Shannon has compiled a table of ion polarizabilities (40) that allow one to predict the dielectric constant of a new material using this relation and the additivity rule of ion polarizabilities, given below.

$$\alpha(M^{2+}M^{4+}X_3) = \alpha(M^{2+}) + \alpha(M^{4+}) + 3\alpha(X^{2-}) \quad (1.3)$$

The dielectric constant decreases with the relaxation of each contributing term, and is roughly constant as a function of frequency between these regions.

The other dielectric quantity of interest in the field of microwave electronics is called the *loss tangent*, or $\tan\delta$. To understand this quantity, consider the response of the ionic polarizability to an increase in applied field frequency. At lower frequencies, the ions can completely change their polarization state when the field reverses. The polarizations, due to mobile charges in the dielectric, are equivalent to an alternating current flowing in the material. When the field frequency is low enough to permit the ionic polarizations to keep up with the voltage changes, the current due to the polarizations is exactly 90° out of phase with the electric field. The power dissipated as heat as a function of the current and the voltage is

$$P = (1/2) i \cdot v \cos \delta \quad (1.4)$$

where δ is the phase angle. So, at frequencies at which the ionic polarizations can keep up with the field, the vector product is zero, and no power is lost as heat. When the frequency becomes too fast for the polarizabilities to keep up, however, a current component out of phase with the voltage develops, and δ is no longer 90° . Hence, power is lost as heat. The tangent of this angle gives the ratio of power dissipated to power stored in the circuit (41). The lower the value of the loss tangent, the more efficiently the circuit stores or transmits power.

The effect of the dielectric constant on microwave radiation traveling through the dielectric medium is noticed in several ways. First, the wavelength of the radiation is different than the wavelength of

radiation of the same frequency in a vacuum or air. The wavelength in the medium is given by:

$$\lambda = \lambda_o / (\epsilon_{eff})^{1/2} \quad (1.5)$$

where ϵ_{eff} is the effective dielectric constant and takes into account factors such as circuit design. So, with an increase in the relative dielectric constant comes an accompanying decrease in the wavelength of the microwave radiation. Along with the decrease in wavelength is a decrease in the speed of the radiation in the medium relative to that in air or a vacuum. The speed of the signal propagation is also inversely proportional to the square root of the effective dielectric constant.

$$v \propto 1 / (\epsilon_{eff})^{1/2} \quad (1.6)$$

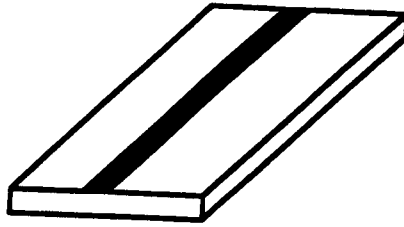
Finally, the frequency of a signal propagating in a non-perfect dielectric medium undergoes dispersion about the central frequency. This dispersion is directly proportional to the square root of the effective dielectric constant.

$$\Delta f \propto \epsilon_r^{1/2} \quad (1.7)$$

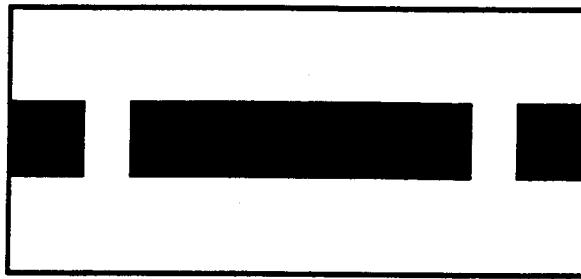
Therefore, a substrate with a relatively high dielectric constant will result in circuits with slower signal propagation and greater signal dispersion relative to those fabricated on a lower dielectric constant medium. For some applications, such as superconducting quantum interference devices (an extremely sensitive detector of magnetic flux), these factors will not cause a degradation in device performance. For passive microwave devices, however, such factors, coupled with the anisotropy of the dielectric constant in non-cubic materials, make the design of reliable devices extremely difficult.

Passive microwave devices are such circuit elements as transmission lines, resonators, and filters. They are referred to as passive because they require no external power supply to operate. Simple schematics of these components are given in Figure 1.3. The transmission line is the most basic structure in microwave circuits. Superconducting transmission lines have resistive losses of ten to one thousand times less than normal conductors, hence the advantage of using a superconductor for these applications (42). Not only do they connect components, but often the components themselves are constructed from some geometrical arrangement of a length of transmission line. Transmission lines in high temperature superconducting circuits are usually composed of microstrip line, which consists of a thin strip of superconducting material, deposited and patterned on top of a dielectric, which has been previously deposited on a conducting ground plane. The circuits are also sometimes constructed of stripline, which is similar to microstrip, but with a dielectric and ground plane both above and below the conductor, and of coplanar line, which has the ground plane constructed horizontally in plane with the conductor. *Resonators* are simply lengths of transmission line separated from, but inductively coupled to, the external circuit, and are designed to form standing waves of multiples of one half the wavelength of the desired frequency with little power loss. They allow power of a particular frequency to be selectively stored in the circuit. The performance of a resonator is described by a quantity known as the Q-value. It is defined as

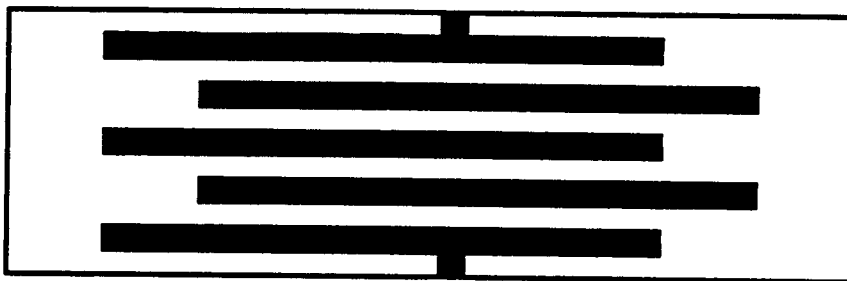
$$Q_o = 2\pi f_o W / P \quad (1.8)$$



(a)



(b)



(c)

Figure 1.3 (a) A schematic of a microstrip transmission line. The dark portion is the superconductor; the light portion is the dielectric. (b) An inductively coupled resonator. (c) A five-resonator-array bandpass filter.

where f_0 is the resonant frequency, W is energy stored in the resonator, expressed as the sum of the individual loss components

$$P = P_c + P_d + P_r \quad (1.9)$$

where P_c , P_d , and P_r are losses due to conductive, dielectric, and radiative effects. Conductive losses are a function of the surface resistance of the conductor, and are greatly minimized by the use of a superconductor. Radiative losses are primarily a function of the resonator design (43). Dielectric losses are a function of the loss tangent of the dielectric material used in the circuit, and are described by

$$P_d \propto \alpha_d = (\omega CZ_0 / 2) \cdot \tan \delta \quad (1.10)$$

where α_d is the attenuation of the signal due to the dielectric, ω is the resonant frequency, C is the capacitance of the circuit, and Z_0 is the impedance. *Filters*, in the simplest case, are merely cascaded resonators inductively coupled to one another, and are designed to drop or pass a particular resonant frequency. At each step, the undesired frequencies are rejected to a greater degree than the previous step, resulting in a sharp bandpass. The same general relationships that govern a single resonator apply to filters as well. From the relations above, it is obvious why a low dielectric constant and low loss substrate are desirable for these components. In the case of filters, a high dielectric constant will increase the dispersion of the signal (eqn. 1.7), decreasing the sharpness of the desired band. For resonators, a high loss tangent will lead to increased dielectric power loss, decreasing the Q value, and hence the efficiency, of the circuit. When signal speed is important for

transmission lines, a low dielectric constant will increase the signal velocity, and a low loss tangent will increase the efficiency of power transmission in the line.

With such a high dielectric constant, it is easy to see why strontium titanate ($\epsilon_r = 300$) is a poor substrate choice for microwave applications. Signal speed would be relatively slow, and frequency dispersion would be quite high in comparison to that in a circuit with a traditional dielectric ($\epsilon_r = \sim 3 - 6$), making it more difficult to obtain a sharp band through the use of filters. Lanthanum aluminate has a lower dielectric constant ($\epsilon_r = 23$) than any of the other commonly used materials except for MgO ($\epsilon_r = 10$), and has very similar lattice dimensions relative to YBCO and TBCCO. However, it possesses a phase transition between 450 and 500 °C. Below this temperature range, the structure is rhombohedral, and the dielectric characteristics are anisotropic. Above the transition temperature, the structure is cubic. Epitaxial film growth almost always occurs at a temperature greater than this. The films are therefore grown on a cubic substrate. After deposition, as the substrate is being cooled, it transforms from cubic to rhombohedral. The change in dimension is slight, and does not result in a catastrophic volume change comparable to that which occurs in lanthanum gallate, so films are not cracked. However, the phase transition results in the formation of twin planes along the pseudo cubic (110) and (101) substrate planes. Due to the anisotropic nature of the dielectric constant in this compound, the dielectric properties change as a signal crosses a twin boundary. Since the wavelength of a signal is a function of the dielectric constant of the substrate, the wavelength changes slightly upon crossing a twin plane. This changes the resonant

frequency of any resonators or filters that happen to cross the plane, making the design of a reliable precision circuit difficult or impossible.

Many researchers have been working around the existing substrate problems in their efforts to develop these devices. Other groups, however, have concentrated their efforts to solve the substrate problem itself. Three approaches have been taken: a) the attempted utilization of untried materials, b) the use of a passivating buffer layer between a common, but less desirable, substrate and superconducting film, and c) the modification or combination of currently used materials in order to modify the structure or other physical properties of the materials. The most commonly tried of the above solutions is the investigation of untried materials, whether newly synthesized or previously known. These materials are generally chosen for their structure and lattice match with the high T_c materials, and are usually perovskite or perovskite related. C. D. Brandle and V. J. Fratello studied a large number of double perovskites to test their suitability for these applications (25). The double perovskite structure is a particular case of the mixed perovskite. A mixed perovskite is generally obtained by substituting some ratio of two cations onto the B site such that the average oxidation state of the two is equal to that of the original B cation. It is given by the general formula $AB_{1-x}B'_xO_3$. In a double perovskite, the ratio of the B site cations is 1:1 (or, equivalently, $x = 0.5$), and the B cations order, doubling the size of the unit cell, and changing the space group from $Pm3m$ to $Fm3m$. The structure is shown in Figure 1.4. The most interesting compounds investigated in this study were those formed by combinations of the cations Al^{3+} and Ga^{3+} on the B' site and Nb^{5+} and Ta^{5+} on the B site. These materials were determined to be cubic, have

similar lattice dimensions to the superconductors, have low, isotropic dielectric constants and loss tangents, and be congruently melting, giving hope that single crystals of the compounds could be grown via the Czochralski method. The physical properties known thus far are summarized in table 1.3. However, single crystals of the compounds have proven to be quite difficult to grow, and none of substrate size have been reported.

The growth of buffer layers to passivate the surface of a less desirable substrate has been reported by several groups. CeO₂ thin films have been reported on LaAlO₃ (28). This compound has a cubic structure, and similar lattice dimensions in the <110> direction as the superconductors in their <100> and <010> directions. The critical temperature of YBCO films grown on this buffer layer were over 90 K. A less successful buffer layer is Mg₂TiO₄ (36). As mentioned above, Mg₂TiO₄ buffer layers have been synthesized on MgO by reaction with vapor phase TiO₂. The critical temperature of YBCO films grown on this surface were depressed to 85 K. The lattice constants of this material (4.22 Å) are slightly greater than those of MgO (4.21 Å), which is itself considered to have too much lattice mismatch. One of the double perovskites investigated by Brandle and Fratello (25), Sr₂AlTaO₆ (or SAT), has been the subject of several buffer layer investigations since it first appeared in the substrate literature. Findikoglu *et al* reported the synthesis of thin films of this material by laser ablation onto lanthanum aluminate substrates (26). They were able to measure the relative dielectric constant of the films and found them to be slightly higher

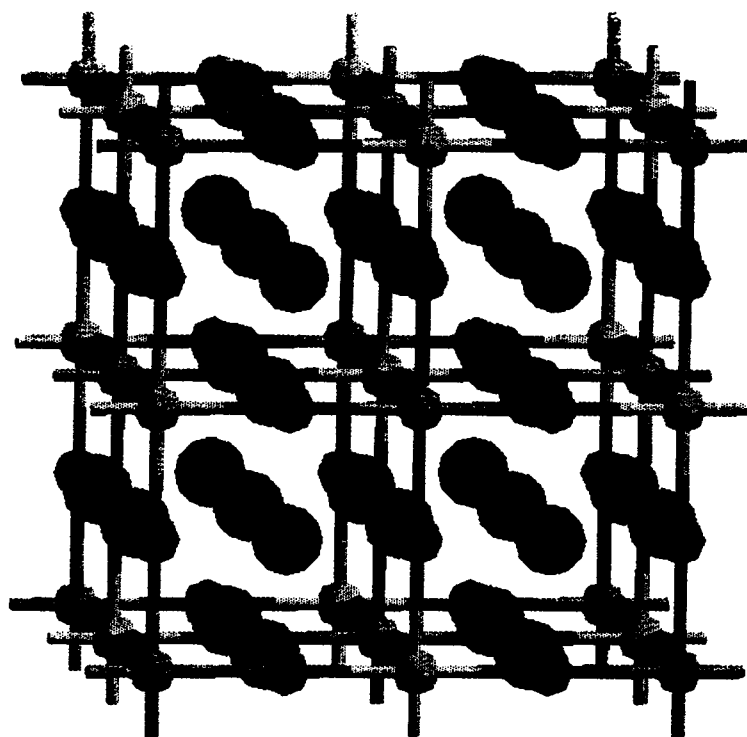


Figure 1.4 The double perovskite structure.

Table 1.3

Physical Properties of Double Perovskites

Compound	1/2 Lattice Constant (Å) ¹	$\Delta l / l$ (10 ⁻⁶ /°C)	Dielectric Constant	$\tan\delta$ (x10 ⁻³)	Melting Point (°C)
Sr ₂ AlNbO ₆	3.898 (1.1%)		9.5	0.59	1790
Sr ₂ GaNbO ₆	3.948 (2.4%)				1720
Sr ₂ AlTaO ₆	3.898 (1.1%)	9	10 (ceramic) ~23-30 (film)	4.24	1900
Sr ₂ GaTaO ₆	3.949 (2.4%)				1820
YBCO	a = 3.84 b = 3.88	11-12			

¹Number in parenthesis is the relative percent mismatch between the perovskite and average superconductor lattice constant.

($\epsilon_r = -23, 26,$ and 30) than measurements performed previously on ceramic samples ($\epsilon_r = 11.8$). YBCO films were not grown directly on the buffer layer, but SAT films were grown onto a LaAlO₃/YBCO multilayer structure to investigate its feasibility as an intermediate layer in devices. The critical temperature of the YBCO films in this arrangement were approximately 89 - 90 K. Han *et al* reported the synthesis of SAT films on LaAlO₃ substrates by metal organic chemical vapor deposition the following year (27). Standard x-ray diffraction analysis showed good c-axis orientation of the films, and x-ray phi scans demonstrated good in-plane epitaxy. No experiments with superconducting films were mentioned in this report.

Efforts to chemically modify substrate materials have centered primarily on lanthanum aluminate. The tolerance factor of this material is 1.016, which is in the range of cubic materials, yet it crystallizes in the rhombohedral space group $R\bar{3}c$. Upon heating, the structure changes to the ideal perovskite $Pm\bar{3}m$ structure. This phase transition was originally reported as occurring around 435 °C (44), but was later determined to be closer to 500 °C (45,46). The phase transition is second order, and is detected by a slight change in heat capacity, or by high temperature diffraction studies. Because the tolerance factor of the compound puts it seemingly close to a geometrically favorable cubic structure, research has focused on increasing the tolerance factor slightly through solid solution with other perovskites. The first report of such an experiment was an investigation by Bednorz and Muller of the LaAlO_3 - SrTiO_3 (tolerance factor=1.12) solid solution system (47). Strontium titanate has a phase transition from cubic to tetragonal at 105 K. The study attempted to follow the phase transition temperature, and the structural features of the system above and below this temperature, as a function of the composition of the system. They found a systematic decrease in the phase transition temperature with increasing incorporation of SrTiO_3 in the system, and a transition to the rhombohedral structure for concentrations of SrTiO_3 as high as 80%. They also found the system to be soluble across the whole composition range. However, too much disorder existed in the samples to accurately determine the transition temperature or the symmetry of the structure past the 80% SrTiO_3 concentration. Fergus and Alcock researched substituted lanthanum aluminate systems in conjunction with studies of solid electrolytes to determine which cations occupy the A or B site in the

structure (48). They reported a slight, smooth increase in the lattice constant a_0 with increasing Sr concentration, but treated the lattice angle as a constant in the study. Vanderah *et al* studied the effects on powder and single crystal x-ray patterns of the incorporation of SrTiO₃, Sr/Zr, Sr/Mg, and Sr/Sc/F into the lanthanum aluminate structure (49). Their results supported those of Fergus and Alcock in that substitution of strontium titanate resulted in an expanded unit cell. They also noticed that the structure became more cubic with increasing concentration of SrTiO₃. However, the work was qualitative, and no standard was used in the powder diffraction work, so no quantitative structural information was reported. Guo *et al* reported on the substitution of the mixed perovskites Sr₂AlTaO₆ and Sr₂AlNbO₆ into lanthanum aluminate and neodymium gallate (35). The resulting compounds were cubic, and displayed similar dielectric properties to the end members of the solid solution. Finally, Gloubokov *et al* reported the growth of (La, Sr, Ba)AlO_{3-y} crystals while attempting the growth of crystals in the (Sr, Ba)AlLaO₄ system. X-ray analysis led them to believe the crystals were cubic, and electron microprobe analysis showed the strontium content to be around 3%, and the barium around 0.10%. They concluded that the solubility of Sr in lanthanum aluminate was less than 3% from subsequent crystal growth experiments, and also determined that this doping level was sufficient to render the structure cubic.

The work presented in this thesis attempts to solve the substrate problem using each of the three methods listed above. One effort centers on the investigation of various materials as buffer layers to passivate the surface of MgO and to provide a good surface for the growth of the high

T_c films. Most of the materials investigated in this project belong to the double perovskite family. Attempts were also made to synthesize multilayer structures by growing films of Sr_2GaTaO_6 and Sr_2AlTaO_6 onto a YBCO film/ $LaAlO_3$ structure to test the effect of the deposition conditions of the double perovskite films on the superconducting properties of the YBCO film. Another approach to the problem has been the investigation of strontium substituted $LaAlO_3$. The report of a cubic structure with 3% strontium substitution in single crystals was the motivation for this work. Investigations into the nature of the defects induced in the structure by these substitutions have also been conducted. Finally, the synthesis of new perovskite oxyfluorides has been attempted in an effort to find new cubic materials with similar unit cell dimensions as the superconductors.

1.2 References

1. J. G. Bednorz and K. A. Muller, *Z. Physik* **B64**, 18 (1986).
2. M. K. Wu, J. R. Ashburn, C. J. Torng, P. H. Hor, R. L. Meng, L. Gao, Z. J. Huang, Y. Q. Wang, and C. W. Chu, *Phys. Rev. Lett.* **58**, 908 (1987).
3. H. Maeda, Y. Tanaka, M. Fukutomi, and T. Asano, *Jpn. J. Appl. Phys.* **27**, 1209 (1988).
4. Z. Z. Sheng and A. M. Herman, *Nature* **332**, 138 (1988).
5. C. C. Torardi, M. A. Subramanian, J. C. Calabrese, J. Gopalkrishnan, K. J. Morrissey, T. R. Askew, R. B. Flippen, U. Chowdhry, and A. W. Sleight, *Science* **240**, 631 (1988).
6. M. A. Subramanian, C. C. Torardi, J. Gopalkrishnan, P. L. Gai, J. C. Calabrese, T. R. Askew, R. B. Flippen, and A. W. Sleight, *Science* **242**, 249 (1988).
7. P. Chaudhari, R. H. Koch, R. B. Laibowitz, T. R. McGuire, and R. J. Gambino, *Phys. Rev. Lett.* **58**, 2684 (1987).
8. J. Geerk, G. Linker, and O. Meyer, *Materials Science Reports* **4**, 193 (1989).
9. A. W. Sleight, *Science* **242**, 1519 (1988).
10. C. B. Eom, J. Z. Sun, K. Yamamoto, A. F. Marshall, K. E. Luther, T. H. Geballe, and S. S. Laderman, *Appl. Phys. Lett.* **55**, 595 (1989).
11. R. S. Hiskes, S.A. DiCarolis, J. L. Young, S. S. Laderman, R. D. Jacowitz, and R. C. Taber, *Appl. Phys. Lett.* **59**, 606 (1991).
12. J. M. Phillips, M. P. Siegal, P. B. van Dover, T. H. Tiefel, J. H. Marshall, C. D. Brandle, G. Berkstresser, A. J. Strauss, R. E. Fahey, S. Sengupta, A. Cassanho, and H. P. Jenssen, *J. Mater. Res.* **7**, 2650 (1992).
13. J. Zhang, Z. Chen, D. Cui, H. Lu, Y. Zhou, L. Li, G. Yang, N. Jiang, and J. Hao, *Appl. Phys. Lett.* **66**, 2069 (1995).
14. K. H. Young, G. V. Negrete, M. M. Eddy, J. Z. Sun, T. W. James, McD. Robinson, and E. J. Smith, *Thin Solid Films* **206**, 116 (1991).

15. J. Kwo, M. Hong, D. J. Trevor, R. M. Fleming, A. E. White, R. C. Farrow, A. R. Kortan, and K. T. Short, *Appl. Phys. Lett.* **53**, 2683 (1988).
16. R. Guo, A. S. Bhalla, L. E. Cross, and R. Roy, *J. Mater. Res.* **9**, 1644 (1994).
17. H. Asano, S. Kubo, O. Michikami, M. Satoh, and T. Konaka, *Jpn. J. Appl. Phys.* **29**, L1452 (1990).
18. R. Ramesh, A. Inam, W. A. Bonner, P. England, B. J. Williams, B. J. Meagher, L. Nazar, X. D. Wu, M. S. Hedge, C. C. Chang, and T. Venkatesan, *Appl. Phys. Lett.* **55**, 1138 (1989).
19. W. L. Holstein, L. A. Parisi, R. B. Flippen, and D. G. Swartzfager, *J. Mater. Res.* **8**, 962 (1993).
20. M. Sasaura, M. Mukaida, and S. Miyazawa, *Appl. Phys. Lett.* **57**, 2728 (1990).
21. C. Tome-Rosa, G. Jakob, M. Maul, A Walkenhorst, M. Schmitt, P. Wagner, P. Przyslupski, and H. Adrian, *Physica C* **171**, 231 (1990).
22. D. Reagor and F. Garzon, *Appl. Phys. Lett.* **58**, 2741 (1991).
23. S. N. Mao, X. X. Xi, Q. Li, and T. Venkatesan, *J. Appl. Phys.* **75**, 2119 (1994).
24. R. Feenstra, L. A. Boatner, J. D. Budai, D. K. Christen, M. D. Galloway, and D. P. Poler, *Appl. Phys. Lett.* **54**, 1063 (1989).
25. C. D. Brandle and V. J. Fratello, *J. Mater. Res.* **5**, 2160 (1990).
26. A. T. Findikoglu, C. Doughty, S. Bhattacharya, Q. Li, X. X. Xi, T. Venkatesan, R. E. Fahey, A. J. Strauss, and J. M. Phillips, *Appl. Phys. Lett.* **61**, 1718 (1992).
27. B. Han, D. A. Neumayer, B. H. Goodreau, T. J. Marks, H. Zhang, and V. P. Dravid, *Chem. Mater.* **6**, 18 (1994).
28. X. D. Wu, R. C. Dye, R. E. Muenchausen, S. R. Foltyn, M. Maley, A. D. Rollett, A. R. Garcia, and N. S. Nogar, *Appl. Phys. Lett.* **58**, 2165 (1991).
29. K. H. Young and J. Z. Sun, *J. Appl. Phys.* **70**, 3748 (1991).
30. Z. Barkay, D. Racah, E. Grunbaum, and G. Deutscher, *J. Appl. Phys.* **73**, 7585 (1993).

31. D. K. Fork, F. A. Ponce, J. C. Tramontana, N. Newman, J. M. Phillips, and T. H. Jeballe, *Appl. Phys. Lett.* **58**, 2432 (1991).
32. J. Konopka, I. Wolff, and S. J. Lewandowski, *J. Appl. Phys.* **72**, 218 (1992).
33. R. Brown, V. Pendrick, D. Kalokitis, and B. H. T. Chai, *Appl. Phys. Lett.* **57**, 1351 (1991).
34. S. Hontsu, J. Ishii, T. Kawai, and S. Kawai, *Appl. Phys. Lett.* **59**, 2886 (1991).
35. R. Guo, P. Ravindranathan, U. Selvaraj, A. S. Bhalla, L. E. Cross, and R. Roy, *J. Mater. Sci* **29**, 5054 (1994).
36. H. Haefke, H. P. Lang, R. Sum, H. J. Guntherodt, L. Berthold, and D. Hesse, *Appl. Phys. Lett.* **61**, 2359 (1992).
37. T. N. Blanton, M. Lelenthal, and C. L. Barnes, *Physica C* **184**, 119 (1991).
38. Anthony R. West, *Solid State Chemistry and its Applications*, pp. 534-537, John Wiley and Sons, New York (1985).
39. V. J. Fratello and C. D. Brandle, *J. Mater. Res.* **9**, 2554 (1994).
40. R. D. Shannon, *J. Appl. Phys.* **73**, 348 (1993).
41. Thomas S. Laverghetta, *Microwave Materials and Fabrication Techniques*, pp. 11-13, Artech House, Inc., Dedham, MA (1984).
42. Shen, Zhi-Yuan, *High-Temperature Superconducting Microwave Circuits*, p xi, Artech House, Boston (1994).
43. Shen, pp. 103-107.
44. S. Geller and V. B. Bala, *Acta Cryst.* **9**, 1019 (1956).
45. J. Coutures and J. P. Coutures, *J. Sol. St. Chem.* **52**, 95 (1984).
46. H. M. O'Bryan, P. K. Gallagher, G. W. Berkstresser, and C. D. Brandle, *J. Mater. Res.* **5**, 183 (1989).
47. J. G. Bednorz and K. A. Muller, *Mat. Res. Bull.* **18**, 181 (1983).
48. J. Fergus and C. B. Alcock, *Mater. Lett.* **12**, 219 (1991).

49. T. A. Vanderah, C. K. Lowe-Ma, and D. R. Gagnon, *J. Am. Ceram. Soc.* **77**, 3125 (1994).
50. A. Gloubokov, A. Klos, J. Fink-Finowiki, and A. Pajaczkowska, *Mater. Res. Bull.* **31**, 271 (1996).

Chapter 2

A₂BB' O₆ Double Perovskite Thin Films as Buffer Layers for High Temperature Superconducting Thin Films

2.1 Introduction

Materials of the general type A₂BB' O₆ were first investigated as potential substrate materials for high temperature superconducting thin films by Brandle and Fratello (1). The motivation for this research was the lack of good substrate materials for use in microwave applications at the time. The materials most commonly used then were simple perovskites such as SrTiO₃, LaAlO₃, and NdGaO₃, as well as the binary oxides MgO and ZrO₂. LaAlO₃ and LaGaO₃ possess phase transitions between device operating temperature and growth temperature that result in twin plane formation. The simple oxides have larger lattice mismatch, and a polished MgO surface is unstable to exposure to air. SrTiO₃ has a prohibitively large dielectric constant, and single crystals can be grown only via the Verneuil technique, limiting the size of available crystals. The researchers were in search of compounds that had the properties desirable in a good substrate material, and that could be grown as large single crystals using the Czochralski technique. The study identified the materials Sr₂AlNbO₆, Sr₂AlTaO₆, Sr₂GaNbO₆, and Sr₂GaTaO₆ as potentially very good substrate materials, based on their cubic symmetry and unit cell dimensions. However, a material must meet criteria additional to those that define a good substrate if the Czochralski technique is to be used to grow single crystals. These include (a) a congruent melting composition at or near the stoichiometric composition, (b) a lower melting point than the crucible material, usually

Pt or Ir, and (c) a good resistance to reduction, among others. Although congruently melting, the $\text{Sr}_2\text{BB}'\text{O}_6$ perovskites proved to be difficult to grow as single crystals using this technique, as the melting points were too high to be used with platinum crucibles, and the Ta and Nb were found to be reduced in the crystals grown other ways in air (2).

To get around the crystal growth problem, the $\text{Sr}_2\text{BB}'\text{O}_6$ materials were investigated as buffer layer materials. Other potentially good substrates had been investigated as buffer layers previously, such as CeO_2 (3) and PrGaO_3 (4), that resulted in good performance of superconducting films deposited on top of them. Other materials such as NdGaO_3 (5) have been investigated as thin film buffers, but were not studied as a heterostructure with a superconductor. $\text{Sr}_2\text{AlTaO}_6$ was first reported as a thin film on LaAlO_3 by Findikoglu *et al* (6). The film was deposited by laser ablation, which is the transfer of energy to a target of the desired composition by exposure to high energy laser pulses, resulting in the removal of target material and its subsequent deposition onto the substrate surface. Standard x-ray analysis showed the films to be c-axis oriented, and rocking curve analysis showed little off-orientation growth. The dielectric constant was somewhat higher ($\epsilon_r=23, 26, \text{ and } 30$) compared to a ceramic sample ($\epsilon_r=11.8$). Han *et al* reported the successful growth of an $\text{Sr}_2\text{AlTaO}_6$ film on LaAlO_3 through metalorganic chemical vapor deposition (7). X-ray analysis showed the films to be c-axis oriented, and x-ray phi scans verified the crystallinity in the a-b plane. No other studies of thin films of compounds of this structural type have yet been reported in the literature.

In this study, depositions of thin films of various compounds of the general type $\text{A}_2\text{BB}'\text{O}_6$ were attempted by RF magnetron sputtering in

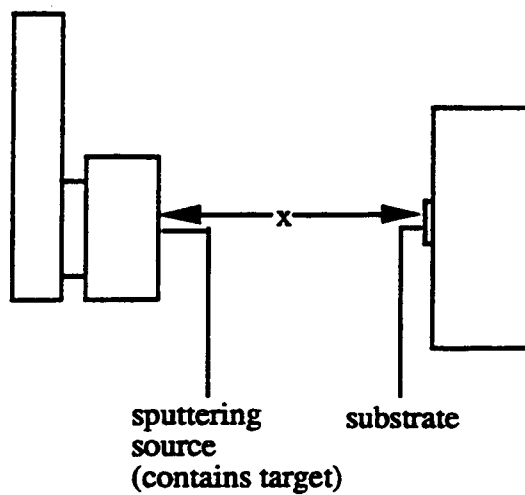
order to determine which are suitable to be grown by this technique, as well as which are suitable for use as buffer layers with high temperature superconducting thin films. The films were grown on (100) MgO to test as a buffer layer, and on a (001) YBCO film/LaAlO₃ substrate heterostructure to study the effect of film growth on the superconducting properties of YBCO.

2.2 Experimental

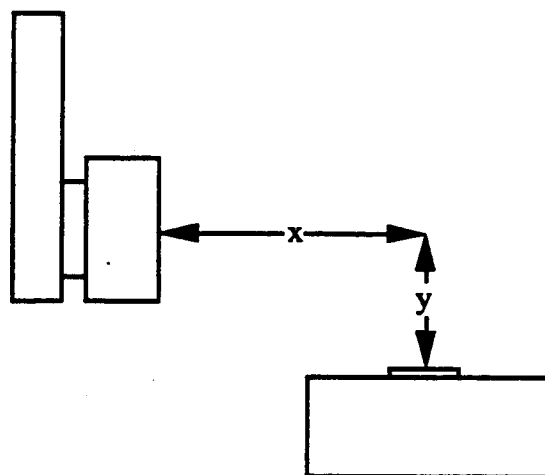
2.2.1 RF Magnetron Sputtering

As previously mentioned, radio frequency magnetron sputtering was used to prepare the films. Film growth by sputtering relies on the use of high energy argon ions to impact and remove material from a target of the desired film composition. The ions are generated in a glow discharge. This is a plasma, or a gas consisting of ions and electrons, with an electron density in the range of approximately 10^9 to 10^{12} cm⁻³ and a characteristic electron energy of approximately 1 to 10 eV. Argon, or other gases, are introduced into a vacuum chamber at a pressure of around 10 to 100 millitorr. A large electric field is generated between the target, which serves as the cathode, and an anode ring. The electric field accelerates electrons, which collide with argon atoms, resulting in ionization and the generation of more electrons. The electric field also accelerates the argon atoms toward the cathode. The ions strike the surface of the target. These collisions can result in ion implantation, backscattering of the ions, or the transfer of energy to target atoms, resulting in their removal. If an insulator is to be sputtered, the continued bombardment with positive ions can result in a positive potential on the target surface, which will repel other positive ions, and

result in a sharp decrease in sputtering rate. The use of an alternating electric field, centered about an applied bias of 0 volts, causes the impingement of electrons onto the target surface every half cycle, resulting in the neutralization of excess surface charge, allowing the sputtering of insulating materials. Empirical observations have shown radio frequencies to be the best for sputtering, and frequencies of 13.56 MHz, and multiples thereof, are used most often, as they are consistent with the regulations of the Federal Communications Commission and its international equivalents. Magnetron sputtering involves the use of a magnetic field to cause electrons in the plasma to travel in a ellipsoidal path close to the target surface, thereby reducing recombination effects and electron loss, and increasing both electron and ion density in the plasma. This results in higher sputtering rates (8). Sputtering can be carried out in two basic different geometrical arrangements: on-axis and off-axis. These terms refer to the orientation of the substrate surface relative to the target normal. Off-axis sputtering is performed with the substrate surface parallel to the target normal, and on-axis is done with the substrate surface perpendicular to the target normal. Simple schematics of these arrangements are given in Figure 2.1. A depiction of the geometrical variables in each arrangement is also given in the figure. A US II 1 inch magnetron sputtering source was used in these experiments.



(a)



(b)

Figure 2.1 Schematics of (a) on-axis, and (b) off axis sputtering geometries. Geometrical variables x and y relate the target and substrate positions.

2.2.2 Target Preparation

One inch diameter ceramic pellets of the desired film composition were prepared as sputtering targets. The compositions tested were Ca_2MgWO_6 , Sr_2MgWO_6 , $\text{Sr}_2\text{AlNbO}_6$, $\text{Sr}_2\text{GaNbO}_6$, $\text{Sr}_2\text{AlTaO}_6$, and $\text{Sr}_2\text{GaTaO}_6$. The Ca_2MgWO_6 was prepared by grinding together stoichiometric proportions of WO_3 , $\text{Mg}(\text{NO}_3)_2 \cdot 6\text{H}_2\text{O}$, and CaCO_3 with an agate mortar and pestle. The mixture was subjected to subsequent heatings of 900, 1300, and 1400 °C for 10 hours each (heating rate=500 °C/hr), grinding thoroughly between each heating cycle. The material was then mixed with a polyvinyl alcohol binder, pressed into a 1 inch diameter by 1/8 inch thick pellet and sintered at 1400 °C for 10 hours. The target shrunk greatly during this step, and was reground. The powder was verified to be single phase by x-ray diffraction. The compound was then heated to 1600 °C for 10 hours, reground, pressed into a 1 inch diameter pellet again, and heated to 1400 °C for 1 hour. The target sintered well and shrunk very little.

The Sr_2MgWO_6 was prepared by grinding together stoichiometric amounts of SrCO_3 , $\text{Mg}(\text{NO}_3)_2 \cdot 6\text{H}_2\text{O}$, and WO_3 . The mixture was first heated to 900 °C for 10 hours, then to 1400 °C twice for the same amount of time. The material was then mixed with a small amount of PVA binder, pressed into a 1 inch pellet, and sintered for one hour at 1400 °C. Diffraction studies on the pellet verified it to be single phase.

The compounds $\text{Sr}_2\text{AlNbO}_6$, $\text{Sr}_2\text{GaNbO}_6$, $\text{Sr}_2\text{AlTaO}_6$, and $\text{Sr}_2\text{GaTaO}_6$ were prepared via a flux/anneal synthesis as described in reference 9. For the $\text{Sr}_2\text{AlNbO}_6$ target, $\text{Sr}(\text{NO}_3)_2$, Al_2O_3 , and Nb_2O_5 were ground together and heated to 900 °C for 1 hour to decompose the nitrates. An equal mass of SrCl_2 was then mixed into the reactants as a

flux, and the mixture was heated to 900 °C for 8 hours. The flux was then washed away with a dilute HCl solution, and the recovered product dried, pressed into a 1 inch pellet, and annealed at 1500 °C for 12 hours. The pellet shrunk slightly during the anneal, so it was necessary to regrind and reanneal it. Similar procedures were adopted for the synthesis of the $\text{Sr}_2\text{AlTaO}_6$ and corresponding gallate targets. The approximate mass of all pellets was 6g.

2.2.3 Dielectric Thin Film Preparation and Film Analysis

A US II one inch sputtering gun from US Inc. was used in all depositions. Film depositions were done with various ratios of argon and oxygen, always with a total pressure of 50 millitorr in the vacuum chamber. The background pressure was 10^{-3} millitorr. The substrate temperature was between 600 °C and 700 °C for most depositions. Higher and lower temperatures were investigated, but did not consistently result in the growth of good epitaxial films. Both off-axis and on-axis sputtering geometries were attempted. The off-axis dimensions (referring to those shown in Figure 2.1) used in the depositions were $x=2.5$ " and $y=1.5$ ". The distance between the target and substrate for the on-axis configuration was $x=2.5$ ". RF power was around 50 watts. The films were deposited onto (100) MgO, polished on one side, obtained from Electronic Space Products International. The dimensions of the substrates as ordered were .5 inch x .5 inch x .02 inch, but were cleaved into pieces roughly one quarter this size for the film growth. Films were cleaved by holding a razor vertically against the edge of the substrate, and tapping the razor firmly with a pair of tweezers. Substrates were kept in a sealed package with a desiccant prior to cleaving. After

cleaving, the pieces not immediately used were stored in methanol. Those that were to be used for a deposition were washed first with acetone, then with methanol, and exposed to air minimally prior to mounting on the heating block. The heater consisted of 2 500 W, 120 V Sylvania tungsten-halogen lamps mounted in an Inconel casing, which could be oriented parallel or perpendicular to the target face. The substrates were attached to the heater by silver paint, and the temperature was detected by an R-type thermocouple attached to the heater with silver paint directly against the side of the substrate. Deposition time was between 4 and 6 hours.

The crystallinity of the films was characterized by x-ray diffraction. Standard two-theta scans and rocking curves were performed with a Siemens D-5000 diffractometer. Two-theta scans were obtained over a range of 2° - 115° . Rocking curves were performed on the (002) film peak to study the degree of the c-axis alignment of the film. In this analysis, the two-theta angle of the diffractometer is set at the correct angle to detect the reflection from a chosen set of planes, which are usually parallel to the film surface. Then, the angle ω , or the angle of the plane of the film surface relative to the incident x-ray beam, is varied to detect any off orientation grains in the film. X-ray phi scans were done to determine the crystallinity of the film in the a-b plane. In a phi scan, both 2θ and ω are fixed to focus a set of planes other than the [00l]. Then, the film is rotated around the angle ϕ , which is equivalent to rotation about the film surface normal. The rotation brings each equivalent (hk0) peak sequentially into the Bragg condition, giving multiple peaks spaced at regular intervals of ϕ . For films in this report that were of good enough quality to warrant this study, the (220) peaks

were chosen for examination. Film morphology was characterized by scanning electron microscopy (SEM) and atomic force microscopy (AFM). Film thickness was measured mechanically with a stylus roughness detector (Alpha-step 100, Tencor Instruments). Electron microprobe analysis (EMPA) was used to investigate the compositions of the films.

Early research on this project revealed that the niobates are more difficult to sputter than the tantalates. The difficulty with sputtering insulators is the tendency for the metal surfaces in the vacuum chamber to become coated with the dielectric. Once the metals are coated with an insulating film, electrons in the chamber that contact the surfaces have no path to ground. Charge builds up on the surfaces, resulting in periodic arcs between metal surfaces of different potential in the vacuum chamber. Regular and frequent sandblasting of the metal components is necessary to keep the system running. It was possible to sputter 6-7 tantalate films between cleanings, while it was difficult to sputter a single niobate film without encountering arcing problems.

2.2.4 Multilayer Film Preparation

Thin films of (001) YBCO on (110) LaAlO₃, deposited by laser ablation, were obtained from Conductus, Inc., for use as substrates for dielectric thin film growth. The substrates were attached to the heater surface with silver paint. The samples were heated in both vacuum and 200 millitorr O₂. The dielectric target compounds used in these experiments were Sr₂GaTaO₆ and Sr₂AlTaO₆. The gas composition used in all depositions was a 45.5 millitorr Ar/4.5 millitorr O₂ mixture, for a total pressure of 50 millitorr. The substrates were heated to 675 or 700 °C, and depositions were carried out for a time of approximately 4 to 5

hours. Both off-axis and on-axis geometries were attempted, with the off-axis runs lasting 5 hours, and the on-axis from 4 to 5 hours. After dielectric film deposition, samples were annealed at 400 °C for 6 hours, then cooled, in 50-200 torr O₂. They were characterized by two-theta x-ray diffraction analysis before being sent to Conductus for further analysis, such as critical temperature determination and etch resistance.

2.3 Results

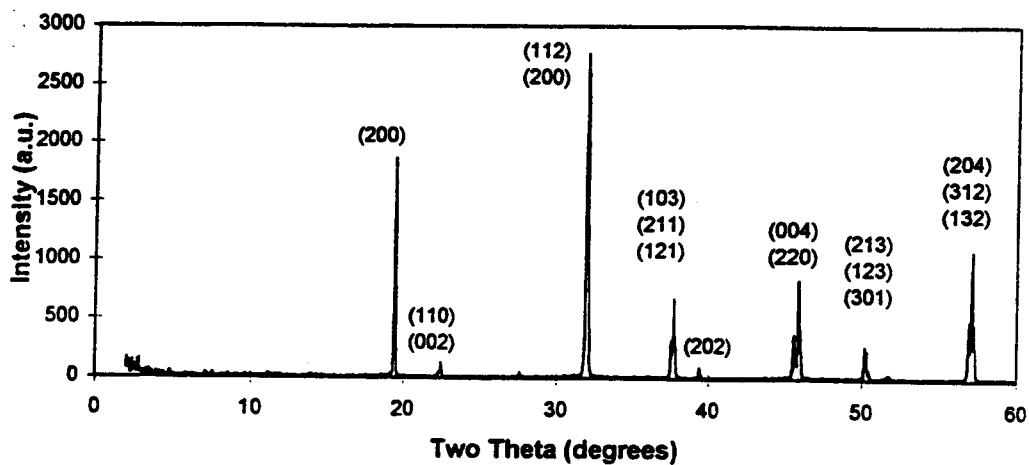
2.3.1 A₂MgWO₆ Films

Three depositions of films from the Sr₂MgWO₆ target were attempted. The deposition conditions for each run are given in Table 2.1, along with those for the Ca₂MgWO₆. Sr₂MgWO₆ is a tetragonally distorted, ordered double perovskite, and crystallizes in the space group I4/m. The lattice parameters of the true unit cell are a=5.579 Å and c=7.938 Å. The pseudo cubic cell dimension along the (110) distance in the true cell is 3.945 Å, and 3.969 Å along the (001). This is fairly close to the (100) and (010) distances in YBCO (see Table 1.1), and much closer than commonly used substrates such as MgO. An indexed x-ray diffraction pattern of the target is given in Figure 2.2 (a). A temperature of 700° C was chosen for initial attempts at film growth (SMW 1). An x-ray diffraction pattern of a resulting film is given in Figure 2.2 (b). Looking at the film pattern, it is evident that no peaks in the target pattern match those in the film pattern. A powder diffraction file database search identified the film phases as polycrystalline SrWO₄ and MgWO₄. Substrate temperatures of 750 and 800 °C were also tried. The only crystalline phase grown was MgWO₄.

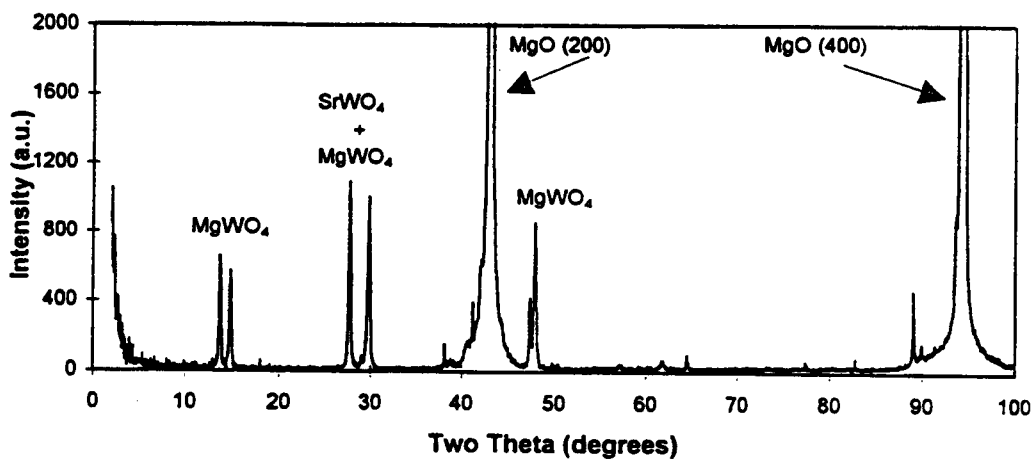
Table 2.1Deposition Conditions for Sr₂MgWO₆ and Ca₂MgWO₆ Thin Films

Compound/ Geometry	P(Ar) (millitorr)	P(O ₂) (millitorr)	T _{substrate} (°C)	Observations
SMW/on-axis	41.7	8.3	700	MgWO ₄ / SrWO ₄ film.
SMW/on-axis	41.7	8.3	750	MgWO ₄ film.
SMW/on-axis	41.7	8.3	800	MgWO ₄ film.
CMW/off-axis	41.7	8.3	650	No crystalline film.
CMW/on-axis	41.7	8.3	650	No crystalline film.
CMW/on-axis	41.7	8.3	700	Unidentified crystalline film+smaller second phase.

Three attempts were also made at synthesizing Ca₂MgWO₆ thin films. The films were sputtered from a target that was verified to be single phase by x-ray diffraction. The bulk material crystallizes in the monoclinic space group $P2_1/c$, with lattice constants of $a=5.421$, $b=5.55$, $c=7.716$, and $\beta=89.90$. The pseudocubic unit cell vector along the true unit cell $\langle 110 \rangle$ direction (the average of the true cell $d(110)$ and $d(\bar{1}10)$) is 3.878 \AA , and along the (001) is 3.858 \AA . These values are again very close to those of the superconducting oxides. A partially indexed x-ray diffraction pattern for the target is given in Figure 2.3 (a). Due to the large number of reflections from this low symmetry structure,

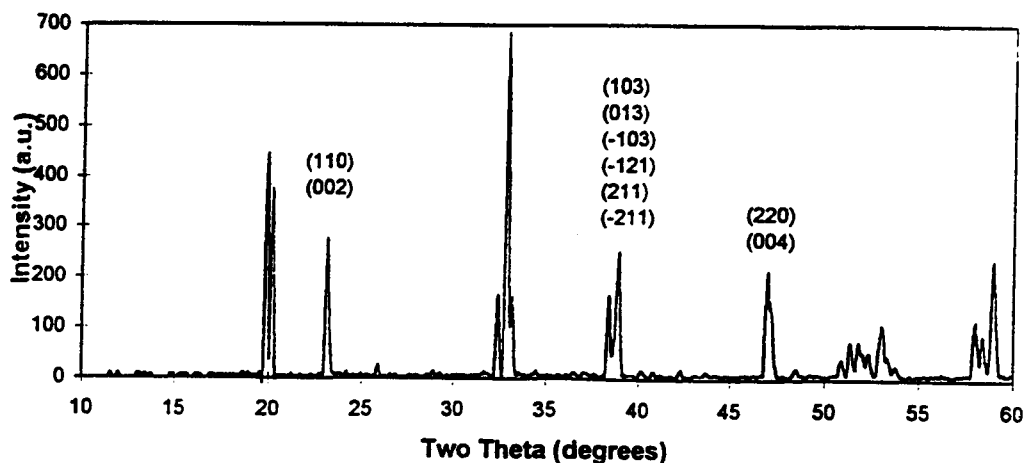


(a)

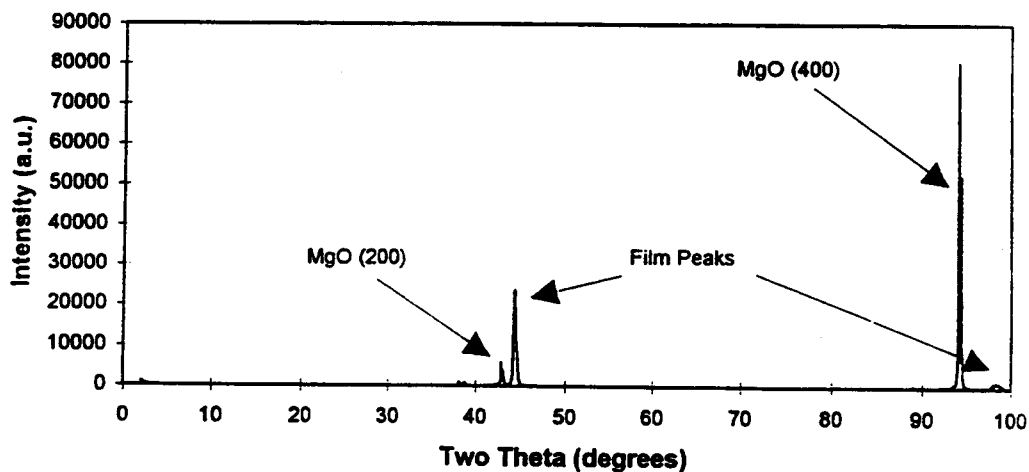


(b)

Figure 2.2 X-ray diffraction patterns from (a) a ceramic Sr_2MgWO_6 target and (b) the thin film sample SMW 1 on (100) MgO . All peaks in the film pattern can be indexed to the phases SrWO_4 and MgWO_4 , and none match the bulk phase.



(a)



(b)

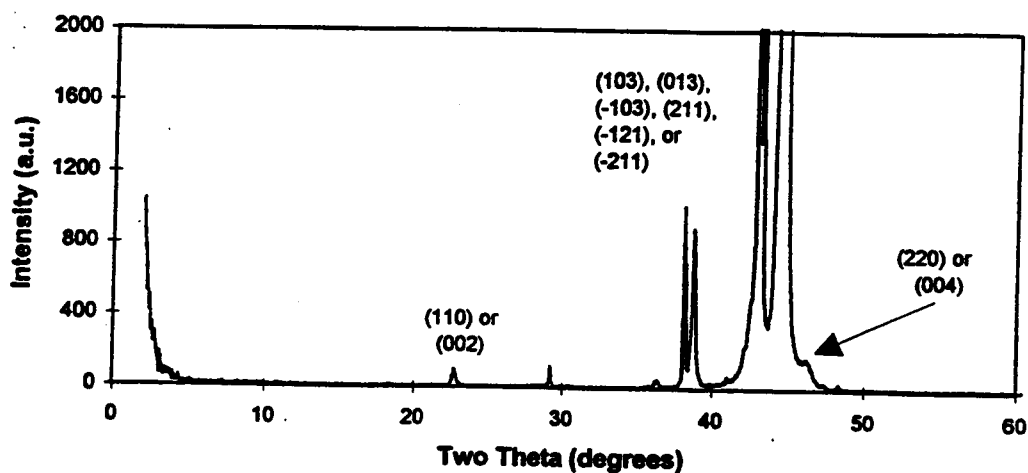
Figure 2.3 X-ray diffraction patterns from (a) a ceramic Ca_2MgWO_6 target and (b) the thin film sample on (100) MgO. The scale of the film pattern is large to show the intensity of the film peaks relative to the substrate peaks. The large film peaks do not match any peaks in the bulk phase powder pattern.

not all peak indices are given, but those clusters belonging to sets of planes that are of concern to the use of the compound as a substrate are fully indexed. Two attempts to grow films of this compound were done with a substrate temperature of 650 °C, and both on-axis and off-axis geometries. They resulted in no crystalline film growth, although there was evidence of the deposition of an amorphous phase.

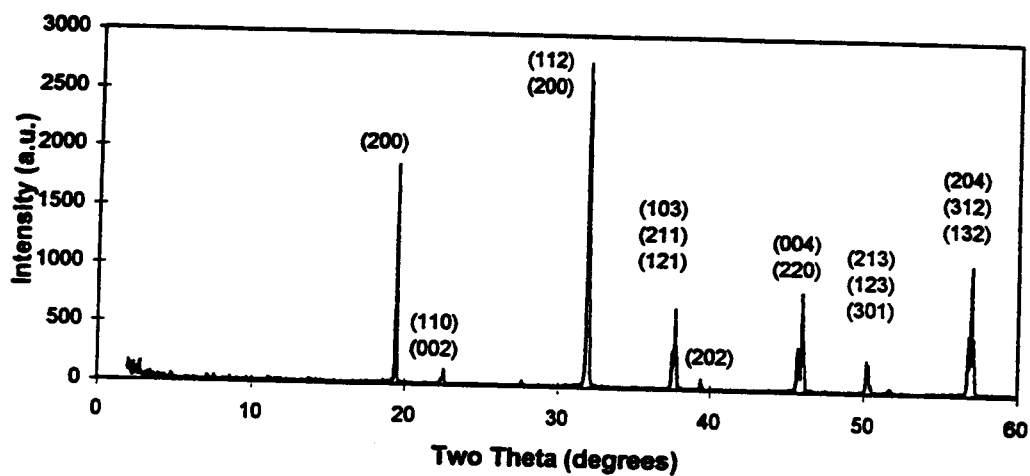
A third attempt at Ca_2MgWO_6 film deposition was done on axis with a substrate temperature of 700 °C. A majority phase was clearly visible, shown in comparison with the bulk pattern in Figure 2.3 (b). Although intense, the film peaks do not correspond to any in the bulk pattern. They also did not compare to any Ca/Mg/W phases in the JCPDS Powder Diffraction File. Figure 2.4 shows very low intensity film peaks from a second phase. These do match the position of some of the Ca_2MgWO_6 bulk peaks. However, due to the high degree of peak overlap resulting from the low symmetry of the bulk compound, it is impossible to determine if the correct phase is growing. Due to the low symmetry of the bulk compound, it is likely that films would contain many individual crystallites, and grow in numerous orientations. This would make the design of reliable devices on films of this compound quite difficult. For these reasons, this project was not pursued further.

2.3.2 Sr_2BNbO_6 (B=Al, Ga) Thin Films

Attempts were made to deposit thin films of the cubic materials Sr_2BNbO_6 (B=Al, Ga). Both materials are ordered perovskites, and crystallize in the space group $Fm\bar{3}m$. The unit cell constant of the aluminate is $a = 7.794 \text{ \AA}$ (or $a/2 = 3.897 \text{ \AA}$), and of the gallate is $a=7.894 \text{ \AA}$ (or $a/2=3.947 \text{ \AA}$). Table 2.2 summarizes the work done in this system.



(a)



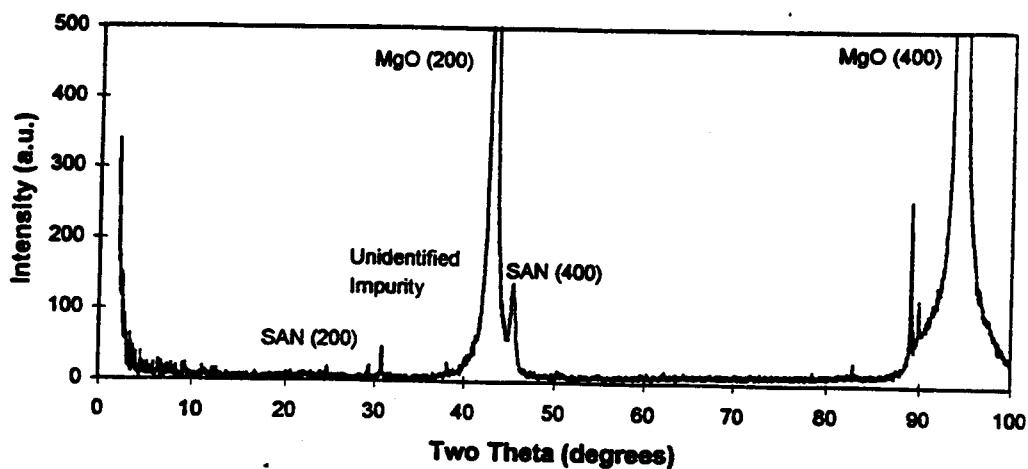
(b)

Figure 2.4 Small second phase peaks of (a) a CMW film x-ray pattern in comparison with (b) the target material.

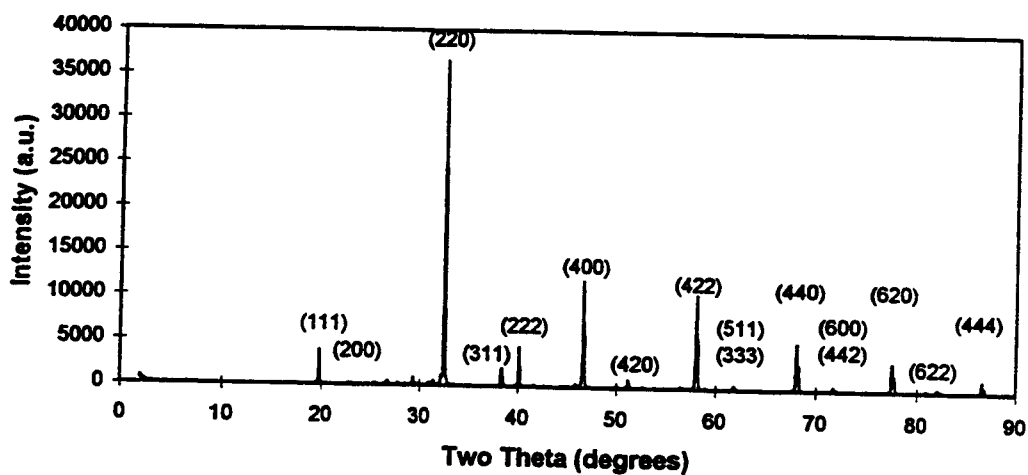
Table 2.2Deposition Conditions for Sr₂AlNbO₆ and Sr₂GaNbO₆ Thin Films

Compound/ Geometry	P(Ar) (millitorr)	P (O ₂) (millitorr)	T _{substrate}	Observations
SAN/off-axis	41.7	8.3	650	No crystalline film.
SAN/on-axis	41.7	8.3	700	Apparent SAN phase.
SGN/on-axis	41.7	8.3	700	Apparent SGN phase. (110) orientation.
SGN/on-axis	41.7	8.3	725	Apparent SGN phase. (110) and (100) orientations.
SGN/on-axis	41.7	8.3	750	Apparent SGN phase. (100) orientation.

Film growth was attempted in both off-axis and on-axis orientations. Off-axis sputtering did not result in crystalline film growth. On-axis sputtering was successful in growing a film. X-ray diffraction patterns of this film and the source target are given in Figure 2.5. Note the presence of x-ray diffraction peaks in the film sample that match those in the bulk Sr₂AlNbO₆ pattern. Also note the relative intensities of the (200) and (400) peaks of the phase in the film and bulk SAN patterns. In both cases, the intensity of the (200) is much lower than the (400); it is almost not visible in the patterns. This is strong evidence that the film structure is similar to the bulk structure. Film peaks are shifted to higher d-

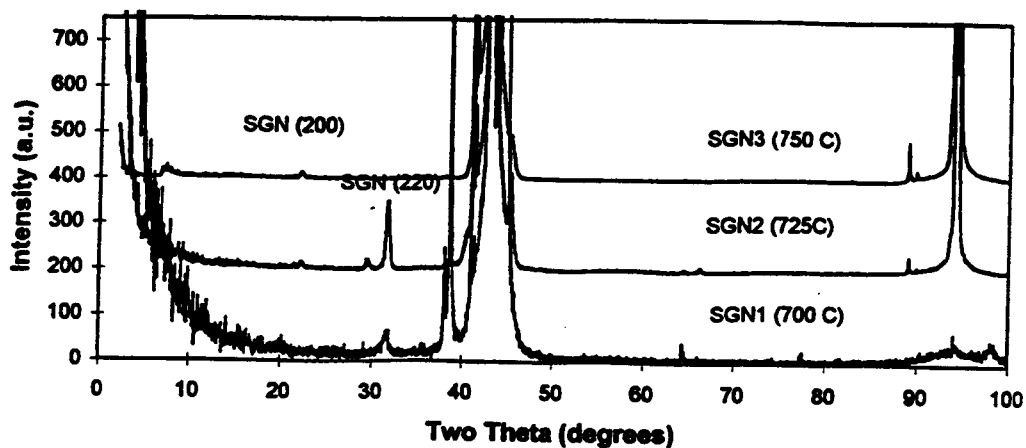


(a)

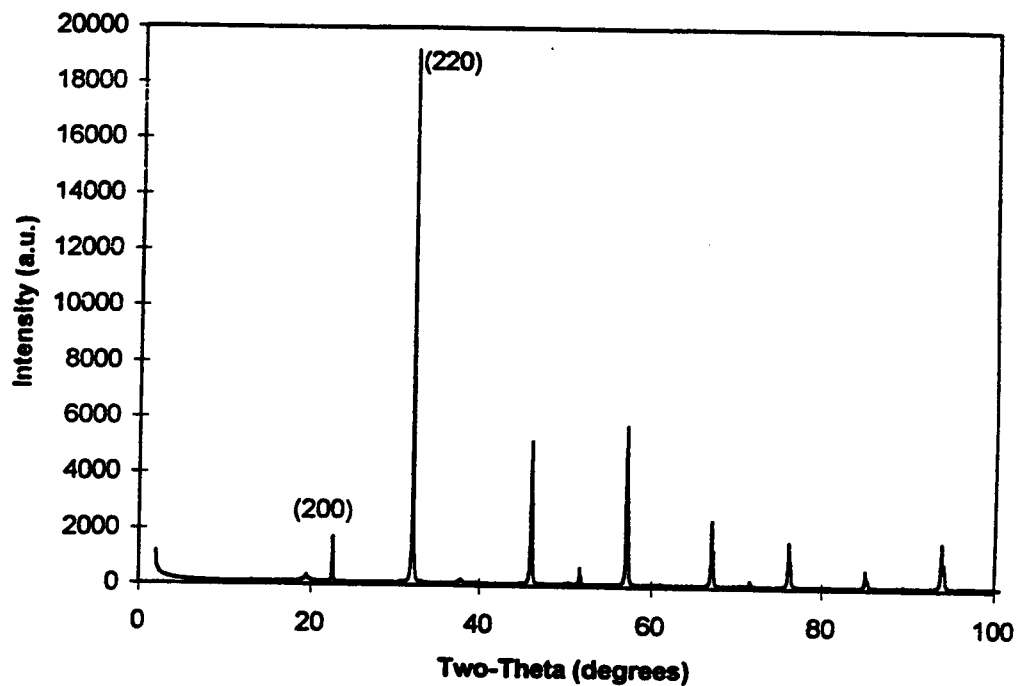


(b)

Figure 2.5 X-ray diffraction patterns of (a) a SAN thin film in comparison to (b) the bulk phase. Notice the similar peak intensities for the two phases, suggesting that the correct phase was grown.



(a)



(b)

Figure 2.6 X-ray diffraction patterns of (a) SGN thin films showing the variation of the film orientation with deposition temperature. Pattern (b) is from the bulk phase.

spacings than bulk peaks, indicating an expanded lattice. This effect is also seen in films of other compounds, described below.

The syntheses of films of $\text{Sr}_2\text{GaNbO}_6$ were attempted with an on-axis geometry at substrate temperatures of 700, 725, and 750 °C (SGN 1, 2, and 3, respectively). All three films showed evidence of a film, with peaks that are of comparable d-spacings to the bulk $\text{Sr}_2\text{GaNbO}_6$ pattern. Comparing the SGN film peaks to the bulk pattern, it appears that increasing substrate temperature results in a change in film orientation from (110) to (100). The three scans are shown in comparison to the target x-ray pattern in Figure 2.6.

These preliminary results suggest that films of SAN and SGN can be grown by on-axis RF magnetron sputtering, and in the desired orientation when a high enough substrate temperature is used. The good lattice match to YBCO, cubic symmetry, and attractive dielectric properties of the bulk compounds make further research into these materials an interesting proposition.

2.3.3 $\text{Sr}_2\text{GaTaO}_6$ Thin Films

2.3.3.1 Optimization of Substrate Temperature

$\text{Sr}_2\text{GaTaO}_6$ is a cubic double perovskite. The B and B' cations (Ga and Ta, respectively) order in the structure, and the compound crystallizes in the space group $Fm\bar{3}m$. The lattice constant of the material is $a = 7.898 \text{ \AA}$ (or $a/2 = 3.949 \text{ \AA}$). Initial results from attempts at sputtering films from a $\text{Sr}_2\text{GaTaO}_6$ target indicated that the films grew best with the use of an on-axis sputtering geometry.

Optimization of the substrate temperature for SGT film growth was performed in an on-axis geometry with a total pressure of 50 millitorr,

Table 2.3**X-Ray Diffraction and Composition Data for SGT Film Temperature Optimization Depositions**

T_s (°C)	d (200) (Å)	FWHM (200) Two-Theta Scan (degrees)	FWHM (200) Rocking Curve (degrees)	EMPA
600	3.99	.565	3.091	---
650	3.99	.456	2.973	Sr _{.53} Al _{.44} Ga _{.41} Ta ₁
675	3.99	.397	2.821	Sr _{.53} Al _{.61} Ga _{.38} Ta ₁
700	---	---	---	---

consisting of 8.3 mT oxygen and 41.7 mT argon. Films were deposited at substrate temperatures of 600, 650, 675, and 700 °C. Films were successfully synthesized at all temperatures but 700 °C. Table 2.3 summarizes x-ray and composition data from these films. Using the MgO peaks as an internal standard, the distance between (200) planes was determined for each film. In each case, the distance was 3.99 Å, compared to the bulk value of 3.94 Å for Sr₂GaTaO₆. The full width at half maximum (FWHM) of the 200 peaks was calculated using peak fitting software for a rough comparison of particle size and strain in the films. With increasing film growth temperature, the FWHM of the (200) peak decreases slightly, suggesting that higher substrate temperature can result in improved crystallinity. Rocking curve scans were performed on the (200) peaks of these films. The degree of off-orientation growth decreases with increasing substrate temperature, evident by the sharpening rocking curve profiles with increasing temperature. EMPA data suggests that the films are very strontium deficient. This was also evident in the Sr₂MgWO₆ depositions, as the primary phase deposited

was MgWO_4 , with a lesser amount of SrWO_4 . The presence of both cation vacancies and, therefore, charge balancing defects, is presumably the reason for the observed discrepancy between bulk and film cell parameters. Additionally, a high concentration of aluminum was found in the films. The $\text{Sr}_2\text{GaTaO}_6$ target was determined to be of the correct stoichiometry by EMPA. The source of the aluminum is likely resputtering effects from the anode cap, as it was machined from an aluminum alloy, and appeared etched after a few months of use. The data from these films suggests that substrate temperatures in the range of 650 to 675 °C result in the best SGT film growth.

2.3.3.2 Optimization of Gas Composition

X-ray diffraction results from the temperature optimization suggested that either 650 or 675 °C were good temperatures for the growth of these films. The next series of depositions investigated the effect of changing gas composition on film growth at these temperatures. Conditions used in the growth of these films are given in Table 2.4. Four different gas compositions were tested: 41.7 mT argon/8.3 mT oxygen (or 5:1 Ar:O₂), 45 mT argon/5 mT oxygen (9:1), 47.5 mT argon/2.5 mT oxygen (19:1), and 49 mT argon/1 mT oxygen (49:1). The films were characterized by two-theta and rocking curve x-ray analysis, and by EMPA. Results are summarized in Table 2.4.

Gas mixtures of 5:1, 9:1 and 19:1 Ar:O₂ all resulted in the deposition of SGT films. It appeared from two-theta x-ray scans that the best films, as evident by intense film diffraction peaks and the absence of small second phase peaks, were synthesized at ratios of 9:1 and 19:1, suggesting that gas compositions between would also be suitable. These

Table 2.4**Results of Sputtering Gas Optimization Studies**

T_s (°C)	Gas Mixture (Ar:O ₂) ¹	d (200) (Å)	FWHM (200) Two- Theta scan (degrees)	FWHM (200) Rocking Curve (degrees)	EMPA
650	5:1	3.99	0.456	2.973	Sr _{0.53} Al _{0.44} Ga _{0.41} Ta ₁
675	5:1	3.99	0.397	2.821	Sr _{0.53} Al _{0.61} Ga _{0.38} Ta ₁
650	9:1	3.99	0.427	2.533	Sr _{0.53} Al _{0.45} Ga _{0.38} Ta ₁
675	9:1	3.97	0.606	17.025	Sr _{0.53} Al _{0.98} Ga _{0.35} Ta ₁
675	19:1	3.96	0.556	3.723	Sr _{0.53} Al _{0.91} Ga _{0.30} Ta ₁
650	19:1	3.96	0.614	3.467	Sr _{0.53} Al _{0.91} Ga _{0.27} Ta ₁
650	49:1	---	---	---	---
675	49:1	---	---	---	---

¹Total pressure = 50 millitorr

films appeared to have good c-axis orientation and sharp (200) peaks, indicating good crystallinity, although one film grown in the 9:1 ambient displayed a good deal of off orientation growth in the rocking curve pattern. Progression to a lower oxygen partial pressure (49:1) resulted in the loss of good film growth. Lattice expansion from the bulk Sr₂GaTaO₆ value was again evident. EMPA results from these films indicate that all are highly strontium deficient. The aluminum concentration is sometimes much greater than the gallium concentration. If both cations are assumed to occupy a Ga site, the occupancy of the B and B' sites are generally fairly close to 1:1, although there is no reason to assume ordering of the cations on the ideal sites in the films.

Table 2.5

Substrate Temperature and X-Ray Analysis for SGT 1-4

Deposition #	T _{substrate} (°C)	d (200) (Å)	FWHM (200) Two-Theta Scan (degrees)	FWHM (200) Rocking Curve (degrees)
SGT 1	675	3.976	0.326	4.151
SGT 2	650	3.985	0.347	2.986
SGT 3	625	4.0122	0.360	1.961
SGT 4	600	3.9981	0.462	3.459

2.3.3.3 Effect of MgO Substrate Temperature on SGT Physical Properties

i) *Film Crystallinity and Thickness.* With the optimization of the argon:oxygen ratio completed in the previous experiments, the effect of the substrate temperature on film growth, composition, and morphology was investigated. An Ar:O₂ ratio between 9:1 and 19:1 was desired when setting gas flows into the vacuum chamber. A measured ratio of 12.25:1 was achieved. This proved good for film synthesis in test runs, and was subsequently maintained for the entire series. Substrate temperatures of 675, 650, 625, and 600 °C were utilized in synthesis, and a step was made in the films with a mask to allow for thickness measurements and determinations of the film growth rates. For purposes of discussion, these films are labeled SGT 1-4 in the following text.

Two theta and rocking curve analysis on these films is summarized in Table 2.5. A decrease in cell dimensions with increasing temperature is evident. All films show an expanded lattice compared to the target. Two-theta FWHM measurements on the (200) peak of each film showed the peak widths increase with decreasing temperature, suggesting the presence of more strain or smaller particle sizes in the lower temperature films. Very small particles (on the order of 50 Å) could also cause the

Table 2.6**Film Thickness Data for SGT 1-4**

Deposition #	T _{substrate} (°C)	Deposition Time (hr:min)	Film Thickness (Å)	Growth Rate (Å / min)
SGT 1	675	4:04	2300	9.5
SGT 2	650	3:38	2200	10.0
SGT 3	625	4:00	1600	6.6
SGT 4	600	4:00	~450 ¹	~1.9

¹It is difficult to measure film thickness mechanically below approximately 1000 Å.

apparent shift in x-ray peak positions (10), which are evident in SGT 3 and 4 in comparison with 1 and 2. Rocking curve FWHM measurements showed the c-axis orientation to improve with decreasing temperature. It is interesting that better crystallinity, as suggested by sharper two-theta x-ray pattern peaks, correlates with poorer c-axis orientation. X-ray phi scans on the (220) peak of these films, given in Figure 2.7, show all to be crystalline in the a-b plane, as evidenced by the existence of 2 peaks spaced 90° apart in a 190 degree scan. None of these scans were optimized for maximum intensity, so peak intensities are not significant.

Film thickness data are summarized in Table 2.6. The deposition rate seems to be dependent upon the substrate temperature, with the rates of the films grown at higher temperatures (650 and 675 °C) being roughly comparable. The thickness data for SGT 4 is only an estimate, as the mechanical stylus is difficult to use to measure thicknesses below about 1000 Å. Film composition data from EMPA for these films is given in Table 2.7. As with the earlier films, these appear quite strontium deficient. Again, relatively high concentrations of impurity Al was found in the sample. The B and B' cations appear to be present in a roughly 1:1 ratio. These results are consistent with previous microprobe

Table 2.7**Film Composition Data for SGT 1-4**

Deposition #	T _{substrate} (°C)	EMPA
SGT 1	675	Sr. ₉₈ Al. ₃₁ Ga. ₄₇ Zn. ₁₀ Ta ₁
SGT 2	650	Sr. ₆₇ Al _{1.01} Ga. ₄₀ Zn. ₀₁ Ta ₁
SGT 3	625	Sr. ₇₂ Al. ₀₄ Ga. ₄₄ Zn. ₇₀ Ta ₁
SGT 4	600	Sr. ₇₄ Al. ₀₃ Ga. ₄₇ Zn. ₇₀ Ta ₁

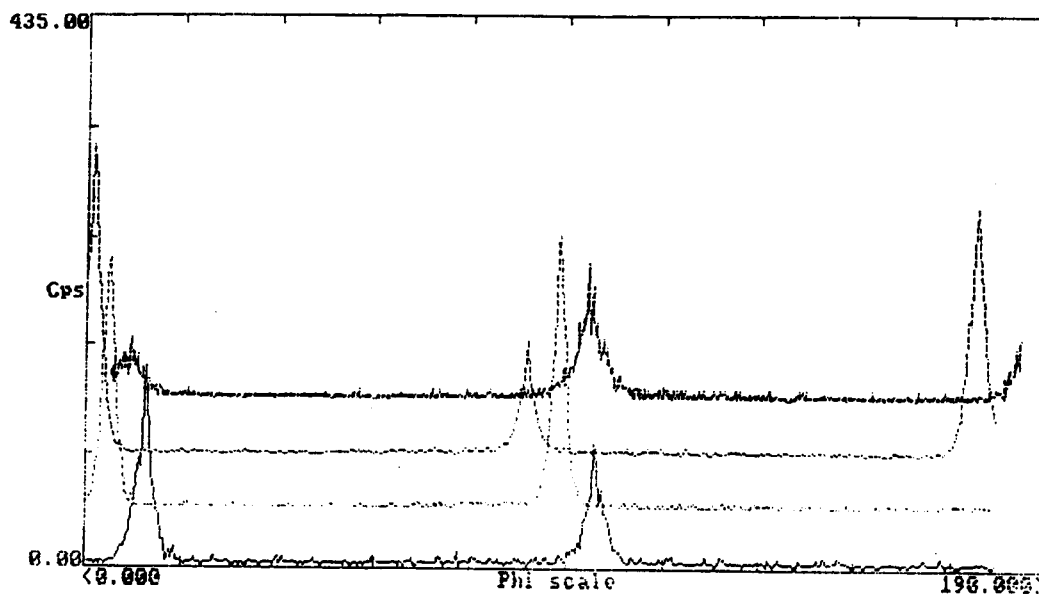


Figure 2.7 X-ray phi scans of SGT 1 (top), 2, 3, and 4, arranged top to bottom.

data. The strontium content is highest in SGT 1, which had the closest lattice constant to that of the target material. This again suggests that the lattice expansion is related to the presence of defects.

ii) Film Morphology The morphology of these films was investigated with SEM and AFM. The results from this study suggested an "island" morphology of film growth; i.e., regions of greater film growth surrounded by regions of lesser growth. The largest scale imaged was a 10 micron by 10 micron area, shown for each film in Figure 2.8. From the images, it is evident that SGT 1 has the smoothest surface. Some grainy regions are present, and some larger defects also appear. These appear as white spots on the film and are probably due to pinholes in the film surface. SGT 2 has perhaps the least uniform morphology. However, while large regions of the film are quite smooth, significant defects are also present. The features do not appear at any regular intervals or distribution on this scale, as they do in SGT 1. Statistics on mean and maximum feature height are given in Table 2.8 for each of the 4 films on this scale, and are given for both the whole sample area and the smaller box area outlined in the images. Comparison of the total area statistics with the box statistics for SGT 2 demonstrates the large difference between local morphology and overall morphology. SGT 3 shows the presence of a wider distribution of defects than SGT 1, and the statistics show the features to be rougher, both in the box and over the whole imaged area. SGT 4 has a very grainy, yet regular, morphology. All features in this image appear to be evenly distributed over the range of the image, unlike SGT 2 and 3.

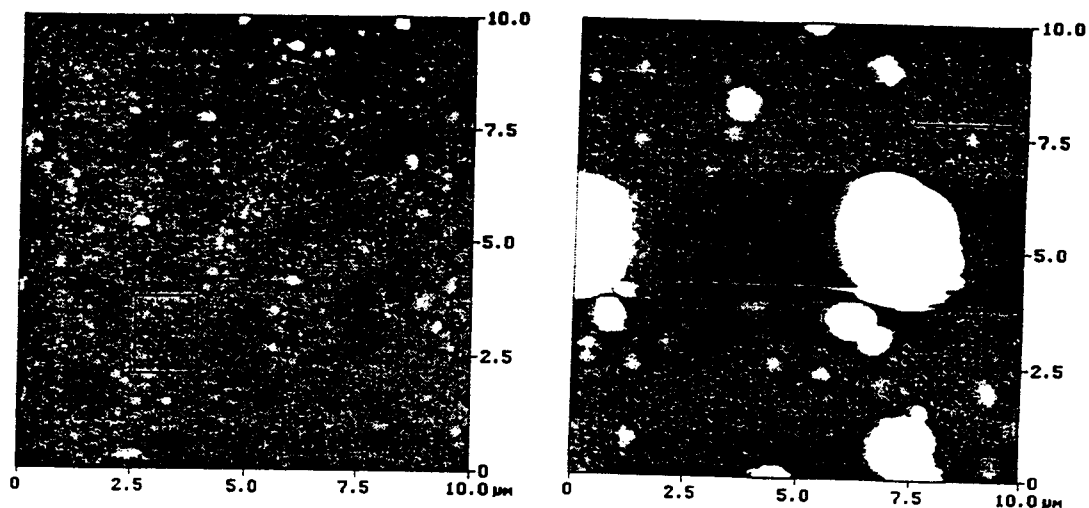
Table 2.8

Statistics from SEM Images of SGT 1-4

Film	Mean Feature Size (nm)	Maximum Feature Size (nm)	In Box: Mean Feature Size (nm)	In Box: Max. Feature Size (nm)
10 micron x 10 micron				
SGT 1	5.5	95	2	26
SGT 2	112	1640	10	88
SGT 3	7	241	6	66
SGT 4	14	330	13	122
0.5 micron x 0.5 micron				
SGT 1	1	11		
SGT 2	3	32	2	15
SGT 3	3	35	2	15
SGT 4	7	69		

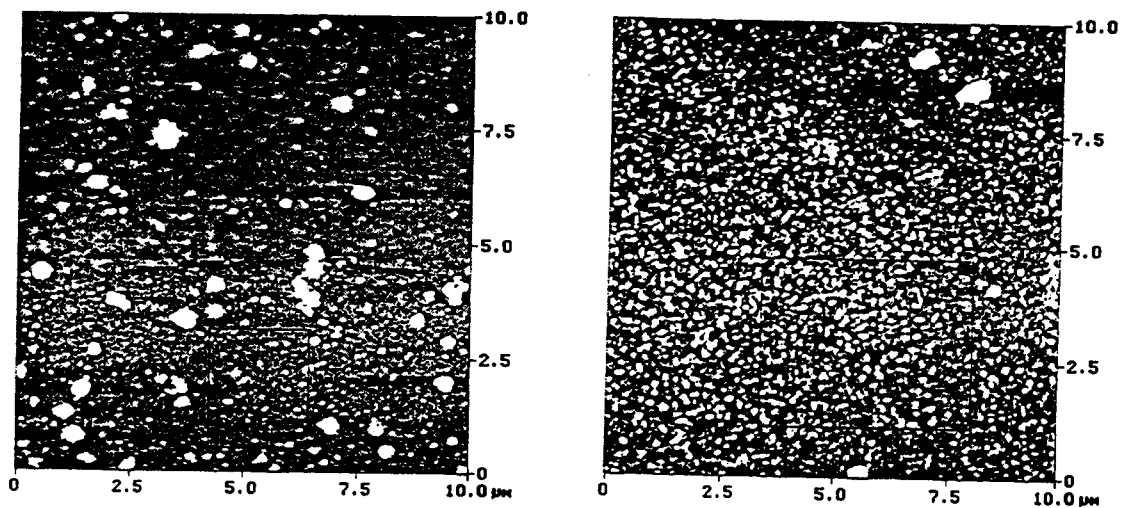
Figure 2.9 shows a 0.5 x 0.5 micron magnification of the previous SEM images of the four films. Just as with the larger area image, the smoothest morphology is found in SGT 1. One defect approximately 50-70 nanometers across appears in the image; the remainder of the image appears extremely smooth and featureless. The other films appear quite rough, and seem to display an island morphology. The image of SGT 2 at this scale was taken from one of the smoother areas of the film, and avoided the large defects. From the statistics, it is apparent that the film surfaces tend to smooth out at higher synthesis temperatures.

AFM images from each film are shown in Figure 2.10. Note the different vertical scale on each image. The different shaded regions are generated topographies. Once again, SGT 1 appears the smoothest film. With a vertical scale of 10 nm/division, SGT 1 appears to be composed of slight, smooth irregularities, and no abrupt features. SGT 2, 3, and 4 are



(a)

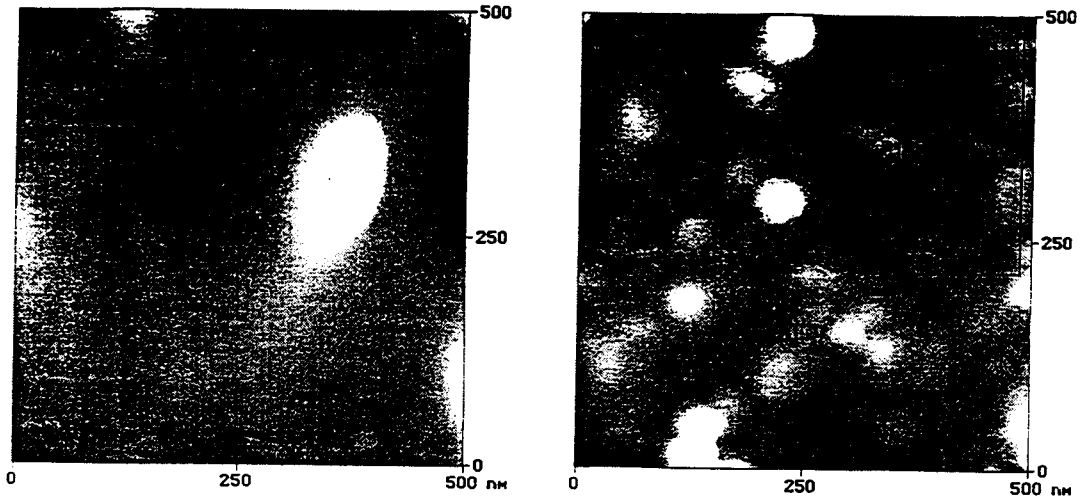
(b)



(c)

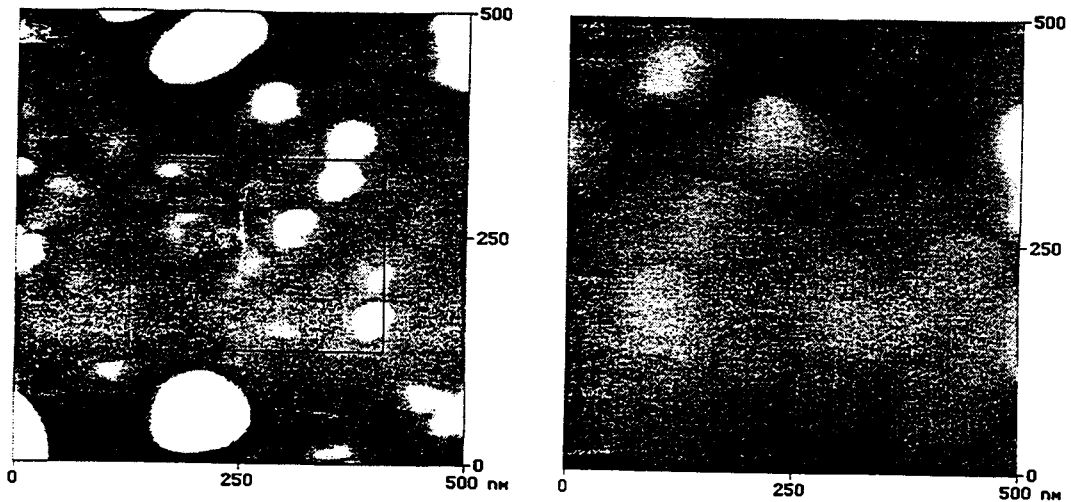
(d)

Figure 2.8 10 micron x 10 micron area SEM images of (a) SGT 1, (b) SGT 2, (c) SGT 3, and (d) SGT 4.



(a)

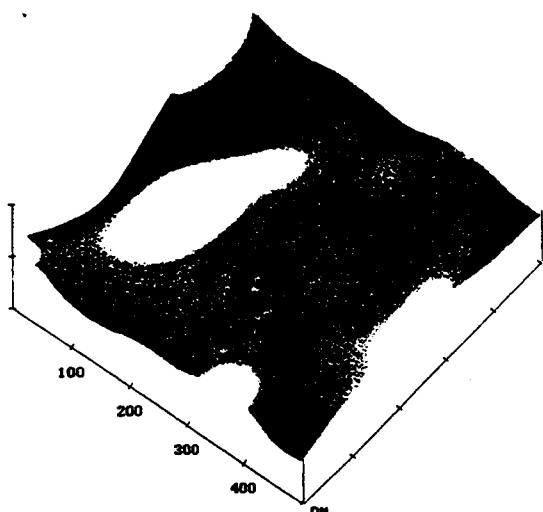
(b)



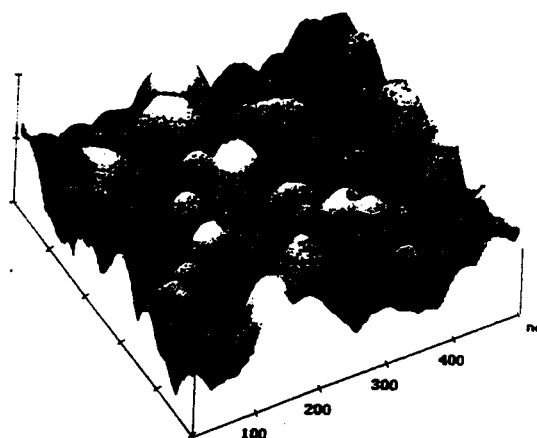
(c)

(d)

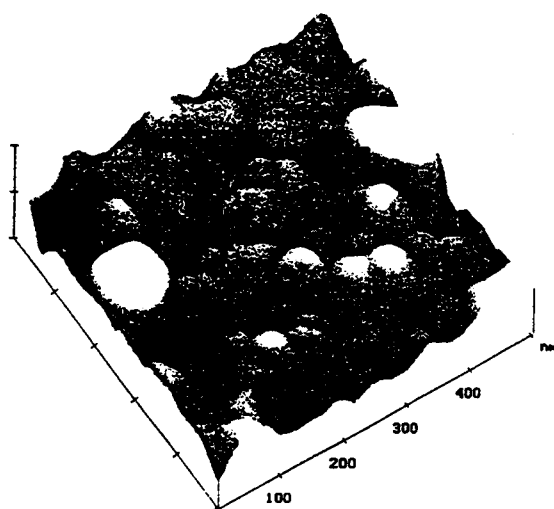
Figure 2.9 0.5 micron x 0.5 micron area SEM images of (a) SGT 1, (b) SGT 2, (c) SGT 3, and (d) SGT 4.



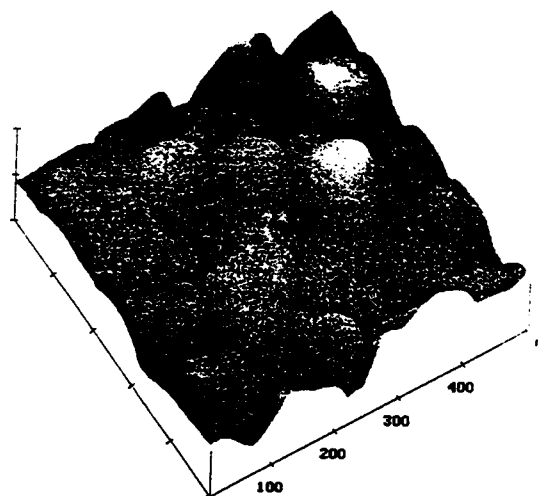
(a)



(b)



(c)



(d)

Figure 2.10 AFM images of (a) SGT 1 (vertical scale = 10 nm/division), (b) SGT 2 (20 nm/division), (c) SGT 3 (25 nm/division), and (d) SGT 4 (50 nm/division).

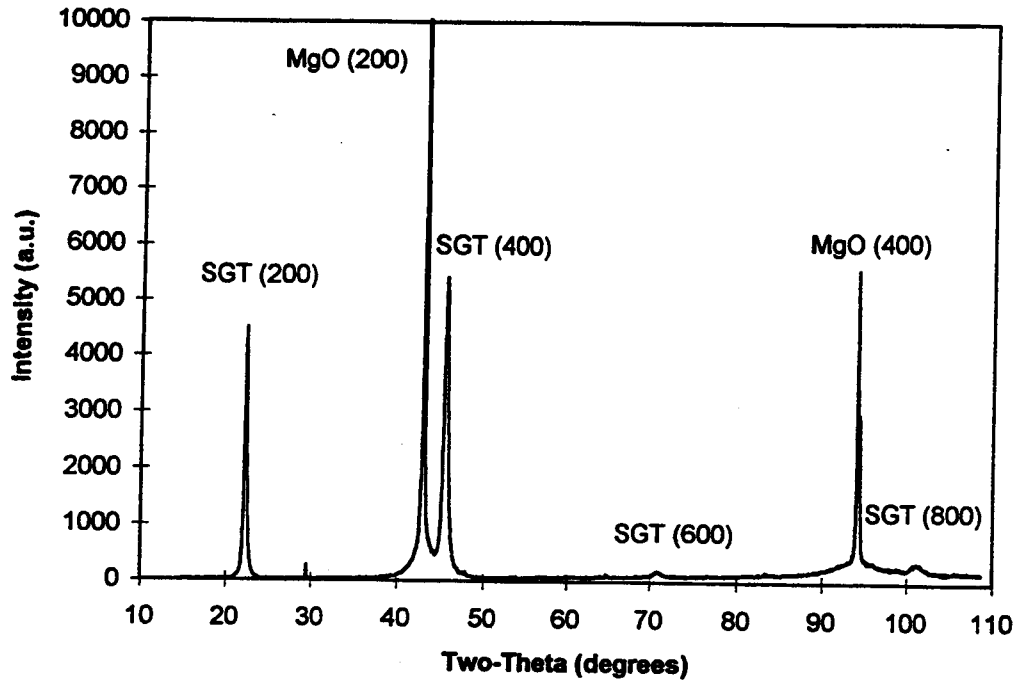
all composed of abrupt bumps, with a good deal of variation in height. The features in SGT 4 are about twice as large as those in SGT 2 and 3. The shapes of the features appear to be consistent from sample to sample. It is not known whether the rounded shape of the growth islands is a true image, or whether it is an artifact from a dull AFM tip.

iii) *Strain and Particle Size Analysis* Referring back to the two-theta x-ray data from these films, the pattern of SGT 2 is unique among all SGT films in that four peaks from the (h00) class of reflections are of measurable intensity, and are distinctly separated from the substrate peaks. The plot is given in Figure 2.11 (a). This allowed the calculation of the strain and average particle size in the film along the (h00) direction using a Williamson-Hall plot. This plot allows the extraction of crystallite size and strain (a unitless quantity defined as the change in cell constant/average cell constant) through measurements of the peak widths from a powder x-ray data set.

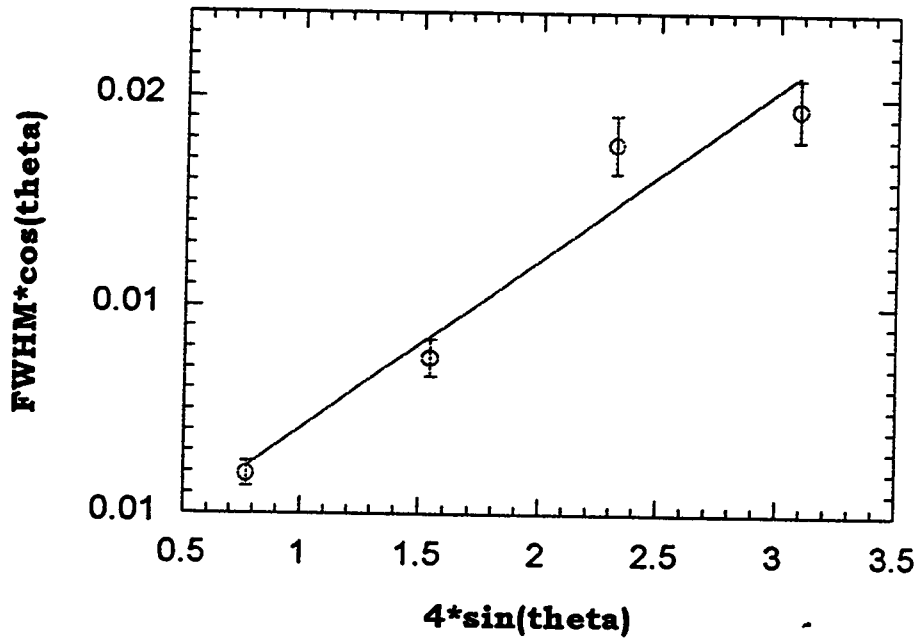
The function plotted is

$$\beta \cos \theta_k / (180 / \pi) = \lambda / \tau + 4\varepsilon \sin \theta_k \quad (2.1)$$

where β is the FWHM of the peak, θ_k is one half the angle two-theta, λ is the wavelength of the radiation, τ is the crystallite size, and ε is the strain. Plotting $\beta \cos \theta (\pi / 180)$ on the y-axis vs. $4 \sin \theta$ on the x-axis yields the strain as the slope of the plot and λ / τ as the y-intercept, from which the particle size is easily calculated. See reference 11 for a complete description of this analysis. The same analysis was performed on the target $\text{Sr}_2\text{GaTaO}_6$ pattern for comparison. The (200), (400), (600), and (800) peaks of the SGT 2 x-ray pattern were all fit using a standard



(a)



(b)

Figure 2.11 (a) Two-theta x-ray diffraction scan of SGT 2 showing the series of (h00) reflections, and Williamson-Hall plot of (b) SGT 2 film x-ray data. The slope of the line gives the strain in the film, and the particle size is calculated from the intercept. The film strain is approximately 5.3 times that of the bulk.

pseudo-Voigt 1 routine in the Siemens Diffrac-AT software package (12). The resulting Williamson-Hall plot is shown in Figure 2.11 (b). All points fall very close to the best fit line. The slope of the line gives the strain as .004, compared to a value of .0007 for the bulk. This shows the film to have a strain about 5 times that of the bulk. With a wavelength of 1.54056 for the Cu $K\alpha_1$ radiation, the particle size was determined to be about 521 Å along the (100) direction. The particle size in the bulk was found to be about 1377 Å. The film particle size suggests that about 3 grain boundaries exist between the substrate and film surface.

Attempts were made to refine the occupancies of the atomic positions in the film using the GSAS (General Structural Analysis Software) program (13), as the software allows refinement of data along particular crystallographic directions. The film peak profiles proved too difficult to fit using the profile functions in the software, and the refinement was impractical.

2.3.4 Sr_2AlTaO_6 Thin Films

Sr_2AlTaO_6 , like Sr_2GaTaO_6 , is an ordered double perovskite that crystallizes in the space group $Fm\bar{3}m$. The cell constant of this material is 7.794 Å, or $a/2 = 3.897$ Å. Once the SGT film growth conditions were optimized, attempts were made to synthesize SAT films under the same conditions. These attempts are summarized in Table 2.9. Depositions were again performed using a sputtering gas pressure of 50 mT, and an Ar:O₂ ratio of 12.25:1. The same temperatures as attempted in SGT film synthesis were tried for the SAT films. No SAT films grew at temperatures below 650 °C. The other temperature films are labeled SAT 1, 2, and 3 (650, 675, and 700 °C respectively) for the purpose of

Table 2.9

Growth Conditions and X-Ray Peak Analysis for SAT Films

Deposition #	T _{substrate} (°C)	d (200) (Å)	FWHM (200) Two-Theta Scan (degrees)	FWHM (200) Rocking Curve (degrees)
SAT 1	650	3.986	0.360	2.523
SAT 2	675	3.985	0.348	2.625
SAT 3	700	3.964	0.307	3.160

discussion. Trends in the x-ray analysis for the films shown in Table 2.9 are consistent with the trends observed in the SGT films. As the growth temperature increases, the (200) peak width decreases, showing improving crystallinity with increasing temperature. Also with increasing temperature comes an increase in the rocking curve width, revealing a greater amount of off-orientation growth. No film thickness data for these films were obtained, as they proved to be too thin to use the mechanical stylus reproducibly. All films were probably less than 1000 Å thick, despite 4 hour sputtering times. Therefore, the sputtering rates of SAT films are lower than those of SGT films at a given temperature. Phi scans performed on these films showed all to have good a-b plane crystallinity.

EMPA data for these films is given in Table 2.10. Because the SGT films from the previous section displayed a high concentration of Al as an impurity, the SAT films were examined for Ga as an impurity. The quantity of Ga found in the films was negligible in comparison with the quantity of Al (approximately one part per hundred). In addition, the films were checked for Zn, as sputtering experiments involving ZnO were being carried out alternately with the SAT depositions. The Zn

Table 2.10**Electron Microprobe Analysis Data for SAT Films**

Deposition #	T _s (°C)	Stoichiometry
SAT 1	650	Sr _{0.84} Al _{0.62} Zn _{0.26} Ta ₁
SAT 2	675	Sr _{0.71} Al _{0.63} Zn _{0.60} Ta ₁
SAT 3	700	Sr _{0.82} Al _{0.51} Zn _{0.11} Ta ₁

contamination in the chamber after cleaning was high enough that the quantity of Zn in the films was not negligible, ranging from one fifth of the concentration of Al to an equal concentration. X-ray diffraction patterns seem to show a single phase, with peak positions that would be expected for a structure similar to the bulk structure of SAT, and no ZnO peaks were evident in any of the patterns. It is therefore possible that the Zn is incorporating itself into the structure. As Zn²⁺ is not known in a 12 coordinate environment, (the Sr²⁺ is in the perovskite structure), and the ionic radius of Zn (0.74 Å, C. N. 6) is very small compared to that of Sr (1.44 Å, C. N. 12), it is likely that the Zn occupies the B cation site. Consistent with previous microprobe on SGT films, the SAT films are strontium deficient. The B:B' cation ratios are further from 1:1 than for the SGT films.

SEM studies were performed on these films over areas of 10 x 10 microns and 0.5 x 0.5 micron, with the exception of SAT 3, which was scanned at 5 x 5 microns instead of 10 x 10. The results are tabulated in Table 2.11. The results are interesting in that, when comparing a small film area to a larger one, the trends in increasing roughness are reversed. From the 10 x 10 micron images, shown in Figure 2.12, the surface seems to become smoother as the substrate temperature is increased. The mean feature size is approximately the same for all films, but the

Table 2.11

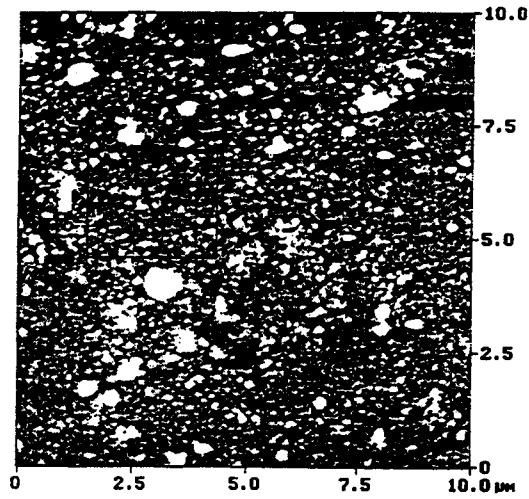
Statistics from SEM Images of SAT 1, 2, and 3

Film	Mean Feature Size (nm)	Maximum Feature Size (nm)	In Box: Mean Feature Size (nm)	In Box: Max. Feature Size (nm)
10 x 10 micron				
SAT 1	7	209	5	59
SAT 2	6	94	4	58
SAT 3 ¹	7	74	---	---
0.5 x 0.5 micron				
SAT 1	3	27	---	---
SAT 2	3	34	---	---
SAT 3	5	47	---	---

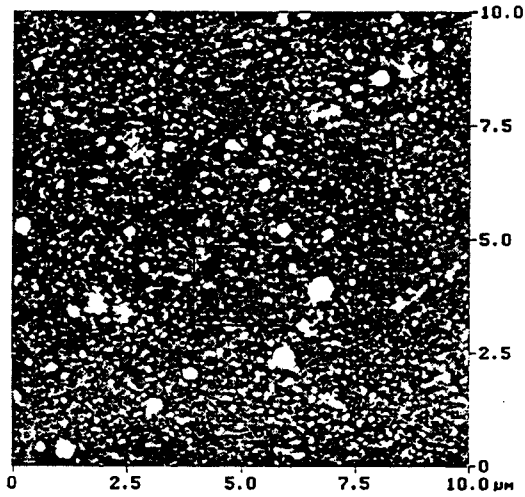
¹Statistics for SAT 3 are from a 5 x 5 micron area.

maximum feature size decreases with increasing temperature, suggesting the extra thermal energy allows the atoms to migrate more after adsorbing to the growing film surface, thereby smoothing out the film. However, on the 0.5 micron scale (Figure 2.13), the order is reversed, with SAT 3 showing the greatest degree of roughness. This film does show the most consistency in surface characteristics between the two scales, suggesting that higher temperatures promote the growth of a more homogeneously structured film. SAT 1 and 2 appear to have a more irregular topography, with a wider variety of defect sizes, spaced at less regular intervals, in comparison with SAT 3. Most likely, the smaller area images were taken from the relatively smooth portions of SAT 1 and SAT 2.

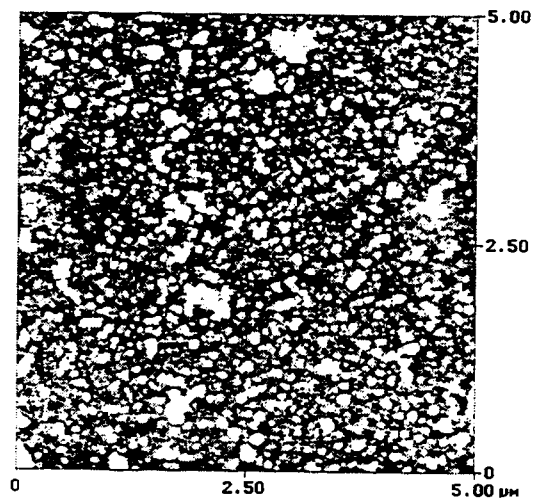
AFM images of the films show all of the film surfaces to be irregular. The images are given in Figure 2.14. All consist of the rounded bumps seen in the lower temperature SGT films. Once again, it



(a)

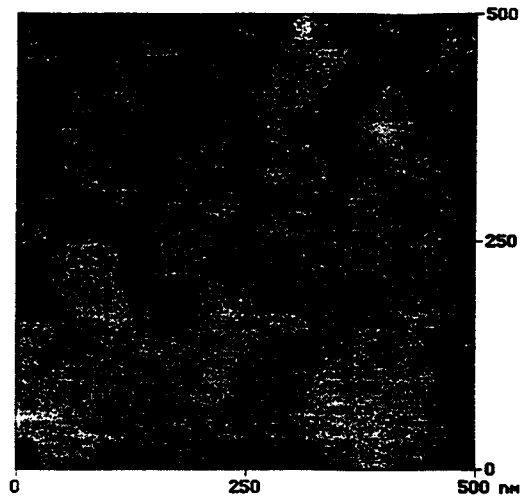


(b)

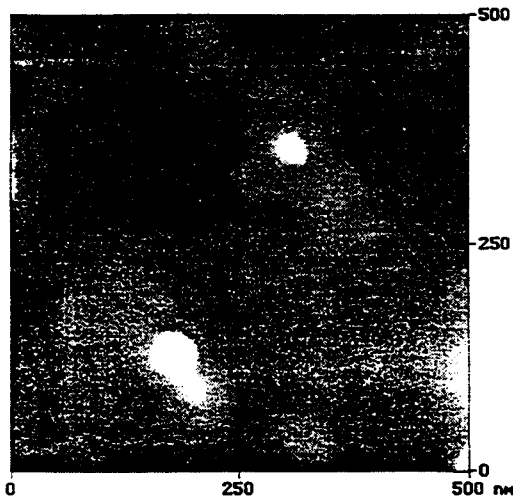


(c)

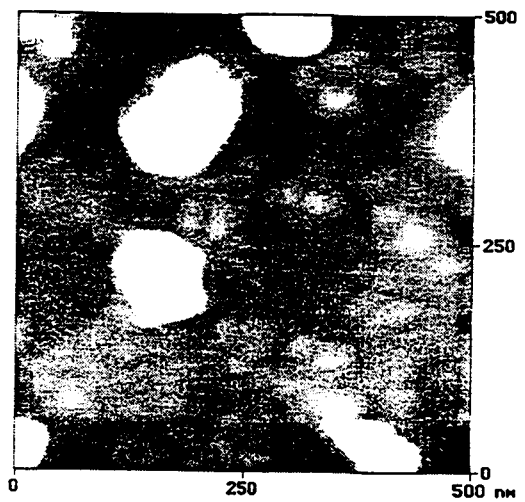
Figure 2.12 10 micron x 10 micron area SEM images of (a) SAT 1 (650 °C), (b) SAT 2 (675 °C), and (c) SAT 3 (700 °C).



(a)

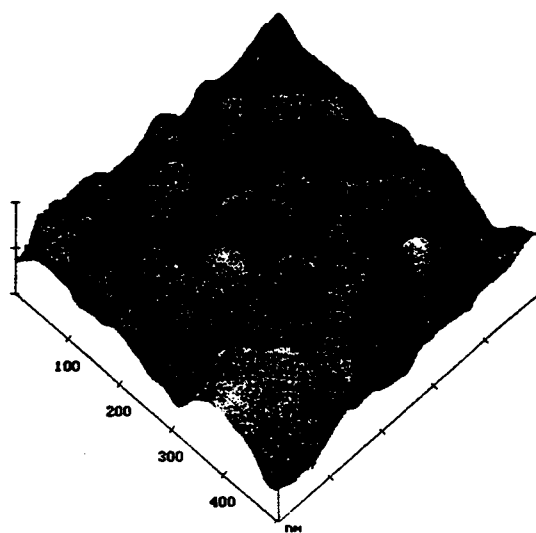


(b)

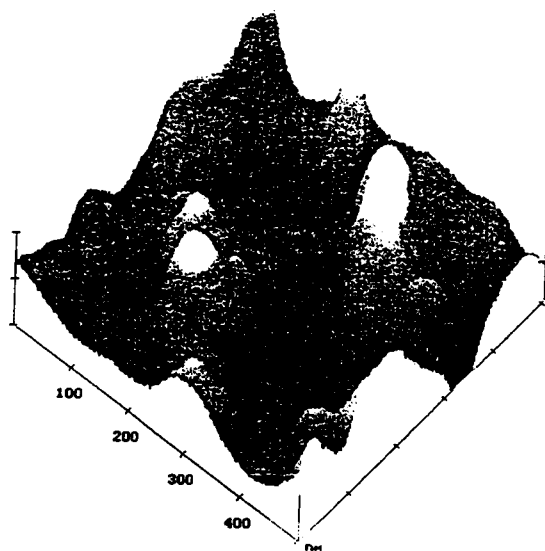


(c)

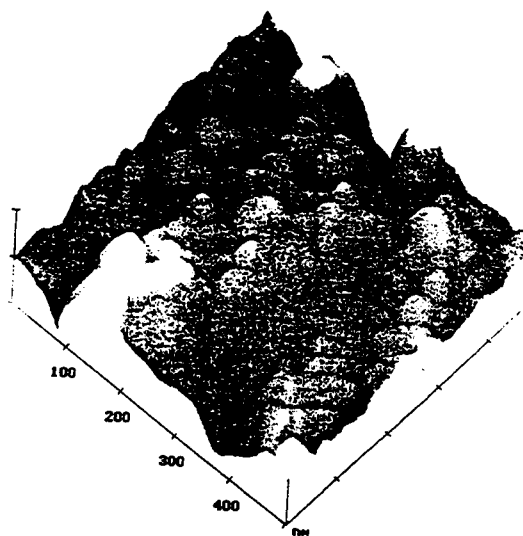
Figure 2.13 0.5 x 0.5 micron area SEM images of (a) SAT 1 (650 °C), (b) SAT 2 (675 °C), and (c) SAT 3 (700 °C).



(a)



(b)



(c)

Figure 2.14 AFM images of (a) SAT 1 (vertical scale=30 nm/division), (b) SAT 2 (10 nm/division), and (c) SAT 3 (20 nm/division).

is uncertain whether the roundness of the features is physically present, or an experimental artifact from a dull AFM stylus. From the vertical scale of the measurements, it appears that SAT 2 has the smoothest morphology, but recall that, on a larger scale, the surface of this film is quite irregular. This image once again was taken from one of the more ideal surface regions rather than from a defect heavy area. The vertical scale needed to image this film was 10 nm/division, although some of the peaks pinned the top of the scale. Some of the peaks did the same with the SAT 3 image, although the vertical scale was 20 nm/division. A scale of 30 nm/division was needed to clearly image the SAT 1 surface.

2.3.5 YBa₂Cu₃O₇ / Double Perovskite Thin Film Multilayer Structures

In the previous set of experiments, it was determined that SGT and SAT were possible candidates for use in multilayer structures with superconducting thin films. In this section, results from experiments on making multilayer thin film structures are presented. YBCO films on LaAlO₃ substrates were obtained from Conductus, Inc. Attempts to synthesize thin films of Sr₂GaTaO₆ and Sr₂AlTaO₆ via RF magnetron sputtering on these substrates were made in both off-axis and on-axis configurations. The runs attempted are summarized in Table 2.12. The films were grown using the sputtering gas conditions found to be optimal in the previous experiments (50 mT, 12.25:1 Ar:O₂). The RF power was not varied from the set value of approximately 50 W. The substrates were heated at a rate of 10 °C/minute to the deposition temperature in a 200 millitorr oxygen ambient. Cooling was performed more slowly (5 °C/min.) to 400 °C, where the films were held for a 6 hour anneal in approximately 20 torr oxygen. From here, the cooling rate was increased

Table 2.12

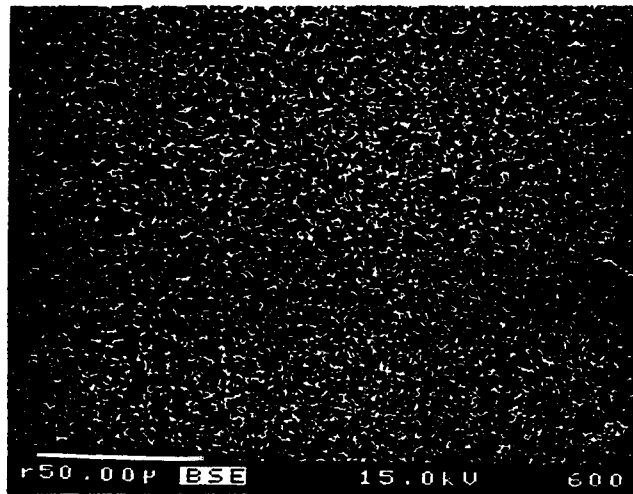
Growth Conditions and Results of LaAlO_3 / $\text{YBa}_2\text{Cu}_3\text{O}_7$ /SGT and SAT Thin Film Multilayers ($x=2.5$ inches except where noted)

Deposition #	$T_{\text{substrate}}$ (°C)	Deposition Geometry	Desired Phase Visible in X-ray?	EMPA / Other Comments
YBCO/SGT 1	675	on-axis $x = 2.0$ in	no	$\text{La}_{0.71}\text{Al}_{4.55}$ $\text{Y}_1\text{Ba}_{1.85}\text{Cu}_{1.03}$ $\text{Sr}_{5.5}\text{Ga}_1\text{Ta}_{3.57}$ Etched YBCO film.
YBCO/SGT 2	675	on-axis	yes	$\text{La}_{0.66}\text{Al}_{2.82}$ $\text{Y}_1\text{Ba}_{1.43}\text{Cu}_{1.66}$ $\text{Sr}_{3.69}\text{Ga}_1\text{Ta}_{3.57}$ $d(200) = 3.99 \text{ \AA}$
YBCO/SGT 3	675	on-axis	yes	$T_c = \sim 80 \text{ K}$ $d(200) = 3.99 \text{ \AA}$
YBCO/SGT 4	675	off-axis	yes	$\text{La}_{0.63}\text{Al}_{3.36}$ $\text{Y}_1\text{Ba}_{1.72}\text{Cu}_{2.16}$ $\text{Sr}_{5.89}\text{Ga}_1\text{Ta}_{2.71}$ $d(200)=4.02 \text{ \AA}$ $T_c \sim 87\text{K}$
YBCO/SAT 1	700	on-axis	no	$\text{Ba}_2\text{Sr}_2\text{Al}_2\text{O}_7$ was only phase grown.
YBCO/SAT 2	700	on-axis	no	No film grown.
YBCO/SAT 3	700 (4 hours or less)	off-axis	no	$\text{Y}(\text{Ba},\text{Sr})_2\text{Cu}_3\text{O}_7$ only phase.
YBCO/SAT 4	700	off-axis	yes	(200), (400) weak but present. $d(400) = 2.02 \text{ \AA}$

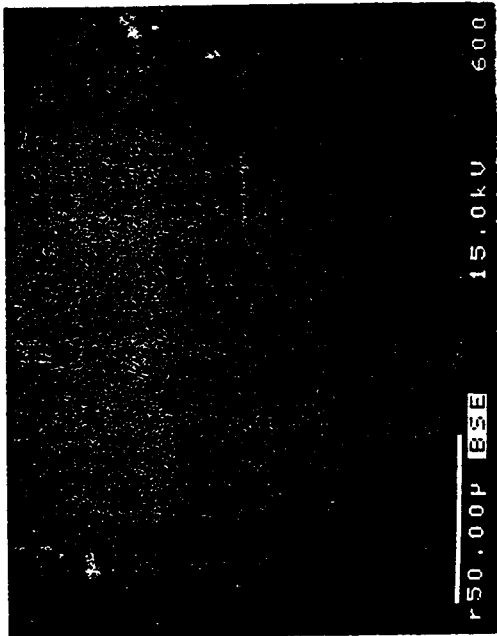
to 10 °C/min. to room temperature. All films were characterized by x-ray diffraction, and selected films by EMPA, T_c determination by mutual inductance, etch resistance tests, and x-ray phi scans.

X-ray and microprobe results from these depositions are summarized in Table 2.12. The results from the YBCO/SGT multilayer films were encouraging. An attempt to deposit an SGT film on YBCO in an on-axis geometry with the heater 2.0 inches from the target surface resulted in the etching of the YBCO film. Moving the substrate to a distance of 2.5 inches resulted in good SGT film growth and no etching of the YBCO. SEM photographs of this surface, shown in Figure 2.15, revealed a very regular surface, more regular than those of SGT films on MgO. Small defects, possibly pinholes, are present, but in smaller densities than the SGT films on MgO. An on-axis film (YBCO/SGT 3) was synthesized for analysis at Conductus. T_c measurements [Figure 2.16 (a)] revealed the onset of the superconducting transition to be about 80 K (87K prior to SGT deposition). The lattice constants of both of these films were expanded relative to bulk Sr_2GaTaO_6 , as with films on MgO. The EMPA results for these films were surprising, as the films were found to be strontium rich. However, the substrate stoichiometry also appears to be far off the ideal 1:1 La:Al ratio, which is highly unlikely in large commercial single crystals; this suggests that these stoichiometries are questionable.

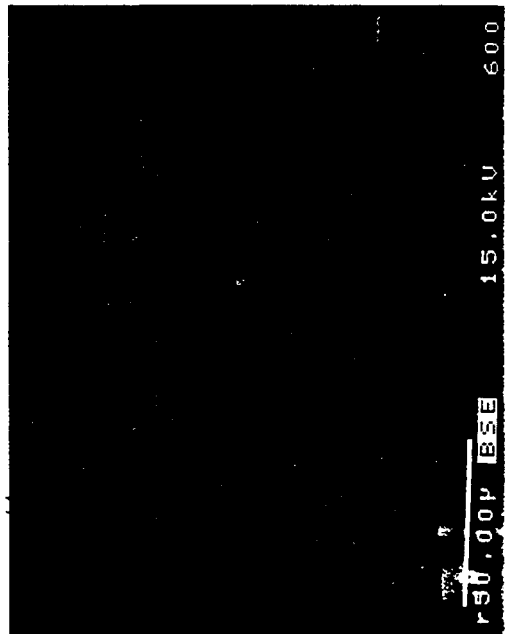
Off-axis SGT films were also successfully grown on YBCO. EMPA verified the presence of all elements. The lattice constant was more greatly expanded in this film than in the on-axis films. SEM photographs revealed a very smooth surface, much like that of the on-axis film. The T_c of the YBCO beneath this film was broadened, but the onset was



(a)

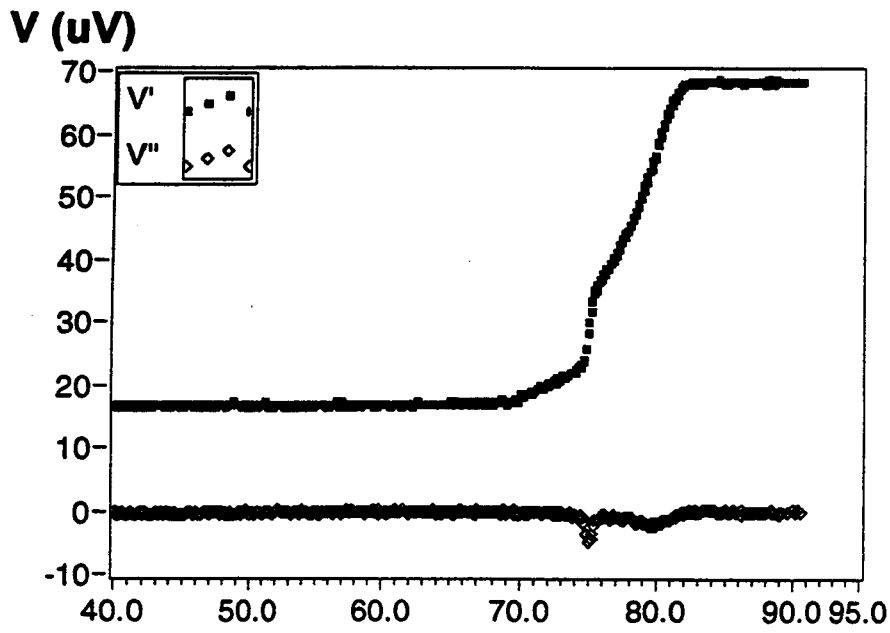


(b)

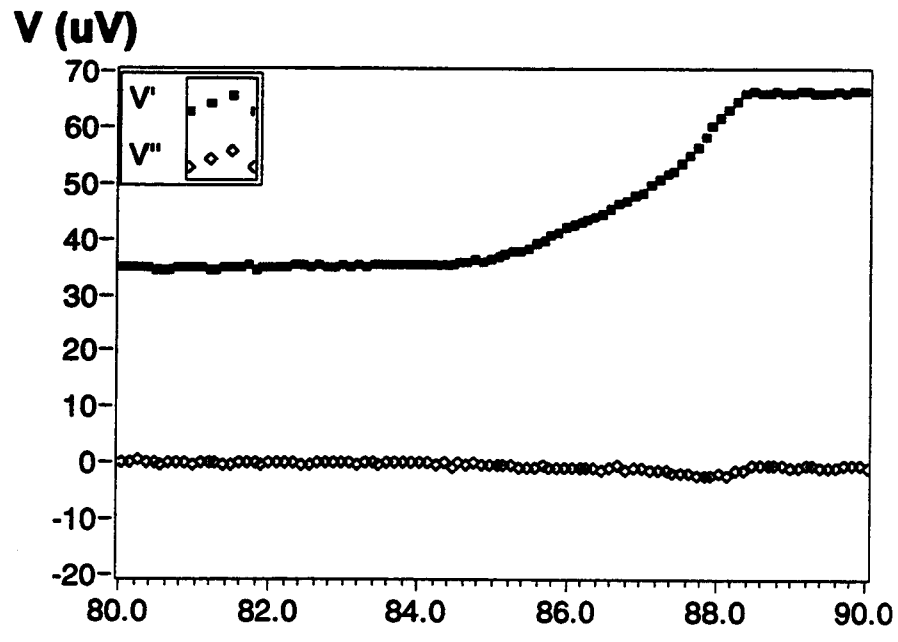


(c)

Figure 2.15 SEM photographs of (a) YBCO/SGT 1, (b) YBCO/SGT 2 (both on-axis, and (c) YBCO/SGT 4 (off-axis). (a) and (b) were synthesized on-axis, and (c) was off-axis. Notice the etched YBCO surface in (a). This was remedied in (b) by moving the substrate farther from the sputtering gun.

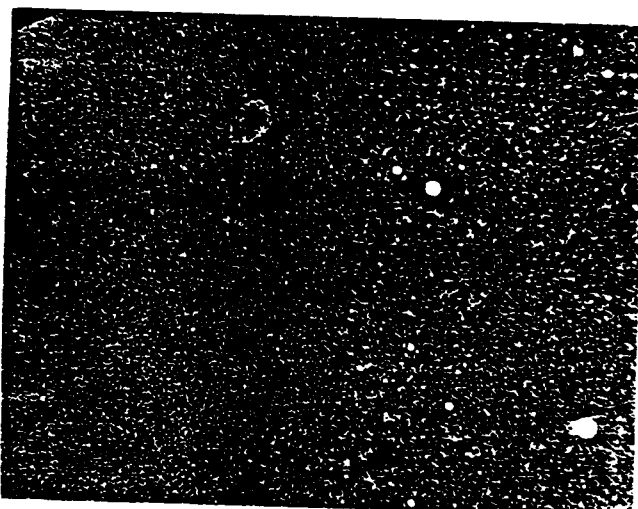


(a)

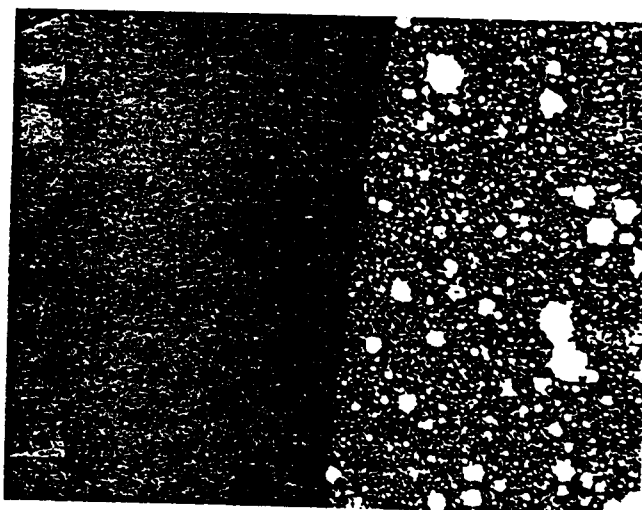


(b)

Figure 2.16 T_c plot of SGT films deposited on a LaAlO_3 substrate/YBCO film structure by (a) on axis and (b) off-axis sputtering.



(a)



(b)

Figure 2.17 SEM photographs from YBCO/SGT film etch tests. The left side of the films were masked prior to the etch. The resulting films were backlit for the photograph to illuminate pinholes where the YBCO was etched away. Figure (a) is from the on-axis film, and (b) is from the off-axis.

higher than that of the on-axis grown sample [87 K, shown in Figure 2.16 (b)]. However, an etch rate test performed on the superconducting layer in this structure and the on-axis grown structure showed the latter to etch at a much slower rate. This suggests that the on-axis grown dielectric film is thicker and more structurally homogeneous than the off-axis film, resulting in less penetration of the etchant solution. SEM photographs of the two films after the etch test was performed are shown in Figure 2.17. The right side of each film given in the figure was exposed to the etch, and the left was protected by a mask. After etching, the films were backlit to illuminate pinholes, which become visible as the YBCO is etched from these regions. The photographs show the on-axis film to have only a few pinholes, while the off-axis film has many.

The epitaxy of the on-axis and off-axis deposited SGT films on YBCO was verified by x-ray phi scans, shown in Figure 2.18. This figure contains two pairs of traces. The top trace in the top pair is a phi scan of the YBCO (220) peak, and just beneath is a scan of the SGT (220) peak from the on-axis film. The positions of the peaks are offset by about 4° , showing that the SGT film grew only a small degree off orientation relative to the YBCO. The bottom two traces depict the same relationship for the off-axis film. The overlapping YBCO and SGT peaks show that the SGT film grew epitaxially.

Less success was met with attempts in synthesizing SAT films on the YBCO/LaAlO₃ substrates. Attempts at growing on-axis films resulted in the formation of Ba₂Sr₂Al₂O₇. Results from attempts at on-axis film growth were no more encouraging, with only one film showing evidence of a (400) peak, and none showing a (200). The films were not characterized by microprobe or T_c measurements.

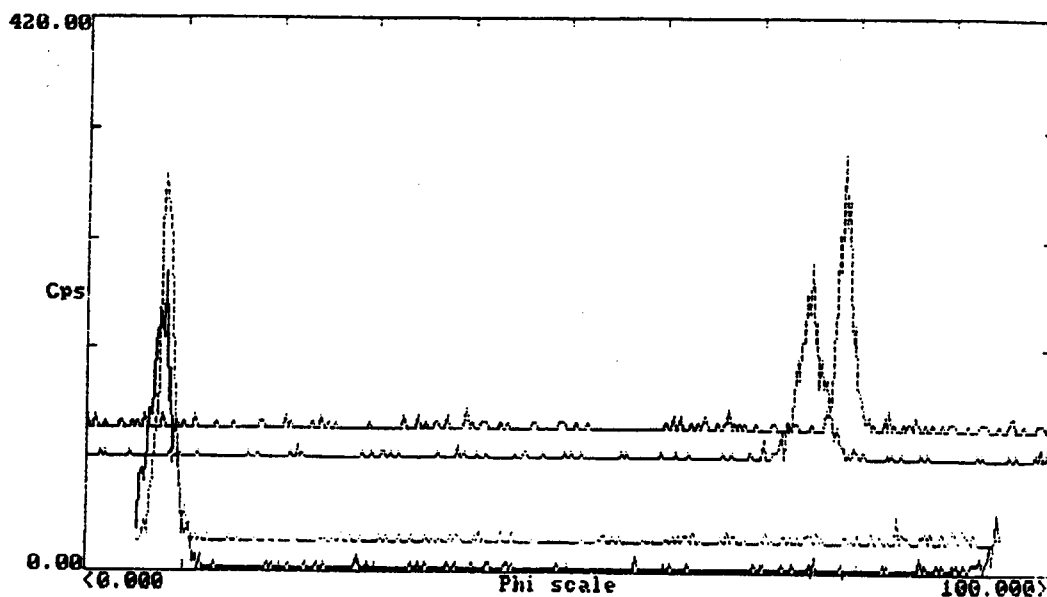


Figure 2.18 Phi-scans of YBCO and SGT (220) peaks showing the growth orientation of the film relative to the substrate for the on-axis (top traces) and off-axis (bottom traces) films.

2.4 Discussion

Experiments performed with the compounds Ca_2MgWO_6 and Sr_2MgWO_6 showed that these compounds are not suitable for applications involving heterostructures with superconducting thin films. The calcium compound is of too low a symmetry to be a good candidate. Films with peaks matching positions of some of those of the bulk were grown, but the high number of peaks found in a small two-theta range of the bulk makes the films extremely difficult to analyze. If films were grown, it is very likely that they would grow with multiple orientations, and have unpredictably located grain boundaries. Since the dielectric constant of a non-cubic material is an anisotropic property, it would

likely change at each grain boundary. This would make the design of precision microwave electronics using this material impossible. Films of Sr_2MgWO_6 were initially of more interest. The symmetry of the material is tetragonal; this is of equal or higher symmetry than many substrates in use or under study today. The pseudocubic lattice constant (3.945 \AA) is small enough to reduce strain in superconducting films grown on the material. However, all attempts at synthesizing this film resulted in the growth of SrWO_4 and MgWO_4 . The composition of the products show that strontium is either not sputtered from the target at the same rate as the magnesium and tungsten, or does not adsorb to the growing film surface as well. In either case, the lack of strontium in the growing film probably causes the other oxides to form. Strontium deficiencies were noticed in other films, but they seemed to be less affected by the off-stoichiometry compositions. For these reasons, the films sputtered from the A_2MgWO_6 targets were determined to be unsuitable for use in applications with high temperature superconducting thin films.

Films of the cubic double perovskite family $\text{Sr}_2\text{BB}'\text{O}_6$, with $\text{B}=\text{Al}$ or Ga and $\text{B}'=\text{Nb}$ or Ta , proved to be the most potentially applicable of those

studied in this investigation. The niobates were not studied in the same detail as the tantalates, but are definitely of high interest due to their predicted low dielectric constant. Because niobium has fewer electrons than tantalum, it is expected that the niobium 5^+ ion is less polarizable than the tantalum 5^+ . Indeed, in referring to Shannon's table of ion polarizabilities (14), the ion polarizability of Nb^{5+} is 3.98 \AA^3 , while that of Ta^{5+} is 4.75 \AA^3 . With all other ions in the structure remaining the same,

Table 2.13

Predicted Polarizabilities and Dielectric Constants of $\text{Sr}_2\text{BB}'\text{O}_6$ Double Perovskites

Compound	Polarizability (\AA^3)	$\epsilon_{\text{calculated}}$
$\text{Sr}_2\text{AlNbO}_6$	25.30	1.865
$\text{Sr}_2\text{AlTaO}_6$	26.06	1.898
$\text{Sr}_2\text{GaNbO}_6$	26.01	1.854
$\text{Sr}_2\text{GaTaO}_6$	26.77	1.884

the dielectric constant should be lower for the niobates. Similarly, the use of aluminum instead of gallium on the 3^+ site may be expected to have a similar effect, as the ion polarizability of Al^{3+} is 0.79 \AA^3 , while that of Ga^{3+} is 1.50 \AA^3 . The predicted molecular polarizabilities, calculated using values from Shannon's table, are given in Table 2.13. The Clausius-Mossotti equation predicts the dielectric constant to scale as a function of α/V_m (where α is the polarizability and V_m is the molar volume), rather than just as a function of the polarizability. Therefore, a larger unit cell can compensate for a larger polarizability. The calculated values predict that the lowest dielectric constant would be found in SGN, followed by SAN, SGT, and SAT. Higher temperatures seem necessary to synthesize the niobate films. At a temperature of $700 \text{ }^\circ\text{C}$, the SGN film grew in the (110) direction only. At $725 \text{ }^\circ\text{C}$, both (110) and (100) oriented materials were evident, and a temperature of $750 \text{ }^\circ\text{C}$ resulted in the growth of a purely (100) oriented film. The high temperatures are not a problem in themselves for film growth, and should not affect the use of the material as a buffer layer substrate. However, attempts at growing SAT films on the YBCO/ LaAlO_3 substrates at these temperatures resulted in a reaction between the superconducting and dielectric film

materials, and the formation of undesired impurity phases. Therefore, it is desirable to keep the synthesis temperature as low as possible if the film is to be used in direct contact with YBCO. The tantalates, especially SGT, proved easier to grow at lower temperatures.

Films of SGT were synthesized at a range of temperatures and gas compositions, allowing the conditions to be optimized. It was found that the best Ar:O₂ ratio for the synthesis of these films was between 9:1 and 19:1. For subsequent experiments, a value intermediate to these two compositions was used (12.25:1) with good results. In the x-ray results, it was found that the width of the (200) peak in the two-theta scan decreases with increasing film growth temperature while the width of the rocking curve pattern increases with increasing growth temperature. This suggests that at lower temperatures, the films have smaller particle sizes or higher strain, or both. In the higher temperature films, particle sizes may be larger, or strain may be lessened, but the films grow more off orientation. From the microprobe data, the films are again very strontium deficient. This cation deficiency is perhaps the cause of the observed unit cell disparity between bulk and thin film samples; a shift of the (200) peak to higher d-spacings is present in all film x-ray patterns. Some kind of compensation would be necessary to account for charge balance with the presence of cation vacancies. Oxygen vacancies would be the most likely candidate. The strain caused by the film/MgO lattice mismatch may additionally expand the films. Thicker films showed less expansion than thinner films, and also sometimes showed increased strontium content, further suggesting that vacancies result in the observed lattice expansion.

Structure factor calculations were performed to examine the effect of strontium deficiency on a calculated x-ray pattern. From electron density considerations, it is expected that a decrease in the strontium occupancy should result in an increase of the (200) and (600) x-ray peaks relative to the (400). Peaks from the film pattern were fit with software to obtain intensities. It was found that the film (200) intensity was higher in comparison to the (400) intensity relative to the bulk phase. Using a model structure and calculating theoretical intensities, all four visible (h00) reflection intensities could be fit by varying the A and B cation site thermal parameters and the Sr occupancy. The Sr site occupancy was calculated to be 0.8 with this method. The resulting thermal parameters were too high to be a physically meaningful measure of thermal motion ($B=8$ for the A site, 4.5 for the B site). This possibly signifies a great degree of positional disorder in the structures.

The substrate temperature was shown to affect other variables in the SGT films, such as film growth rate. The growth rates for the 675 and 650 °C films are fairly similar, but further decrease in temperature (holding all other deposition variables constant) greatly reduces the film growth rate, until it is approximately a factor of 5 lower at 600 °C. Film morphology was also affected to a large degree by the growth temperature. From the SEM and AFM images, the 675 °C film appears the most uniform. This is expected, as the higher temperatures allow adsorbed atoms to migrate more readily on the growing film surface, resulting in more even film growth. An even surface is desired in a buffer layer, as planarization of a rough substrate surface may improve subsequent film growth. It is also beneficial to grow this buffer layer at as low a temperature as possible to minimize the possibility of reactions

between the buffer layer and the substrate, or any films being grown in direct contact with the buffer layer. The fact that thick and smooth SGT films could be synthesized at a relatively low temperature is encouraging.

Good quality SAT films have been reported previously in the literature, but were grown by metalorganic CVD (5) and laser ablation (6). No report of synthesis by sputtering has yet been published. In this work, many of the same trends found in the SGT films grown at different temperatures were evident in the SAT films as well. The EMPA data shows the films to once again be quite strontium deficient. The target stoichiometry was also examined by EMPA, and found to be correct. A group at Conductus reported the same strontium deficiency problem in RF-magnetron sputtered SAT films (15). They reported progress in solving the problem by changing the geometry of the sputtering system. As the substrate was moved closer to the target, the strontium content seemed to increase, and even approach that of the bulk.

As the growth temperature increased for the SAT films, the (200) peak grew sharper, but further off orientation, as in the SGT films. With the increase in temperature also came a decrease in the lattice constant. However, the lattice constant never came as close to the bulk value (closest film=7.928 Å, bulk=7.794 Å, difference=0.134 Å) as for the SGT films (closest film=7.952 Å, bulk=7.898 Å, difference=0.054 Å). Furthermore, the films proved to be too thin to get good mechanical thickness measurements. Williamson-Hall analysis was not possible on these films, as either the (600) and (800) film peaks were not visible in the pattern (both are of very small intensity), or the (400) and (800) peaks were on the shoulder of a saturated substrate peak, and were therefore impossible to fit with available software. SEM and AFM images revealed

the surface of these films to be rougher than those of the SGT films. Moreover, the highest substrate temperatures did not result in smooth films, but did result in reactions with YBCO. Because of the rough morphology of the films, and the higher temperatures necessary to grow these films in comparison with the SGT films, the SAT films seem less suitable for use as a buffer layer when grown by RF sputtering. It is still an attractive candidate for a buffer layer grown by other methods, as reported previously in the literature.

The results of the SGT/YBCO multilayer films on lanthanum aluminum oxide are encouraging. The on-axis growth of this structure preserved the superconductivity of the YBCO, although the T_c was depressed to a greater degree than that of other heterostructures reported (6). Optimization of the synthesis conditions could possibly remedy this. The film appeared quite smooth by SEM, and the pinhole density, as measured qualitatively by the etch resistance of the YBCO inner layer, was low. The off-axis growth of the SGT on YBCO also resulted in what appeared to be a good film by x-ray and SEM analysis, but the etch test revealed a higher concentration of holes in the film. The T_c of the YBCO in this heterostructure was not as severely depressed as that of the on-axis SGT film, but the transition range was broadened. Another interesting aspect of these depositions was that the lattice constant of the SGT was not closer to the bulk than the SGT films grown on MgO. The periodicity of the YBCO lattice, if it is serving as the template for the SGT film growth, should result in compressive strain in the growing film, as the lattice constants, and therefore the distances between good adsorption sites, are smaller for YBCO than the interatomic distances in SGT. However, it was found that the SGT film

still had an expanded lattice. This supports the conclusion that intrinsic defects are the primary cause of the lattice expansion in the structure. It would be desirable to minimize these vacancies, as the resulting defects may have detrimental effects on the dielectric behavior. It is encouraging that the cation occupations can be adjusted through refinements in the geometry of the sputtering system. The SAT/YBCO experiments were not as successful, as most attempts resulted in reactions between the superconductor and dielectric films.

2.5 Conclusions

Experiments on growing buffer layer thin films of the materials $\text{Sr}_2\text{AlNbO}_6$, $\text{Sr}_2\text{AlTaO}_6$, $\text{Sr}_2\text{GaNbO}_6$, and $\text{Sr}_2\text{GaTaO}_6$ suggest that films produced from these targets are all good candidates for use as buffer layers. In particular, $\text{Sr}_2\text{GaTaO}_6$ seemed to be a good material for synthesis via RF magnetron sputtering, as good quality films with smooth surfaces could be grown at temperatures lower than the other compounds, and in different sputtering geometries, allowing the process to be adapted to different situations. Additionally, this compound was shown to be suitable for use in multilayer heterostructures with superconducting thin films, as the film grew as an epitaxial single phase on YBCO, and the superconducting properties of the YBCO were preserved, although T_c was depressed to some degree. Further optimization of the deposition process could perhaps remedy this. Results with $\text{Sr}_2\text{AlTaO}_6$ seem to show that this material is less suitable for use in multilayer heterostructures synthesized by sputtering due to chemical reactions between the superconductor and the growing dielectric film. However, the material is still an attractive candidate as a

buffer layer substrate, as the bulk compound has a closer lattice match to YBCO than $\text{Sr}_2\text{GaTaO}_6$. More work is needed on the niobates to draw firm conclusions on their suitability; however, they are very attractive for future work due to their relatively low predicted dielectric constant. The compounds A_2MgWO_6 were determined to be unsuitable due to their low symmetry and tendency to deposit as binary oxides.

I would like to thank Laura L. H. King of Hewlett Packard, Inc. (formerly of Conductus, Inc.) for her assistance in obtaining x-ray phi scan, SEM, T_c , and AFM data on the films, and Roger Nielson for his assistance in obtaining EMPA data.

2.6 References

1. C. D. Brandle and V. J. Fratello, *J. Mater. Res.* **5**, 2160 (1990).
2. R. Guo, P. Ravindranathan, U. Selvaraj, A. S. Bhalla, L. E. Cross, and R. Roy, *J. Mater. Sci* **29**, 5054 (1994).
3. X. D. Wu, R. C. Dye, R. E. Muenchausen, S. R. Foltyn, M. Maley, A. D. Rollett, A. R. Garcia, and N. S. Nogar, *Appl. Phys. Lett.* **58**, 2165 (1991).
4. E. Olsson, G. Brorsson, P. Å. Nilsson, and T. Claeson, *Appl. Phys. Lett.* **63**, 1567 (1993).
5. B. Han, D. Neumayer, D. L. Schulz, T. J. Marks, H. Zhang, and V. P. Dravid, *Appl. Phys. Lett.* **61**, 3047 (1992).
6. A. T. Findikoglu, C. Doughty, S. Bhattacharya, Q. Li, X. X. Xi, T. Venkatesan, R. E. Fahey, A. J. Strauss, and J. M. Phillips, *Appl. Phys. Lett.* **61**, 1718 (1992).
7. B. Han, D. A. Neumayer, B. H. Goodreau, T. J. Marks, H. Zhang, and V. P. Dravid, *Chem. Mater.* **6**, 18 (1994).
8. Klaus K. Schuegraf, ed., *Handbook of Thin-Film Deposition Processes and Techniques*, pp. 291-301, Noyes Publications, Park Ridge, New Jersey (1988).
9. P. Woodward, R-D. Hoffmann, and A. W. Sleight, *J. Mater. Res.* **9**, 2118 (1994).
10. J. L. Schlenker and B. K. Peterson, *J. Appl. Cryst.* **29**, 178 (1996).
11. D. L. Bish and J. E. Post, eds., *Reviews in Mineralogy, v20: Modern Powder Diffraction*, pp. 266-268, The Mineralogical Society of America, Washington, D.C. (1989).
12. *Profile User's Guide v1.1*, Sobacim, 1995.
13. A. C. Larson and R. B. Von Dreele, *LANSCE*, Los Alamos National Lab., 1994.
14. R. D. Shannon, *J. Appl. Phys.* **73**, 348 (1993).
15. L. L. H. King, private communication (9/95).

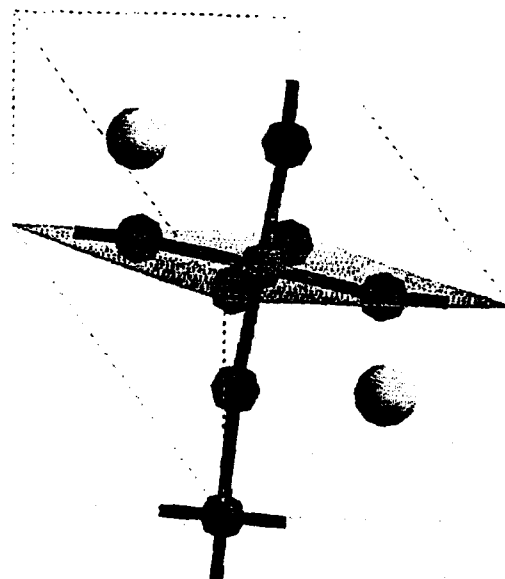
Chapter 3

Structural Studies of the Solid Solution $(\text{La}_{1-x}\text{Sr}_x)\text{AlO}_{3-y}$

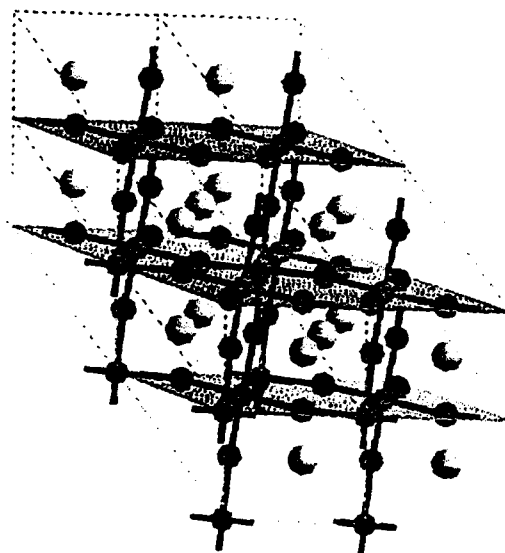
3.1 Introduction

Lanthanum aluminate, LaAlO_3 , is one of the most commonly used substrate materials in high temperature superconducting thin film microwave technology, and, in many ways, is the best of these. The lattice dimension of the film growth face (the rhombohedral (110), which is the pseudo-cubic (100)), is 3.79 Å. This is slightly smaller than the lattice constants of the superconductors YBCO ($a=3.84$ Å, $b=3.88$ Å) and TBCCO ($a=3.857$ Å), which results in only a small degree of compressive strain in the growing film. The dielectric constant of the material ($\epsilon_r=23-24$) (1,2), while higher than that of substrates for standard microwave circuits, is still low enough to allow for good signal speed, and the dielectric loss is extremely low ($\delta=3 \times 10^{-5}$ @ ~2.3 GHz) (2), allowing for good transmission of microwave power in resonators, filters, and other passive components. Films of superconductors grown on lanthanum aluminate typically outperform films grown on other substrates (1), with high critical currents, and good epitaxial growth demonstrated by sharp rocking curve profiles (3). The coefficient of thermal expansion ($1.1 \times 10^{-5} \text{ }^\circ\text{C}^{-1}$) is very close to that of YBCO ($1.26 \times 10^{-5} \text{ }^\circ\text{C}^{-1}$), and better than the other common substrates, which minimizes the possibility of film cracking as a result of thermal expansion differences when cooling from film growth temperature or to device operation temperature. The properties seem ideal until the problems associated with the rhombohedral symmetry and phase transition are considered.

LaAlO_3 crystallizes in the rhombohedral space group $R\bar{3}c$, and has unit cell constants of $a=5.356 \text{ \AA}$ and $\alpha=60.1^\circ$. If α were exactly 60.0° , the lattice would be metrically cubic. The unit cell is depicted in Figure 3.1, along with an extended view of the structure, to more clearly show its similarity to that of the ideal perovskite. The distortion in the structure is twofold, in that the corner sharing octahedra of the ideal perovskite structure are tilted relative to one another, and the octahedra themselves are flattened slightly along one threefold axis. Upon heating, the material undergoes a phase transition from the rhombohedral unit cell to the ideal cubic perovskite structure (space group $Pm\bar{3}m$). This phase transition was originally studied by high temperature x-ray diffraction, and was reported in 1956 by Geller and Bala to occur around $435 \text{ }^\circ\text{C}$ (4). A high temperature x-ray diffraction study by Coutures and Coutures in 1984 found the transition to occur at $500 \text{ }^\circ\text{C}$ (5). O'Bryan *et al* studied the phase transition by diffraction and heat capacity measurements in 1989, and found results consistent with the study by Coutures and Coutures (6). In this study, the peak splittings were visible to a temperature of near $500 \text{ }^\circ\text{C}$. The rhombohedral angle changed smoothly as a function of temperature, and was calculated to become cubic at $500 \text{ }^\circ\text{C}$ by extrapolation. Dilatometry detected no first order phase transition or abrupt volume change in this region. With the smooth change in lattice constants that accompanies the phase transition, little damage is induced in films grown on this substrate upon cooling after deposition. The formation of substrate twin planes does occur, however. Couple this with an anisotropy in the dielectric constant of around 10% for different crystallographic directions (7), and the problems with the material become more obvious. Because resonator



(a)



(b)

Figure 3.1 (a) The rhombohedral unit cell of LaAlO_3 , and (b) the extended structure, showing the similarity to the ideal perovskite structure (given in Figure 1.1). The (110) planes are shaded. These are the (100) planes in the cubic structure.

dimensions must be designed with an exact knowledge of the dielectric constant of the substrate, the formation of twins at random places in the substrate makes the design of such components with any reliability impossible.

By purely geometrical arguments, lanthanum aluminate is expected to be cubic, as demonstrated its tolerance factor of 1.016. Due to the otherwise ideal properties of the material, it would be desirable to change the symmetry of the compound, while preserving the desired properties. Groups in the past have investigated the effect of the substitution of different cations into the structure. These have been done as simple one-cation substitutions, as well as solid solutions between the lanthanum aluminate and cubic perovskites. The basic idea is to increase the average size of the A cation to stabilize the cubic 12 coordinate site. The first study done in this area was an attempt to determine the phase diagram of the $(\text{LaAlO}_3)_{1-x}/(\text{SrTiO}_3)_x$ solid solution by Bednoz and Muller (8). They found the system to be soluble across the whole composition range. A study of the rhombohedral-cubic phase transition revealed that the phase transition temperature decreased with increasing SrTiO_3 fraction, but did not reach room temperature through a fraction of 80% strontium titanate. Moreover, past this point, an uncertain region exists where the symmetry of the material could be $R\bar{3}c$, $Pm\bar{3}m$, or $I4/mcm$, which SrTiO_3 transforms to upon cooling to 105 K. This system was investigated as a potential substrate system by Vanderah *et al*, along with lanthanum aluminate solid solutions of SrZrO_3 , SrMgOF_2 , and SrScO_2F (9). Only the La/Al/Sr/Ti and La/Al/Sr/Mg/F oxide systems formed pure products. Peak splitting decreased to undetectable levels with the addition of 25% SrTiO_3 , but the

peaks were greatly broadened. No quantitative analysis or x-ray refinements were performed.

Another solid solution that has been investigated is that of lanthanum aluminate and the cubic double perovskites $\text{Sr}_2\text{AlTaO}_6$ and $\text{Sr}_2\text{AlNbO}_6$ (10). The entire solubility range was not investigated; only the compounds $0.7[\text{SrAl}_{0.5}\text{Ta}_{0.5}\text{O}_3]-0.3[\text{LaAlO}_3]$ and $0.7[\text{SrAl}_{0.5}\text{Nb}_{0.5}\text{O}_3]-0.3[\text{LaAlO}_3]$ were synthesized, along with the neodymium gallate analogues. The choice of the SAT and SAN perovskites as end members in lanthanum aluminate solid solutions is sensible, as the dielectric constants of these compounds are superior to those of LaAlO_3 ($\epsilon_r=11.8$ for ceramic SAT, and 18.7 for SAN), and the loss tangents are comparable. X-ray powder diffraction showed a single phase product with an ordered cubic structure. Dielectric measurements showed the products to have dielectric properties similar to the lanthanum aluminate. The growth of small crystal fibers was successful by a laser heated pedestal technique, and other groups have reported growth of single crystals in this system by the Czochralski technique (11).

Interest in LaAlO_3 as an oxygen ion conductor fueled studies on the substitution of various divalent cations into the structure to create oxygen ion vacancies (for example, see ref. 12). One study of these materials investigated which site the substitutional cations assumed in the structure by an investigation of unit cell parameter changes as a function of doping level (13). With the Sr doped sample, a slight, but smooth, increase in the lattice parameter was found with increasing Sr concentration. In the study, however, the lattice angle was treated as constant. With the ionic radius of 12-coordinate Sr^{2+} (1.44 Å) being

larger than that of La^{3+} (1.36 Å), it is likely that the lattice angle will change along with the unit cell length upon substitution of Sr for La.

The most recent appearance of Sr doped LaAlO_3 in the literature reported the synthesis of this compound as an impurity growing on the surface of polycrystalline pellets of materials in the SrLaAlO_4 - BaLaAlO_4 system (14). X-ray diffraction and EMPA studies indicated that as little as 1.5% to 3% strontium, along with less than 0.3% barium, doped into lanthanum aluminate was sufficient to change the symmetry to cubic. The structural work was not detailed, however, in that no refinements were reported, and no systematic investigation of the substitution was performed.

The original intention of the work presented here was to attempt to grow thin films of the 3% Sr cubic lanthanum aluminate. Upon making a target of the material, however, it was discovered that the compound doped to this level was not cubic, and that past reports of the system in the literature were quite incomplete, especially in the area of structural information. Thus, a range of compounds in the solid solution $(\text{La}_{1-x}\text{Sr}_x)\text{AlO}_{3-y}$ were synthesized and studied through powder x-ray diffraction. The unit cells of all synthesized compounds were refined using the GSAS (General Structural Analysis Software) Rietveld refinement software package (15). The structure of a high Sr concentration compound was investigated with neutron diffraction to study its symmetry and oxygen content and positions. Finally, high Sr concentration samples were annealed in different gas environments in attempts to reduce and oxidize the compound.

3.2 Experimental

Referring to the general formula $(\text{La}_{1-x}\text{Sr}_x)\text{AlO}_{3-y}$, compounds with $x=0, 0.01, 0.03, 0.05, 0.07, 0.09, 0.11, 0.13, 0.15,$ and 0.17 were synthesized via standard solid state techniques. Stoichiometric amounts of powders of La_2O_3 (Aldrich, 99.99%), SrCO_3 (Mallinckrodt, 99.9%), and Al_2O_3 (Aldrich, 99.8%) were ground together with an agate mortar and pestle. The mixtures were transferred to alumina crucibles and heated to $1300\text{ }^\circ\text{C}$ for 10 hours in air. After this treatment, the powders were reground and heated to $1400\text{ }^\circ\text{C}$ for 10 hours. Powder x-ray diffraction patterns were taken between each heating cycle. After going to $1400\text{ }^\circ\text{C}$, x-ray diffraction revealed impurity phases, so the mixtures were heated to $1450\text{ }^\circ\text{C}$ for 10 hours. Diffraction patterns revealed impurity peaks of the same intensity as before still present, so the powders were next taken to $1500\text{ }^\circ\text{C}$ for 10 hours. The intensities of the impurities decreased after this step, so one final heating to $1500\text{ }^\circ\text{C}$ was performed. Powder x-ray diffraction analysis was performed on a Siemens D-5000 diffractometer. X-ray patterns were refined using the GSAS program. Williamson-Hall analysis was used to determine the strain in the crystallites through the series.

A sample with $x=0.35$ was prepared to test the solubility of strontium in the lanthanum aluminate. The sample was prepared the same as those from $x=0$ to $x=0.17$ until the final heating cycle was reached. The $x=0.35$ sample still had fairly intense impurity peaks in the x-ray diffraction pattern after heating to $1500\text{ }^\circ\text{C}$, so it was taken first to $1525\text{ }^\circ\text{C}$, and then to $1550\text{ }^\circ\text{C}$. At this temperature, the powder started to react with the alumina crucible, so higher temperatures were not attempted. Heating at $1550\text{ }^\circ\text{C}$ was repeated until the impurity peaks

ceased changing in relative intensity between high temperature treatments. This took only 2 cycles. The structure, along with the impurity fraction, was refined using GSAS.

Once this study determined the solubility of strontium in the lanthanum aluminate, a sample of $x=0.25$ was prepared for neutron diffraction. For this sample, high purity reagents were used in the preparation. These were La_2O_3 (Aldrich, 99.99%), SrCO_3 (Aldrich, 99.995%), and Al_2O_3 (Aldrich, 99.99%). Otherwise, the preparation was the same as for the $x=0.35$ sample, with two 10 hour heatings done at 1550 °C. The sample was sent to Brookhaven National Laboratories to obtain neutron diffraction data.

Samples of $x=0.15$ were prepared for the redox studies. Initially, the samples were prepared using the standard lower purity reagents. The following anneals resulted in the respective color to appear in the samples: 1500 °C for 10 hours in air resulted in a light tan color, 1500 °C for 10 hours in a vacuum resulted in a very light pink, 1500 °C for 10 hours in a 10% H_2 /90% N_2 resulted in a gray color, and 1500 °C for 32 hours in O_2 resulted in a light mustard/brown color. The hydrogen and oxygen annealed samples were prepared in a Thermolyne high temperature tube furnace, and the vacuum annealed sample was prepared in a brew furnace. To test whether these colors were due to the strontium substitution in the lanthanum aluminate itself, or merely impurities present in the structure from the lower purity starting materials, the samples were again prepared using the higher purity reagents. With the higher purity reagents, the air annealed sample was much closer to white than the lower purity sample. The other color

changes were different as well, and are discussed below with the rest of the experimental results.

3.3 Results

X-ray diffraction patterns showing the decrease in splitting between the $(42\bar{2})$ and (642) peaks as the strontium content decreases is given in Figure 3.2. The splitting appears to decrease in a smooth manner, indicating the continuous solubility of strontium in the lanthanum aluminate lattice. The peak shifts along the two-theta axis cannot be interpreted from this figure alone, as some small zero point error exists in each scan. As the peak splitting decreases, the peaks broaden, possibly indicating strain due to defects introduced into the structure. This decrease in splitting is the effect expected if the structure were to move toward cubic, as the two peaks should merge to form the (321) peak in the space group $Pm\bar{3}m$. This is the same effect reported in reference 9. To quantify this trend, each structure was refined.

The refined crystallographic variables for the compound in the space group $R\bar{3}c$ were the unit cell constants (a and α), the fractional occupancy of strontium on the lanthanum site, the oxygen positional parameter x (y and z are not variables in this space group), and the isotropic thermal parameters for each atomic position. Additionally, where a significant amount of a second phase appeared in the x-ray pattern, the phase fraction was refined. The sum of the lanthanum and strontium was constrained to be 1, as was the sum of the phase fractions. The refined lattice parameters are given in Table 3.1. The $x=.25$ and $.35$ compounds were refined in the space group $Pm\bar{3}m$ as well as $R\bar{3}c$, but the rhombohedral results are presented in this section for consistency. The cubic results are summarized in a later section. From

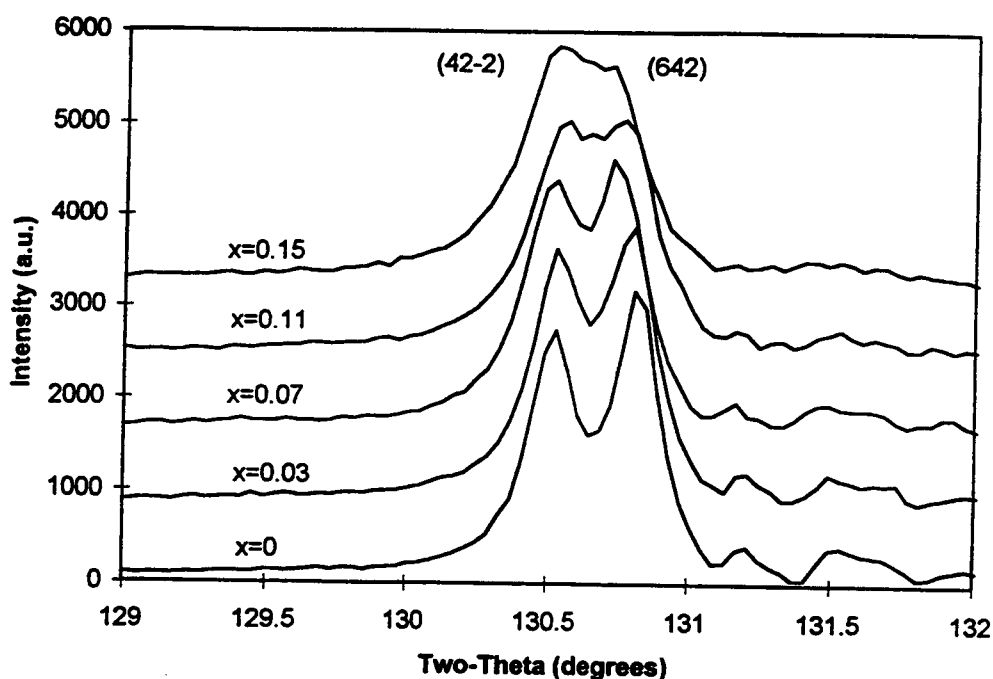


Figure 3.2 Two-theta x-ray diffraction scans of the $(42\bar{2})$ and (642) peaks for various compositions of $(\text{La}_{1-x}\text{Sr}_x)\text{AlO}_{3-y}$, demonstrating the decrease in peak splitting as strontium concentration increases.

the table, some trends are immediately evident. The most obvious is the decrease in the lattice angle through the series. With no strontium, the lattice angle refined to a value of 60.101 degrees, which is the accepted value. With as little as 1% strontium in the compound, the angle decreases to 60.092 degrees. The trend continues through the end of this series, and is as low as 60.058 by the time the 17% strontium sample is reached. (Keep in mind that the percent strontium is the mole percentage used as a reactant, and should not be thought of as the actual amount of strontium in the lanthanum aluminate lattice. Refined

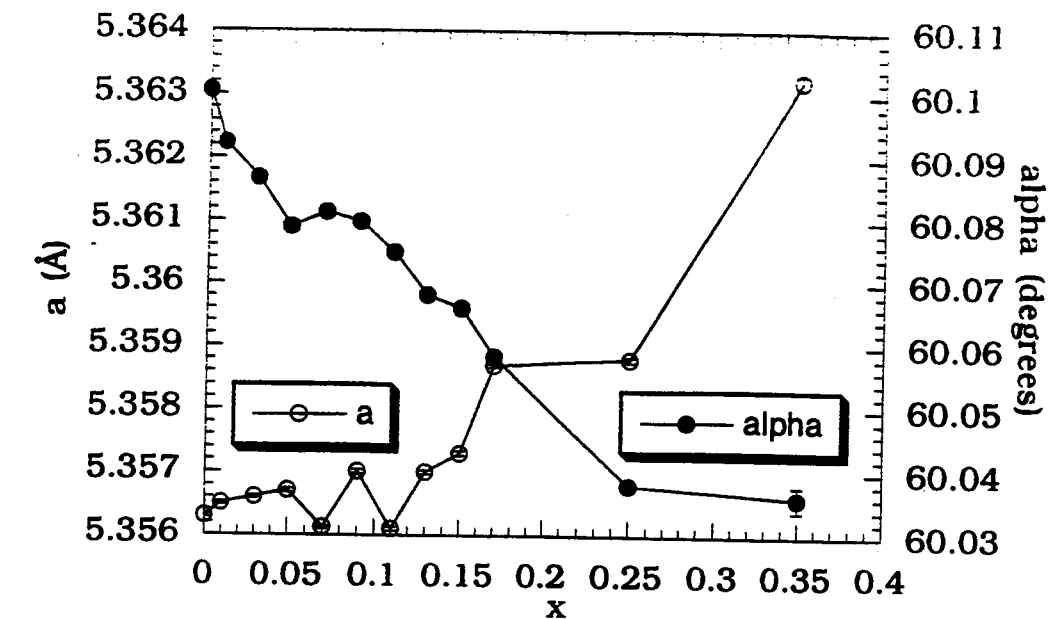
Table 3.1

Refined Lattice Parameters for $(\text{La}_{1-x}\text{Sr}_x)\text{AlO}_{3-y}$
Standard Deviations in Parentheses

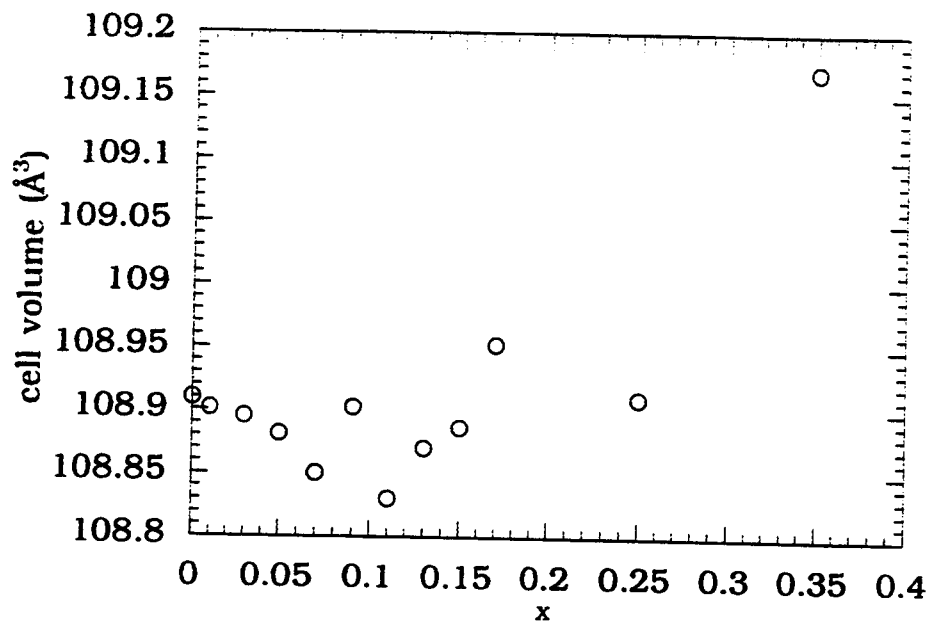
x	a and (σ_a), (Å)	α (degrees) ¹	Cell Volume and (σ), (Å ³)
0.00	5.3563 (0.00002)	60.101 (0.000)	108.909 (0.001)
0.01	5.3565 (0.00002)	60.092 (0.000)	108.901 (0.001)
0.03	5.3566 (0.00002)	60.087 (0.000)	108.895 (0.001)
0.05	5.3567 (0.00003)	60.079 (0.000)	108.881 (0.001)
0.07	5.3561 (0.00002)	60.081 (0.000)	108.850 (0.001)
0.09	5.3570 (0.00003)	60.080 (0.000)	108.902 (0.001)
0.11	5.3561 (0.00003)	60.075 (0.000)	108.830 (0.001)
0.13	5.3570 (0.00003)	60.068 (0.000)	108.870 (0.001)
0.15	5.3573 (0.00004)	60.066 (0.000)	108.886 (0.001)
0.17	5.3587 (0.00003)	60.058 (0.000)	108.952 (0.001)
0.25	5.3588 (0.00004)	60.038 (0.001)	108.910 (0.001)
0.35	5.3632 (0.0001)	60.036 (0.002)	109.170 (0.002)

occupancies are presented later in this section.) The standard deviations for the lattice angle values given in the GSAS output file were all zero. Lattice parameter refinements were also done by mixing in a silicon standard with the powders, indexing and fitting the peaks manually, and using the program REFCEL to refine the variables. The results were consistent with the GSAS results, and the error was given to be in the third decimal place. These values are plotted in Figure 3.3, along with those of the lattice constant and cell volume.

From Table 3.1, it is also evident that the lattice constant increases slightly with increasing strontium content, as was reported in reference 13. This is a much smaller effect than the lattice angle change, and is not as consistent across the series. The reported ionic radius of the 12 coordinate lanthanum (1.36 Å) ion is only 0.08 Å smaller than that of the strontium ion in the same coordination (1.44 Å), so a large change is not to be expected with the substitution.



(a)



(b)

Figure 3.3 (a) Plot of the lattice constant and lattice angle vs. strontium concentration in reaction mixture. Note the trend toward an angle of 60° with increasing strontium concentration. At 60° , the structure would become metrically cubic. (b) Plot of cell volume vs. strontium concentration.

The effect of the lattice parameter changes on the cell volume is less clear. The volume initially appears to be decreasing very slightly through the series, but as higher concentrations of strontium are reached, the volume begins an increasing trend. The apparent volume increase in the $x=.35$ sample relative to that of the unsubstituted compound is quite large.

In Table 3.2, the refined fractional occupancy of strontium is given, along with the statistics describing the closeness of fit of each refinement. The strontium occupancy appears to be quite variable over the range of x , but there is a visible trend in the data, showing the refined strontium concentration to generally increase along the series. This is more evident in a plot of the data, given in Figure 3.4. The oxygen position changes very little across the series, but the magnitude of the changes between adjacent members of the series are greater than one standard deviation for most cases. Toward the end of the series, the oxygen position changes more dramatically, moving more toward the ideal position of $x=-0.25$. A plot of this is also given in Figure 3.4.

Before discussing the statistics given in Table 3.2, a mention of how a Rietveld refinement is performed, and what the statistics say about the refinement, is necessary. The purpose of the refinement is to generate a calculated x-ray diffraction pattern based on a model structure. The variables that define the peak widths and intensities of an x-ray powder diffraction pattern are changed in the model, and the calculated pattern is generated, in a recursive fashion, to minimize the functions

$$Rp = \sum_i |Y_{io} - Y_{ic}| / \sum_i Y_{io} \quad (3.1)$$

Table 3.2

Fractional and Positional Variables, and Refinement Statistics,
for $(\text{La}_{1-x}\text{Sr}_x)\text{AlO}_{3-y}$

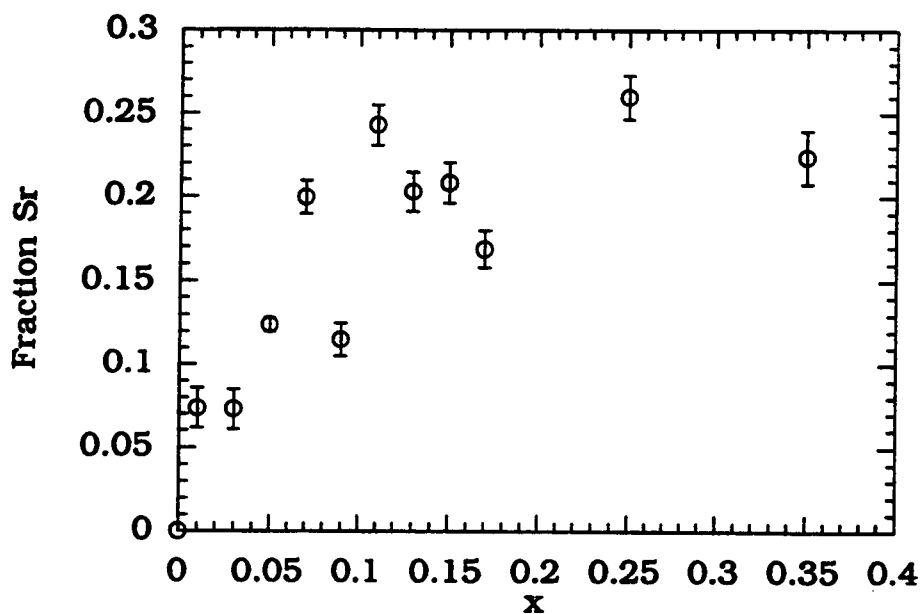
x	Refined Sr Fraction on La site, (σ)	Oxygen Position ¹ , (σ)	R _p	wR _p	χ^2
0	0	-0.219 (.0007)	0.0797	0.1256	9.0380
0.01	0.0737 (.001)	-0.224 (.0007)	0.0713	0.1182	8.457
0.03	0.0730 (.001)	-0.222 (.0008)	0.0733	0.1135	7.835
0.05	0.124 (.0004)	-0.223 (.0008)	0.0769	0.1212	9.323
0.07	0.200 (.001)	-0.222 (.0007)	0.0725	0.1107	7.491
0.09	0.115 (.001)	-0.222 (.0008)	0.0691	0.1069	7.398
0.11	0.243 (.001)	-0.227 (.001)	0.0832	0.1217	9.509
0.13	0.202 (.001)	-0.227 (.001)	0.0841	0.1289	10.050
0.15	0.208 (.001)	-0.229 (.001)	0.0794	0.1295	10.600
0.17	0.169 (.001)	-0.232 (.001)	0.0751	0.1228	9.657
0.25	0.257 (.01)	-0.232 (.0008)	0.0817	0.1114	12.9
0.35	0.224 (.02)	-0.239 (.003)	0.0881	0.1265	8.910

¹The only positional parameter in this space group is x, which applies only to the oxygen. To avoid confusion with the general formula variable x specifying the strontium content of the reactants, the oxygen positional parameter will not be referred to as x.

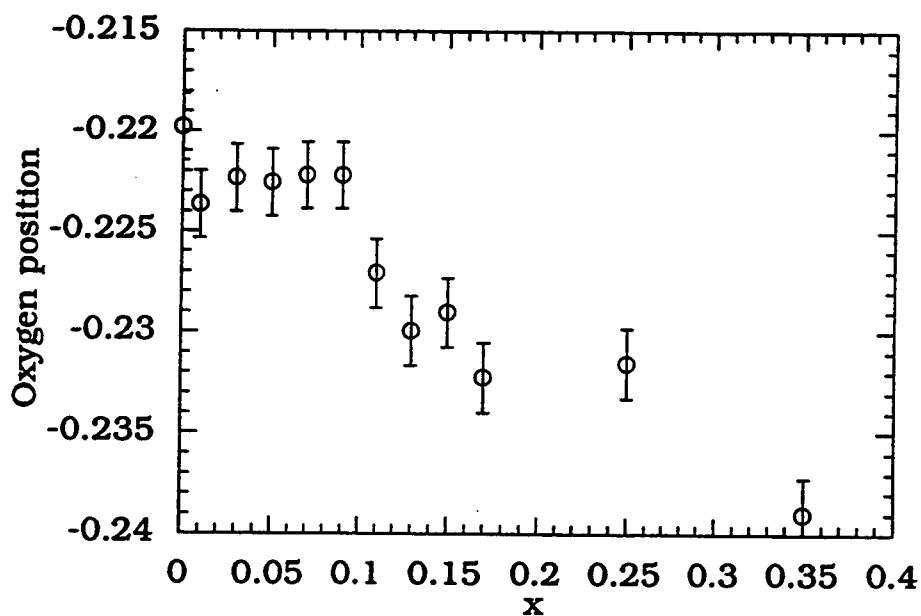
and

$$wR_p = \left[\sum_i w_i (Y_{io} - Y_{ic})^2 / \sum_i w_i Y_{io}^2 \right]^{1/2}. \quad (3.2)$$

In these functions, the variable Y_{io} is the observed intensity of the diffraction pattern at step i, Y_{ic} is the calculated intensity at this step, and w_i is a weight assigned the intensity at each step, generally equal to the square root of the observed intensity (or, equivalently, the inverse of the counting error) (15). The statistical quantity χ^2 describes how well the model pattern compares to the best possible fit, taking into consideration such limiting factors as the signal to noise ratio of the experimental pattern. The mathematical form of this is



(a)



(b)

Figure 3.4 (a) Refined Sr occupancy vs. x , and (b) Oxygen position vs. x in $(La_{1-x}Sr_x)AlO_{3-y}$.

$$\chi^2 = (wR_p / R_{\text{exp}})^2 = \sum_i w_i (Y_{io} - Y_{ic})^2 / (N - P) \quad (3.3)$$

where R_{exp} is the expected (or the statistically best possible) R, N is the number of observations, and P is the number of parameters. The value of χ^2 is not expected to be less than one.

Refinement statistics given in Table 3.2 are consistent from sample to sample, with a typical R_p of 0.07 to 0.08, and a wR_p of 0.11 to 0.12. χ^2 was usually between 7 and 10, with only a couple of refinements having a value of just over 10. The greatest source of pattern mismatch, as displayed by higher numerical statistical values, is peak fitting error. Profiles of some of the lower angle peaks proved difficult for the software to fit, but plots showing the difference values between the calculated and observed x-ray patterns showed the error to be symmetrical about the zero point, signifying that the error was not in the structural variables. A χ^2 of around 7 was obtained when the major visible error present was in the peak shapes. Higher values of χ^2 generally signify the presence of a small minority phase. Where the minority phase fraction appeared to be significant, the phase was identified and refined along with the primary phase.

The isotropic thermal parameters for each atomic position, and, where applicable, the impurity phase fraction, are given in Table 3.3. The thermal parameters refined as expected. As the strontium concentration in the compound grows greater, the thermal parameters become larger. This signifies more disorder in the sample, as the atomic positions appear more smeared out. Additionally, the creation of oxygen vacancies by the inclusion of the divalent strontium cation could open up the structure, allowing for greater thermal motion.

Table 3.3

Isotropic Thermal Parameters and Impurity Phase/Phase Fraction
for $(\text{La}_{1-x}\text{Sr}_x)\text{AlO}_{3-y}$

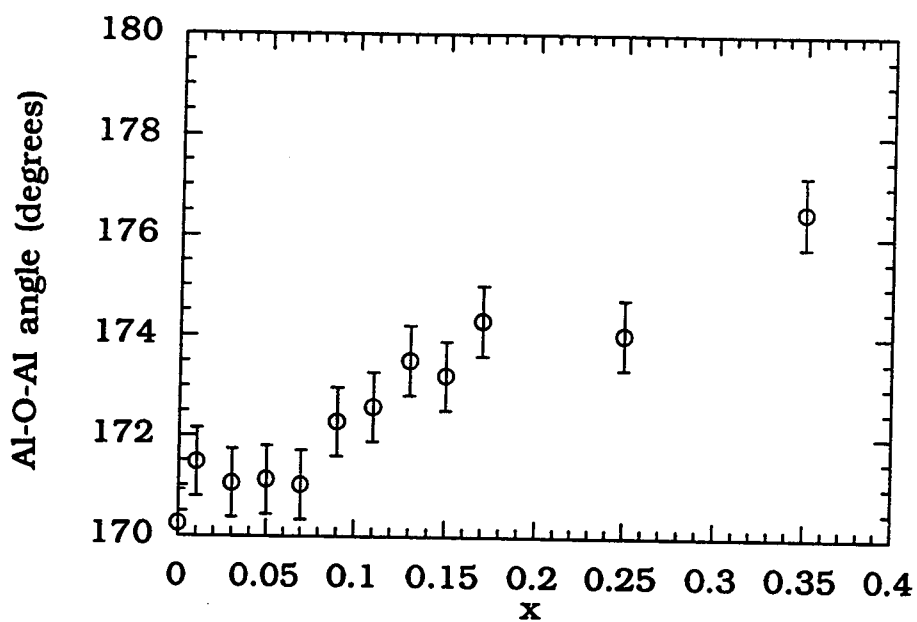
x	UIISO (La/Sr) (\AA^3)	UIISO (Al) (\AA^3)	UIISO (O) (\AA^3)	Impurity Phase / %
0	0.00268	0.00305	0.00129	La_2O_3 / (unrefined)
0.01	0.00376	0.00501	0.00614	---
0.03	0.00425	0.00643	0.00607	SrAl_2O_4 / 0.44
0.05	0.00339	0.00535	0.00576	SrAl_2O_4 / 1.07
0.07	0.00296	0.00654	0.00692	SrAl_2O_4 / 0.76
0.09	0.00520	0.00676	0.00889	SrAl_2O_4 / 0.69
0.11	0.00254	0.00683	0.00853	---
0.13	0.00316	0.00623	0.00913	SrAl_2O_4 / 0.18
0.15	0.00362	0.00673	0.00933	SrAl_2O_4 / 0.92
0.17	0.00559	0.00748	0.0115	SrAl_2O_4 / 2.30
0.25	0.00610	0.00353	0.00500	SrAl_2O_4 / 4.89
0.35	0.00478	0.00451	0.01148	SrAl_2O_4 / 4.20

The primary impurity phase in almost all the samples was the monoclinic SrAl_2O_4 . To improve the fitting statistics of the calculated patterns, the phase was refined along with the $(\text{La}_{1-x}\text{Sr}_x)\text{AlO}_{3-y}$, and a phase fraction was obtained. Another impurity noticed in several samples was SrAlLaO_4 , with the K_2NiF_4 structure. However, it was generally present in such small quantities that inclusion in the refinements did not change the resulting fit significantly. It was found to be quite difficult to avoid the formation of the SrAl_2O_4 impurity. Heating to 1550 °C did result in a decrease in the intensities of the x-ray peaks from this phase, but never in the complete removal of the phase. At this temperature, the powders reacted with the alumina crucible, so no higher temperatures were tried. The concentration of this impurity, however, does not seem to scale with the amount of strontium in the reaction mixture.

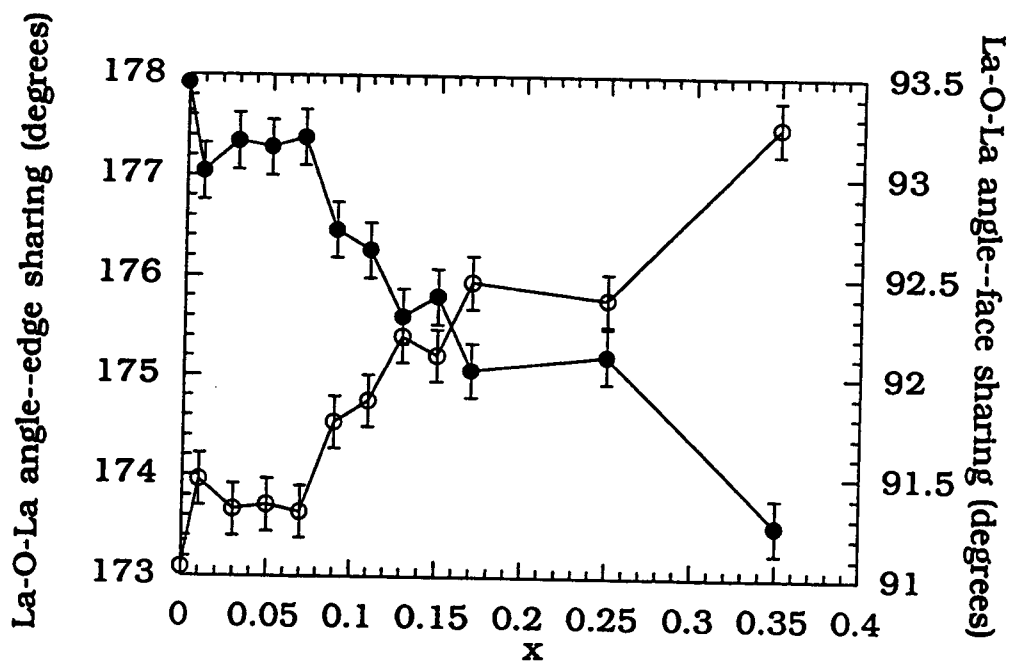
Table 3.4Bond Angles as a Function of x in $(\text{La}_{1-x}\text{Sr}_x)\text{AlO}_{3-y}$

x	Al-O-Al Angle (degrees)	La-O-La Angle 1	La-O-La Angle 2	O-Al-O Angle
0.00	170.24 (0.24)	173.09 (0.17)	93.46 (0.08)	90.29 (0.01)
0.01	171.47 (0.24)	173.96 (0.17)	93.02 (0.08)	90.238 (0.009)
0.03	171.05 (0.00)	173.66 (0.00)	93.17 (0.00)	90.25 (0.01)
0.05	171.12 (0.26)	173.71 (0.18)	93.14 (0.09)	90.24 (0.01)
0.07	171.02 (0.22)	173.64 (0.06)	93.19 (0.08)	90.257 (0.009)
0.09	172.28 (0.25)	174.53 (0.18)	92.73 (0.09)	90.199 (0.008)
0.11	172.58 (0.34)	174.75 (0.24)	92.63 (0.12)	90.18 (0.01)
0.13	173.50 (0.31)	175.40 (0.22)	92.30 (0.30)	90.151 (0.009)
0.15	173.20 (0.40)	175.21 (0.25)	92.40 (0.13)	90.17 (0.01)
0.17	174.30 (0.40)	175.94 (0.25)	92.03 (0.13)	90.135 (0.009)
0.25	174.03 (0.25)	175.77 (0.18)	92.11 (0.09)	90.124 (0.009)
0.35	176.5 (1.0)	177.5 (0.7)	91.26 (0.34)	90.04 (0.015)

With the structure refinements complete, it was possible to examine the transformation through the calculation of the bond distances and angles in the structure. Table 3.4 lists the interesting bond angles in this transformation. The Al-O-Al bond angle is 180 degrees for the ideal cubic perovskite. For the $(\text{La}_{1-x}\text{Sr}_x)\text{AlO}_{3-y}$, the angles change from near 170 degrees to almost 177.5 degrees, and the individual shifts from structure to structure are of greater magnitude than statistical errors. This suggests that the tilting of the octahedra relative to one another is decreasing with increasing strontium substitution. In the ideal cubic structure, one La-O-La bond angle should be 180 degrees (from one unit cell to the next edge-sharing cell), and one should be 90 degrees (for the La-O-La bond angle created by face sharing unit cells). The large deviations from the ideal cubic values present in lanthanum aluminate are lessened with the addition of



(a)



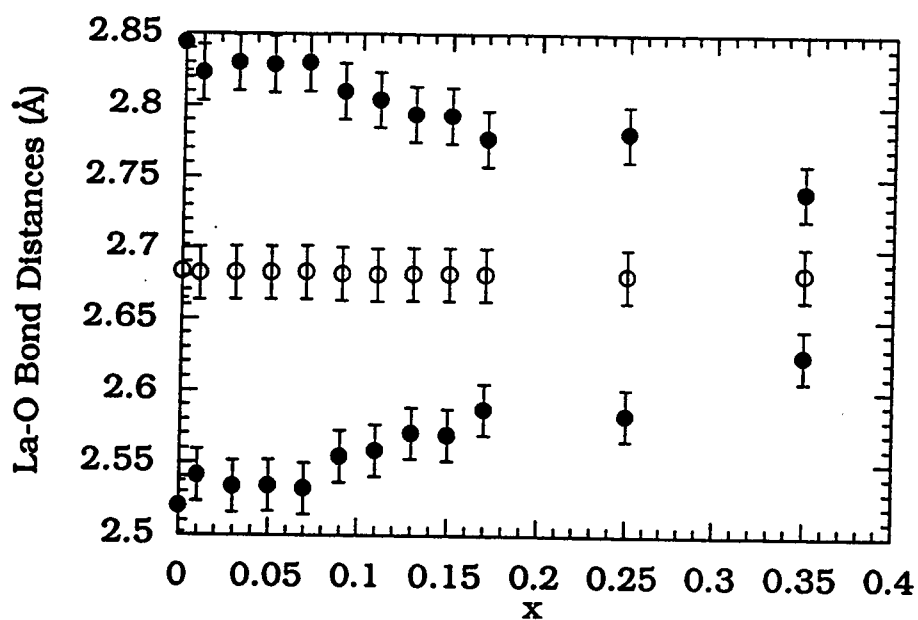
(b)

Figure 3.5 (a) Al-O-Al bond angle and (b) O-Al-O bond angles as a function of x in $(\text{La}_{1-x}\text{Sr}_x)\text{AlO}_{3-y}$.

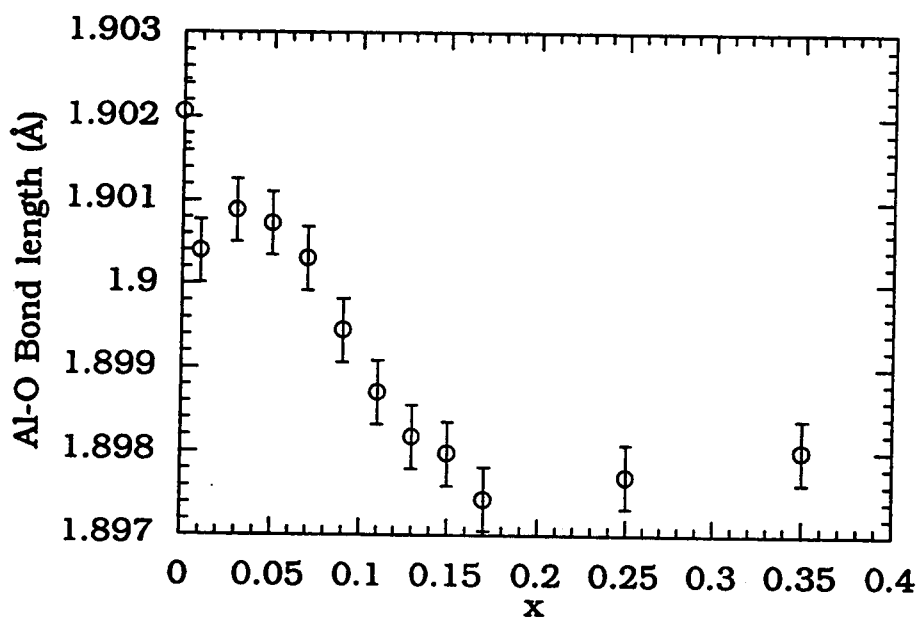
Table 3.5Bond Distances as a Function of x in $(\text{La}_{1-x}\text{Sr}_x)\text{AlO}_{3-y}$

x	Al-O Distance (Å)	La-O Distance 1 (Å)	La-O Distance 2 (Å)	La-O Distance 3 (Å)
0.00	1.9021 (.0003)	2.6830 (.0002)	2.8440 (.004)	2.5200 (.004)
0.01	1.9004 (.0003)	2.6820 (.0002)	2.8230 (.004)	2.5410 (.004)
0.03	1.9009 (.0000)	2.6824 (.0000)	2.8301 (.000)	2.5335 (.000)
0.05	1.9007 (.0003)	2.6824 (.0002)	2.8290 (.004)	2.5340 (.004)
0.07	1.9003 (.0003)	2.6825 (.0002)	2.8300 (.004)	2.5320 (.004)
0.09	1.8994 (.0003)	2.6816 (.0002)	2.8100 (.004)	2.5540 (.004)
0.11	1.8987 (.0004)	2.6809 (.0003)	2.8040 (.006)	2.5580 (.006)
0.13	1.8982 (.0003)	2.6815 (.0002)	2.7940 (.005)	2.5700 (.005)
0.15	1.8980 (.0004)	2.6813 (.0003)	2.7930 (.006)	2.5690 (.006)
0.17	1.8974 (.0002)	2.6813 (.0002)	2.7770 (.006)	2.5870 (.006)
0.25	1.8958 (.0002)	2.6782 (.0002)	2.7780 (.0003)	2.5801 (.0003)
0.35	1.8980 (.0005)	2.6826 (.003)	2.740 (.007)	2.625 (.007)

strontium; the La-O-La angle formed by edge sharing unit cells changes from 173 to 177.5 degrees, and the one formed by face sharing cells transforms from about 93.5 to 91.2 degrees. The O-Al-O angles within the aluminum octahedra move toward the ideal value of 90°, showing a decrease in the distortion within the octahedra themselves. In all calculations, a major deviation from the trend existed in the x=.25 sample. The refinement was repeated, and the same results were found. It is interesting in that the lattice parameters of this compound are close to those of the x=.35 sample, while the bond angles are far different.



(a)



(b)

Figure 3.6 A plot of the (a) La-O and (b) the Al-O bond distances as a function of x in $(\text{La}_{1-x}\text{Sr}_x)\text{AlO}_{3-y}$.

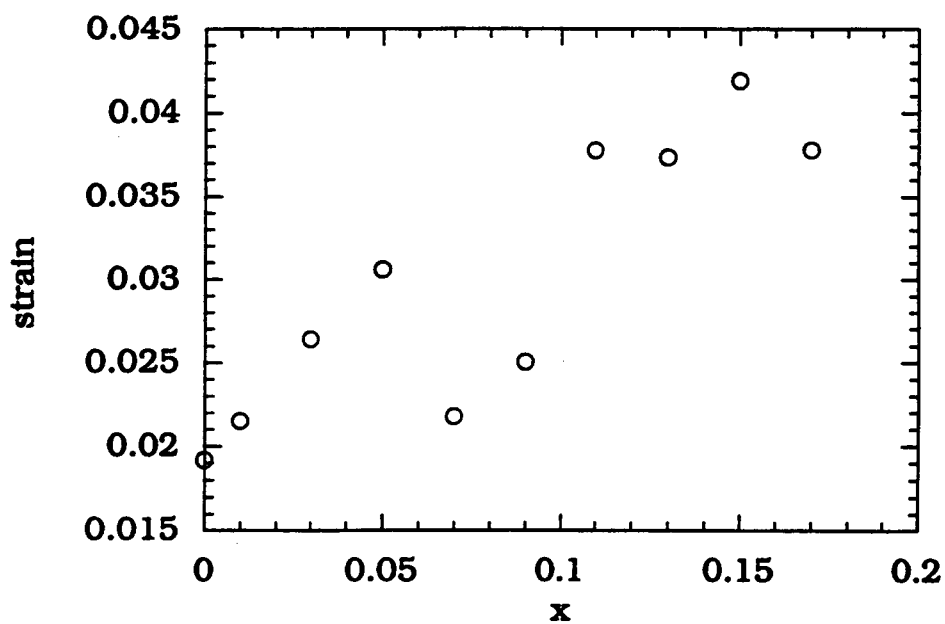
This suggests the cell is metrically cubic, but the oxygen atoms are still off the cubic special positions. Plots of the Al-O bond angle changes are shown in Figure 3.5.

Bond distance data is given in Table 3.5. It is well known (17) a decrease in an octahedral distortion is often accompanied by a decrease in M-O bond distances within the octahedra. This appears to be true for the Al-O octahedra in this structure, as the substitution of the larger, lower valence strontium ion results in an increase in the strength of the Al-O bonding interaction, decreasing the bond distance. The La-O bond distances give further evidence of the decrease in structural distortions. In the rhombohedral structure, the 12 coordinate ion (La and Sr) of a perovskite is not actually coordinated by 12 equidistant anions. The coordination polyhedra distorts somewhat along the pseudocubic unit cell diagonal, resulting in 3 nearest anions, 6 at a slightly longer distance, and 3 farthest. In Table 3.5, the column labeled *La-O Distance 1* is the intermediate bond distance, *La-O Distance 2* is the longest, and *La-O Distance 3* is the shortest. As the strontium content increases, the longer and shorter distances approach the intermediate value. Also, as the La-O-La and Al-O-Al bond angles approach the cubic values, the Al-O distance and La-O distance 1 both decrease slightly as expected. This is readily seen in Figure 3.6, which gives a plot of these distances as a function of the strontium content.

From the x-ray patterns (Figure 3.2), it is evident that, as the strontium concentration increases and the peak splitting decreases, the peaks become broader. This is indicative of increasing lattice strain. Peaks that have no overlap were fit with the program Profile, and were

Table 3.6**Strain Analysis of $(La_{1-x}Sr_x)AlO_{3-y}$**

x	Strain	Residuals of Williamson-Hall Plot
0.00	0.0192	0.997
0.01	0.0215	0.991
0.03	0.0264	0.991
0.05	0.0306	0.991
0.07	0.0218	0.984
0.09	0.0250	0.970
0.11	0.0378	0.980
0.13	0.0373	0.975
0.15	0.0419	0.983
0.17	0.0378	0.980

**Figure 3.7** Strain in $(La_{1-x}Sr_x)AlO_{3-y}$ crystallites as a function of x .

analyzed for strain using the Williamson-Hall analysis described in Chapter 2. A summary of the strain data is presented in Table 3.6, and a figure depicting the increase in strain with increasing Sr concentration is shown in Figure 3.7. The residuals of the best fit lines for each Williamson-Hall plot are given along with the strain magnitude as a figure of merit.

If the plots of the bond angles are fitted to a best fit straight line, the extrapolated strontium content at which the compound goes cubic is found to be $x=0.46$. This seemed a very high concentration of a divalent ion to substitute onto a trivalent lattice site, so to investigate the higher strontium concentration regime of this solid solution, a composition of $x=0.35$ was attempted. After synthesis, the x-ray pattern from the product appeared to be that of a cubic perovskite. A segment of the x-ray diffraction pattern, compared to that of the pure LaAlO_3 and of the $x=0.11$ sample, is shown in Figure 3.8. Note the symmetry of the $x=0.35$ peaks compared to those of the other two phases. The primary impurity phase was once again SrAl_2O_4 , although, considering the extremely high concentration of strontium added to the sample, the amount of the phase present in the final product is surprisingly small. Visible inhomogeneities existed in the powder. Whereas the powders for $x=0.17$ consistently appeared light tan, the $x=0.35$ had both dark brown grains and lighter tan grains, both in fairly large proportions. The x-ray pattern shows the product to be mostly the desired phase, however. Furthermore, upon grinding the powder, the sample became homogeneously light tan, pointing to the possibility that the dark brown phase may form only in small quantities. The peaks become broad with increasing two-theta, indicating a good deal of lattice strain. To attempt

Table 3.7Results of $\text{La}_{.65}\text{Sr}_{.35}\text{AlO}_{3-y}$ X-Ray Refinement in $R\bar{3}c$ and $Pm\bar{3}m$

Variable	Pm3m	R-3c (Starting Rho)	R-3c (Starting Cubic)
a (Å)	3.7935	5.3632 ¹	unstable
α (degrees)	n/a (60)	60.036	unstable
Fraction La	0.811	0.776	unstable
Fraction Sr	0.189	0.224	unstable
Oxygen Position	n/a (-0.25)	-0.239	unstable
UIO (La,Sr)	0.00498	0.00478	
UIO (Al)	0.00340	0.00451	
UIO (O)	0.01137	0.01148	
G_u	15.7	unstable	
G_v	-8.2	unstable	
G_w	5.1	unstable	
L_x	2.049	3.117	
L_y	15.773	15.032	
Fraction LaAlO_3	.977	.958	
Fraction SrAl_2O_4	.023	.042	
Rp	0.0730	0.0881	0.0763
wRp	0.1196	0.1265	0.1283
χ^2	8.806	9.838	8.910

¹The pseudo-cubic lattice constant, for comparison with Pm3m results, is 3.7924 Å.

to determine the actual symmetry of this compound, and to get an idea of the fractional occupancy of strontium on the lanthanum site, the compound was refined both in the rhombohedral space group $R\bar{3}c$ and the cubic space group $Pm\bar{3}m$. The results of both refinements are given in Table 3.7. The rhombohedral refinement was attempted by first starting at the refined values of the x=0.17 sample, and then by first refining the structure in the cubic space group, and using the results from the cubic refinement as the starting point for the rhombohedral refinement. The cubic refinement converged rapidly, and the final fit

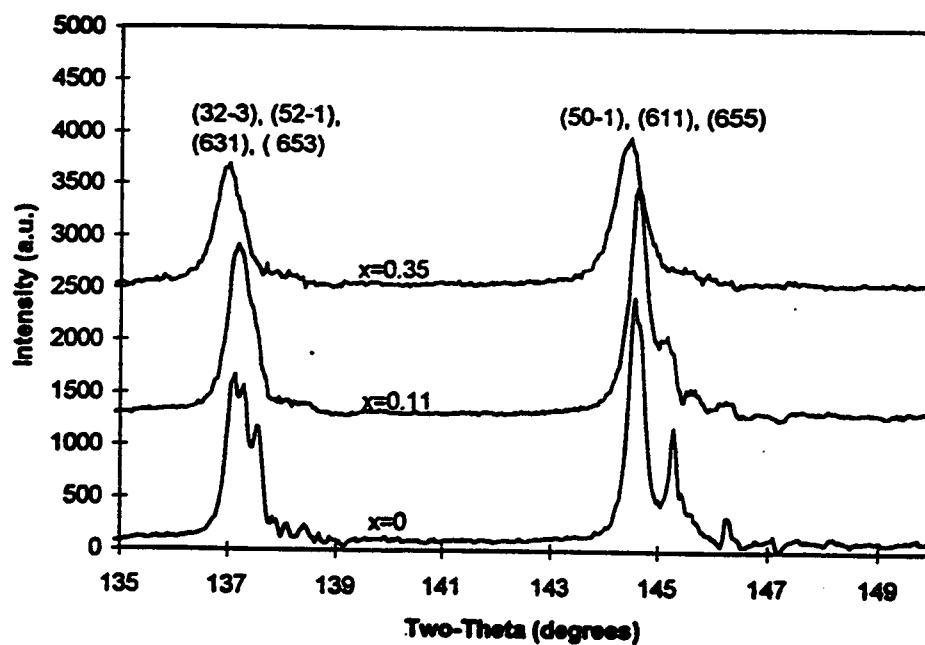
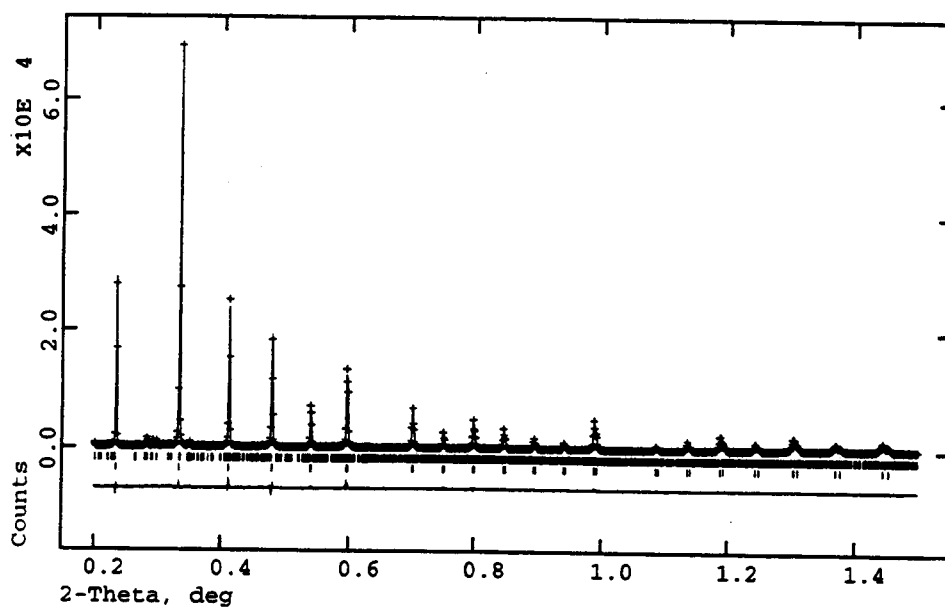
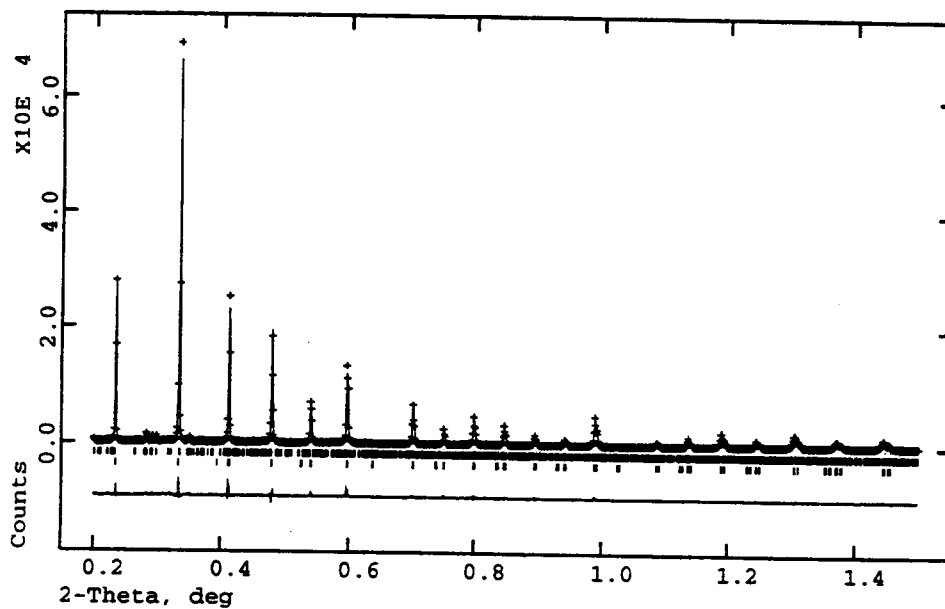


Figure 3.8 X-ray powder diffraction scans of high angle peaks of $(\text{La}_{1-x}\text{Sr}_x)\text{AlO}_{3-y}$ samples of $x=0$, 0.11, and 0.35, to demonstrate the seemingly cubic symmetry of the $x=0.35$ powder.



(a)



(b)

Figure 3.9 Comparisons of calculated and observed peak intensities from Rietveld refinements performed on $\text{La}_{0.65}\text{Sr}_{0.35}\text{AlO}_{3-y}$ performed in (a) $\text{Pm}3\text{m}$, and (b) $\text{R-}3\text{c}$ (starting from $x=0.17$ values), demonstrating the slight error in the calculated peak intensities for the rhombohedral case. The x-axis scale is degrees/100.

statistics were comparably low to the members of the series with lower strontium content refined in the known space group. When the refinement was attempted in the rhombohedral space group, starting from the $x=0.17$ refined values for all variables, the refinement was not stable to Gaussian peak profile refinement. More importantly, the refinement converged with poorer fit statistics than the cubic case. Additionally, the errors in the fit cannot be attributed to peak fitting errors, as they can in the cubic case. The two attempts fit the high angle peaks well, but the low angle peak intensities are not correct for the rhombohedral case, as shown in Figure 3.9. The rhombohedral refinement should be able to be at least as good as the cubic refinement, as there are more variables available for manipulation. The rhombohedral refinement was found to oscillate, rather than converge, as a result of highly correlated variables. The values from the cubic refinement were used as a starting point for the refinement of the compound in the rhombohedral space group to test for convergence on a minima with values closer to those of the cubic. From this point, it was impossible to refine any variables except for scale factors without the refinement diverging.

The strontium occupancy on the A cation site refined to fairly similar values in each space group (approximately 20%), so a sample of a close composition to this was synthesized for x-ray and neutron diffraction analysis. The A cation reactant ratio was chosen to be 25% strontium to account for the usual formation of impurity phases in the final product. The x-ray diffraction pattern was refined first, again in both $R\bar{3}c$ and $Pm\bar{3}m$. The results of both refinements are given in Table 3.8. As in the case of the $x=0.35$ sample, refinements in both space

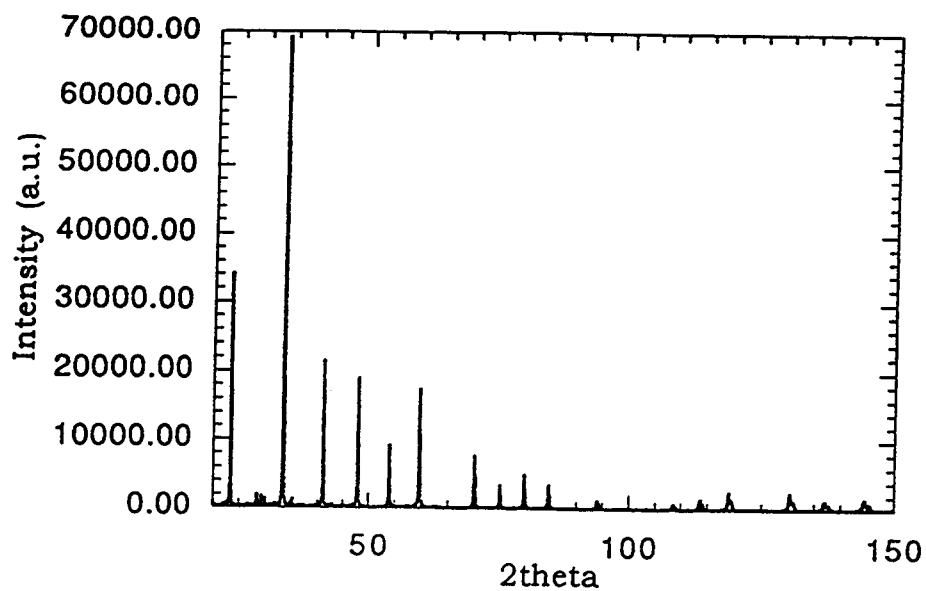
Table 3.8Results of $\text{La}_{.75}\text{Sr}_{.25}\text{AlO}_{3-y}$ X-Ray Refinement in $R\bar{3}c$ and $Pm\bar{3}m$

Variable	Pm3m	R-3c
a (Å)	3.79041 (.00001)	5.3588 ¹ (.00004)
α (degrees)	n/a	60.037 (.001)
Oxygen Position (x)	n/a	-0.2239 (.0007)
Fraction La	0.76 (.015)	0.743 (.013)
Fraction Sr	0.24 (.015)	0.257 (.013)
Phase Fraction SrAl_2O_4	0.0586 (.0004)	0.0489 (.0009)
UIISO (Sr, La)	0.00053 (.00002)	0.00061 (.00001)
UIISO (Al)	0.0027 (.0005)	0.0035 (.0005)
UIISO (O)	0.0091 (.0008)	0.0050 (.0009)
wRp	0.1369	0.1302
Rp	0.0936	0.0886
χ^2	7.923	7.171

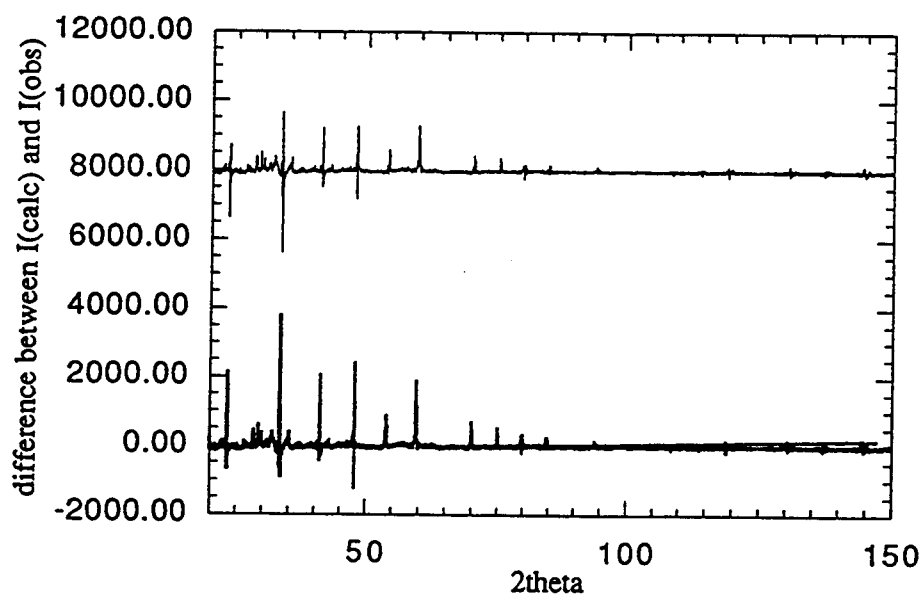
¹The pseudo-cubic lattice constant, for comparison with Pm3m results, is 3.789 Å.

groups gave very similar fits, with the rhombohedral being slightly better. In both cases, the strontium occupancy refined to approximately 25%. This to be expected, as there are more variables to manipulate in this space group. Plots of the calculated x-ray pattern vs. the experimental pattern are given in Figure 3.10. The fit is almost identical for each refinement, with the same small errors in intensity present in some of the low angle peaks. The refinement results were too similar to make a judgment on symmetry from the x-ray data, so neutron diffraction data was obtained and refined.

The neutron refinements were only successful in the space group $R\bar{3}c$. The results from this refinement are given in Table 3.9. The statistics are rather high due to the presence of impurity phases. In addition to the SrAl_2O_4 , peaks belonging to SrAlLaO_4 were also present. It is interesting that the lattice angle refined to a position farther from



(a)



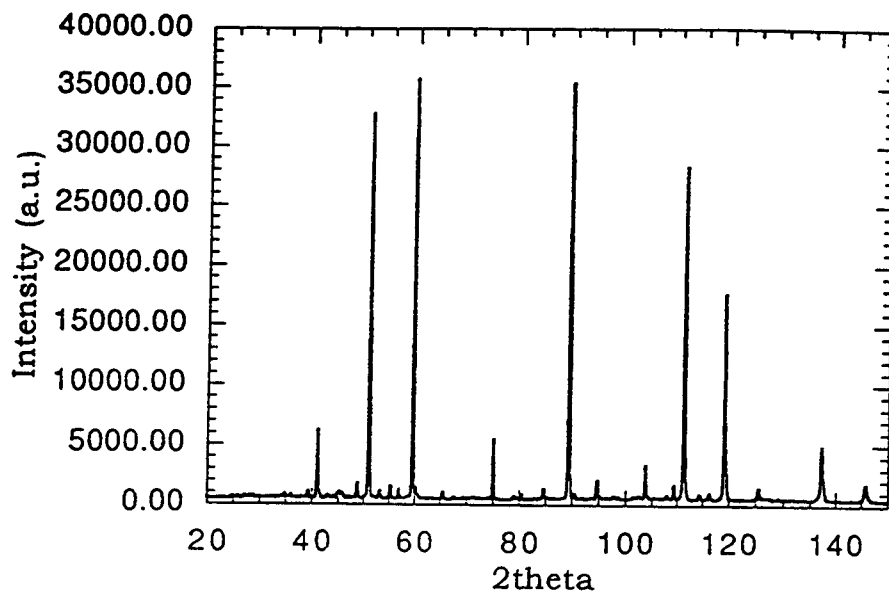
(b)

Figure 3.10 (a) Observed x-ray powder diffraction pattern from $\text{La}_{0.75}\text{Sr}_{0.25}\text{AlO}_{3-y}$, and (b) difference patterns from Pm3m (top) and R3c (bottom). Note the similarities in the difference patterns.

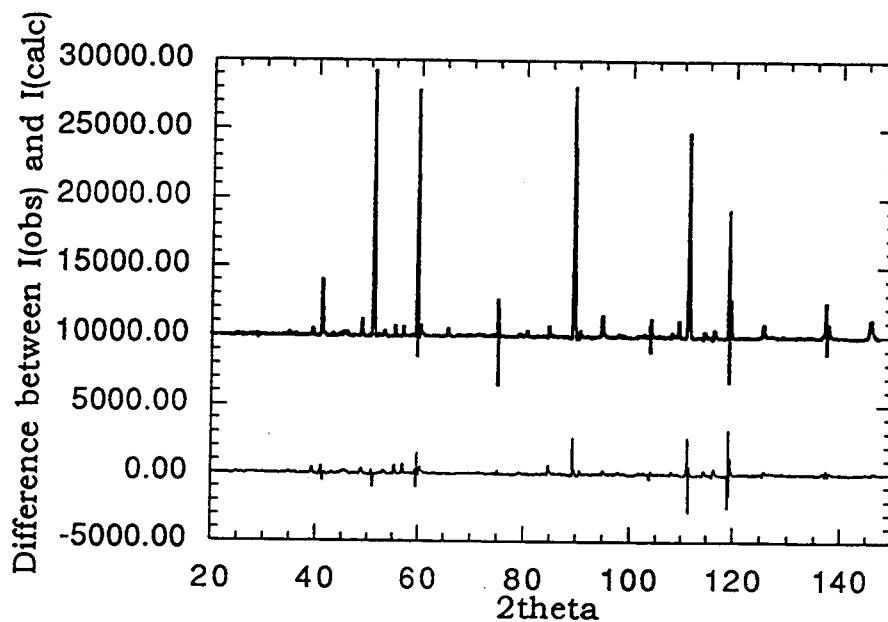
Table 3.9Results from Neutron Diffraction Refinement of $\text{La}_{.75}\text{Sr}_{.25}\text{AlO}_{3-y}$

Parameter	Refined Value
space group	R-3c
λ_{neutron}	1.8857
a (Å)	5.3533 (.00004)
α (degrees)	60.066 (.0001)
Oxygen Position (x)	-0.2315 (.0002)
Fraction La	not refined
Fraction Sr	not refined
Fraction O	0.976 (.007)
UIISO (La, Sr)	0.0035 (.0005)
UIISO (Al)	0.0078 (.0001)
UIISO (O)	0.0091 (.0005)
wRp	0.1114
Rp	0.0817
χ^2	12.9

cubic in the neutron refinement (60.066 degrees) than in the cubic refinement (60.037 degrees). The oxygen occupancy refined to a value of just below full occupancy (97.6%), which is expected, due to the lower charge of the strontium atom. If the strontium concentration were truly 25% (as given by the x-ray refinements), the general formula would be expected to be $\text{La}_{.75}\text{Sr}_{.25}\text{AlO}_{2.85}$ by charge balance considerations. This would give an oxygen occupancy of 95.8%. The refined value is in fairly close agreement. The lanthanum and strontium occupancies were not refined in the neutron analysis, as they proved to be too closely correlated with each other and the thermal parameters of that site. The thermal parameters are expected to be different from those of the x-ray refinements, as the neutron thermal parameters are a function of nuclear rather than atomic thermal vibrations.



(a)



(b)

Figure 3.11 (a) Observed neutron diffraction pattern from $\text{La}_{0.75}\text{Sr}_{0.25}\text{AlO}_{3-y}$, and (b) difference patterns from $\text{Pm}3\text{m}$ (top) and $\text{R}3\text{c}$ (bottom). Many peaks located in $\text{R}3\text{c}$, and present in the pattern, do not exist in $\text{Pm}3\text{m}$.

Table 3.10

Peaks Visible in Neutron Diffraction Data and Rhombohedral Space Group with No Corresponding Peak in Simple Cubic Space Group

Peak Indices	Two-Theta ($\lambda=1.8857 \text{ \AA}$)	D-spacing (Å)
(210)	48.76	2.284
(20-1)	65.68	1.738
(21-2)	94.79	1.281
(31-1)	94.80	1.281
(421)	94.88	1.280
(432)	94.93	1.279
(410)	109.39	1.155
(30-2)	125.37	1.061
(430)	125.47	1.060
(32-2)	145.77	0.987
(40-1)	145.77	0.987
(42-1)	145.82	0.986
(531)	146.01	0.986
(542)	146.13	0.986

A refinement of the neutron data was attempted in the space group $Pm\bar{3}m$. Difference curves for this refinement and the successful one in $R\bar{3}c$ are shown in Figure 3.11. In each illustration, between the difference plot and the data plots above it, are marks signifying the positions of the peaks of the phases refined into the calculated pattern. For the rhombohedral case, three rows of marks are shown: one for the $\text{La}_{1-x}\text{Sr}_x\text{AlO}_{3-y}$ phase, and one for each impurity phase. The $Pm\bar{3}m$ refinement pattern has only two rows of marks, as only one impurity phase (SrAl_2O_4) was refined into the pattern. The bottom row of marks in each illustration shows the positions of the peaks from the $\text{La}_{0.75}\text{Sr}_{0.25}\text{AlO}_{3-y}$ phase. Note that some high intensity peaks that are observed in the experimental pattern, and marked and refined in the rhombohedral phase, are not found in the cubic refinement. The major

peaks found in the data set that are expected in the rhombohedral space group, but not in the cubic, are given in Table 3.10.

High purity $x=0.15$ samples annealed in different gas environments showed color changes, although different from those found in the standard purity samples initially attempted, and described in the experimental section. The sample was initially annealed in air at 1550 °C, and was white. A fraction of this powder annealed in 10% H₂/90% N₂ at 1500 °C for 10 hours had a very faint pastel yellow tint in comparison to the air annealed powder. Another fraction of this powder annealed flowing O₂ turned a light tan. No vacuum anneal was performed on the high purity sample.

3.4 Discussion

The results from the x-ray structural study clearly show the change in the unit cell of (La_{1-x}Sr_x)AlO_{3-y} as a function of x . The lattice angle decreases from its original value of 60.1°, and smoothly changes toward a cubic value with increasing strontium concentration. The lattice constant appears to increase slightly with increasing strontium. The magnitude of the increase is outside the standard deviations given in the GSAS output file, but it is uncertain whether this is a true measure of the calculational error. The deviations given by the software reflect error in the calculations performed on a particular data set, rather than the range of values different measurements on a particular sample will yield. The oxygen position changes quite slowly at the beginning of the series, but then moves more rapidly toward the cubic position as the strontium concentration becomes larger. This, however, is more suspect than the other trends. Because the scattering factor of oxygen is so

much smaller than that of lanthanum or strontium, small changes in the oxygen position are unlikely to have much impact on x-ray peak intensities and positions when the other, more powerfully scattering, elements, are present. Therefore, the small changes seen are likely within the error in the calculation. The other data showing the compound to make the same structural changes, however, does support the validity of this result. Predictably, the strain in the structure increases with higher concentrations of strontium, as oxygen vacancies are created to maintain charge balance.

The determinations of individual changes in bond angles and lengths also supports the smooth structural transition. The trend in the Al-O-Al bond angle toward 180° shows the octahedra to decrease their tilt relative to one another. The lanthanum-oxygen bond distances also support the transition, as the shorter and longer distances approach the mean distance as the strontium content increases. Extrapolation of these plots to find the concentration of strontium at which the structure would become cubic gave a value of 46%. However, there is reason to believe that the structure may go cubic at a lower concentration than this. Addition of the Sr onto the La site increases the tolerance factor of the structure only gradually. Many more factors than purely geometrical considerations contribute to the symmetry of a structure. It has been reported that the rhombohedral distortion is the most commonly observed when the tolerance factor is in the range of 0.975 and 1.02 and the ionic charge on the A site cation is also large, as with La^{3+} . This arrangement maximizes the ionic interaction between the A cation and the oxygen (18). In fact, no $\text{A}^{3+}\text{B}^{3+}\text{O}_3$ perovskites have been reported to have the ideal cubic structure at room temperature (10). As the average

ionic charge on the site decreases, so does the magnitude of this interaction. Then, the cubic structure becomes more common. Coupled with the increase in the average A cation size, the decrease in the magnitude of the ionic interaction with strontium substitution may allow other factors, such as covalent interactions, to determine the symmetry. With so many variables, there is no reason to assume a linear relationship in structural changes down to the cubic symmetry. For these reasons, as well as the unlikelihood of incorporating a lower charge cation into the structure with almost complete one-half occupancy, a lower concentration of strontium was chosen to investigate the far end of the transition.

X-ray refinements performed on the $x=0.35$ compound were inconclusive. The refinement proceeded to similar R_p and wR_p values when done either in $R\bar{3}c$ or $Pm\bar{3}m$. The refinement in $Pm\bar{3}m$ resulted in a slightly better calculated pattern fit, but the two were too close to make a distinction. The strontium concentration refined to a value of about 20%. The instability of the refinements in the rhombohedral group likely result from the difficulty of fitting multiple peaks on one position. Where peak splitting exists in the calculated rhombohedral pattern, but none is visible in the x-ray, the same peak fit can be achieved with many different combinations of variables. The close correlations between these variables increase the instability of the refinement. This was not a problem in the cubic space group, as relatively few of the peaks are multiplets, and those that are have the exact same position.

X-ray refinements on the $x=0.25$ sample are also, in themselves, inconclusive. Refinements in both space groups gave very similar fits, as evident in Figure 3.10. Neutron refinements, however, clearly show that

this composition is not cubic. The presence of peaks in the neutron diffraction scan that can be indexed to a rhombohedral cell, but not to a simple cubic one, is the strongest evidence in support of this conclusion. These peaks are of too low intensity in the x-ray scans to differentiate from the background. For this reason, the fit of the *Pm3m* x-ray refinement was not affected by their presence. The peaks may possibly be indexed to a doubled cubic cell (composed of rhombohedral subcells), but the intensities would most likely be impossible to fit.

The intensities of these peaks in the neutron pattern are heavily dependent upon the oxygen positions and occupancy in the structure. Since the x-ray scattering power of oxygen is quite low, the peaks appear to have low intensities in the x-ray diffraction patterns. Hence, little information can be derived from them. The only positional variable between the two space groups is the oxygen position; the A and B cation sites are fixed in both structures. There is a possibility that the structure is metrically cubic, but positionally rhombohedral; that is, the unit cell parameters are those of a cubic cell, but the atoms are shifted off of their ideal positions in the cell. This would be difficult to tell with x-ray data, as the oxygen positions have little effect on the overall pattern. However, the neutron scattering power of oxygen is of the same order of magnitude as that of strontium or lanthanum. Hence, peaks that were almost absent in the x-ray pattern have high intensities in the neutron pattern, allowing oxygen occupancies and positions to be refined with accuracy. The neutron data shows unambiguously that the oxygen position is not on the ideal cubic site, but shifted to a value of about -0.2315 (from an ideal of -0.25). The cell appears to not be metrically cubic as well. This was difficult to tell with the x-ray pattern, as the peaks indicative of

rhombohedral symmetry were of too low intensity to observe. The appearance of these peaks in the neutron patterns show the unit cell to remain somewhat distorted from cubic. The refinement suggests that the structure is oxygen deficient, with a refined oxygen occupancy of 97.6%.

The redox anneals were performed to gain some insight on the nature of the defects in the compound. Before the anneals, the high purity $x=0.15$ sample was a dull white powder. Lower purity samples of the same strontium concentration had been a light tan color, due to impurities in the sample from the use of lower purity reactants. The anneal in oxygen brought about the same light tan color in the high purity sample. Some type of absorbing species was created in the lattice by the oxidizing conditions. One hypothesis is that the oxygen atoms are inserted into the oxygen vacancies. The substitution of strontium creates vacancies on the oxygen site, probably adjacent to the strontium atom. Oxygen deficiencies refined in the neutron powder work show vacancies could exist, and oxygen ion conductivity measurements have also detected vacancies through increased ionic conductivity with increased dopant levels (12). If an oxygen atom is forced into a lattice vacancy by the anneal, it is possible that an electron can become trapped in one of the available oxygen orbitals, creating the O^{1-} radical. This requires an oxygen vacancy (V_o) in the structure to accept atomic oxygen. The formation of the radical can be represented by



This electron trapped on the (Sr: O^{1-}) defect site would be an absorbing species, and it is likely that the concentration of this defect is very low.

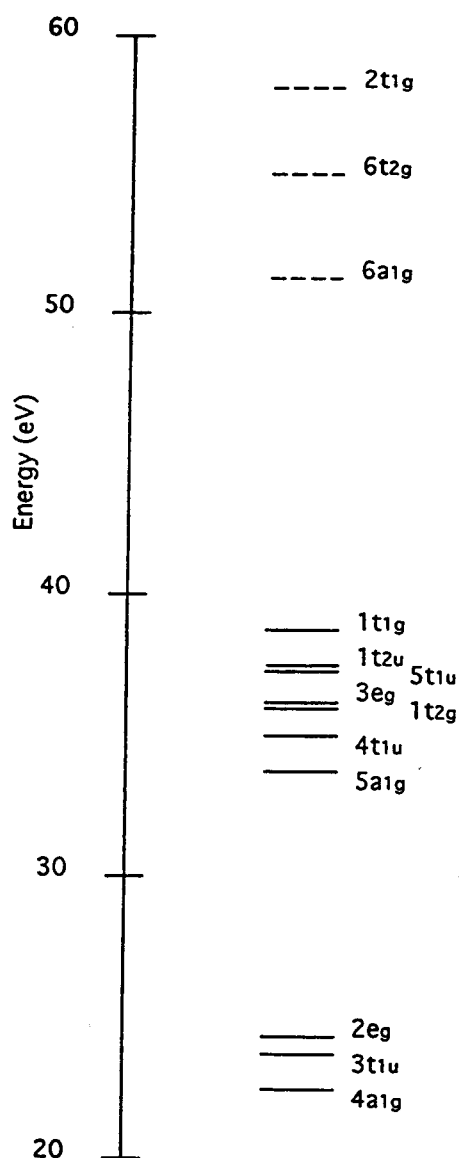


Figure 3.12 Energy level diagram of AlO_6 octahedral network in LaAlO_3 (19). In the pure compound, the highest occupied orbital is the $1t_{1g}$. Reduction may put electrons in the $6a_{1g}$, making a transition between this level and the $6t_{2g}$ possible, although quite weak in intensity due to the different symmetries of the levels. Solid and dashed lines represent filled and empty levels, respectively.

leading to the weakness of color. Electron paramagnetic resonance measurements would help test this hypothesis.

The pale yellow color of the hydrogen reduced samples is most likely created by a different phenomena. Removal of oxygen could result in the addition of electrons to a conduction band in the AlO_6 octahedral network. Reference 19 contains energy levels calculated for BO_6 octahedra in LaBO_3 perovskites for various B cations, which is replicated for LaAlO_3 in Figure 3.12. In pure lanthanum aluminate, the highest occupied energy level is a $1t_{1g}$ molecular orbital at the top of the valence band. The energy between this and the bottom of the conduction band is 13 eV, corresponding to an absorption wavelength of 95.4 nm. This is much too high in energy to affect the absorption of visible light. However, reduction of the powder may result in the insertion of electrons into the $6a_{1g}$ energy levels at the bottom of the conduction band. The next energy level above this is the $6t_{1u}$, with an energy gap of approximately 4 eV separating the two levels. This corresponds to a wavelength of 310 nm, in the UV. It is possible that the absorption band may have a tail extending from the UV into the visible region, resulting in a weak absorption in the violet region of the spectra. Due to the unlike symmetries of the energy levels, the transition would have to occur through coupling with some mechanism that changes the symmetry of one of the levels. It is also possible that the strain in the structure changes the symmetry of the bands. This is another reason the absorption would be expected to be weak. Another band must tail in from the IR to cause the yellow color, but the possible source of this band is less clear. This is only one possible mechanism for the existence of the yellow color. Impurities in the sample with multiple stable valence states

would also be sensitive to reducing conditions, and, if present in low concentrations, could be difficult to detect by chemical analysis, yet still cause a weak color change in the sample.

3.5 Conclusions

The structure of LaAlO_3 is modified by the addition of strontium as a substitutional cation on the lanthanum site, giving a solid solution of the general formula $(\text{La}_{1-x}\text{Sr}_x)\text{AlO}_{3-y}$. With increasing strontium concentration, the lattice angle appears to move continuously toward 60° , at which point the structure would be metrically cubic. Bond angle and distance data supports this, and predicts that the series should reach cubic symmetry at a concentration of 46% strontium. The ultimate solubility of the strontium was not determined due to the difficulty of getting the reaction to go to completion at the temperatures used. Some amount of the phase SrAl_2O_4 was generally present in all the samples of the substituted lanthanum aluminate. This phase did appear to decrease in quantity with increasing reaction temperature, but multiple anneals at 1550°C were not always sufficient to cause the desired reaction to go to completion, and higher temperatures resulted in reactions with the crucible. Higher concentrations of strontium did appear from x-ray refinements to possibly result in a cubic structure, but neutron refinements on an $x=0.25$ sample showed conclusively that the compound was neither metrically nor positionally cubic. Oxygen vacancies appear to form to balance the charge deficiency created by the lower charge strontium. The vacancy concentration refined to a value close to the theoretical. The color changes evident in oxidized samples of these powders may result from an O^{1-} species trapped at a Sr:O lattice

defect. The color change caused by reduction of the samples in hydrogen most likely results from an absorption band created by the insertion of electrons into the lowest conduction band level by the reduction. It is still unclear whether high doping levels create a cubic structure, as x-ray refinements on the $x=0.35$ sample were inconclusive. Neutron refinement of data from such a sample should conclusively determine the symmetry due to the increased intensities of peaks that are observed in the rhombohedral space group, but not in the simple cubic.

3.6 References

1. J. M. Phillips, M. P. Siegal, P. B. van Dover, T. H. Tiefel, J. H. Marshall, C. D. Brandle, G. Berkstresser, A. J. Strauss, R. E. Fahey, S. Sengupta, A. Cassanho, and H. P. Jenssen, *J. Mater. Res.* **7**, 2650 (1992).
2. K. H. Young, G. V. Negrete, M. M. Eddy, J. Z. Sun, T. W. James, McD. Robinson, and E. J. Smith, *Thin Solid Films* **206**, 116 (1991).
3. W. L. Holstein, L. A. Parisi, R. B. Flippen, and D. G. Swartzfager, *J. Mater. Res.* **8**, 962 (1993).
4. S. Geller and V. B. Bala, *Acta Cryst.* **9**, 1019 (1956).
5. J. Coutures and J. P. Coutures, *J. Sol. St. Chem.* **52**, 95 (1984).
6. H. M. O'Bryan, P. K. Gallagher, G. W. Berkstresser, and C. D. Brandle, *J. Mater. Res.* **5**, 183 (1989).
7. D. Reagor and F. Garzon, *Appl. Phys. Lett.* **58**, 2741 (1991).
8. J. G. Bednorz and K. A. Muller, *Mat. Res. Bull.* **18**, 181 (1983).
9. T. A. Vanderah, C. K. Lowe-Ma, and D. R. Gagnon, *J. Am. Ceram. Soc.* **77**, 3125 (1994).
10. R. Guo, P. Ravindranathan, U. Selvaraj, A. S. Bhalla, L. E. Cross, and R. Roy, *J. Mater. Sci* **29**, 5054 (1994).
11. D. Mateika, H. Kohler, H. Laudan, and E. Volkel, *J. Cryst. Growth.* **109**, 447 (1991).
12. J. Mizusaki, I. Yasuda, J. Shimoyama, S. Yamauchi, and K. Fueki, *J. Electrochem. Soc.* **140**, 467 (1993).
13. J. Fergus and C. B. Alcock, *Mater. Lett.* **12**, 219 (1991).
14. A. Gloubokov, A. Klos, J. Fink-Finowiki, and A. Pajaczkowska, *Mater. Res. Bull.* **31**, 271 (1996).
15. A. C. Larson and R. B. Von Dreele, *LANSCE*, Los Alamos National Lab., 1994.
16. D. L. Bish and J. E. Post, eds., *Reviews in Mineralogy, v20: Modern Powder Diffraction*, pp. 282-291, The Mineralogical Society of America, Washington, D.C. (1989).
17. I. D. Brown and R. D. Shannon, *Acta Cryst.* **A29**, 266 (1973).

18. P. M. Woodward, *Acta. Cryst. B.*, accepted 6/96.
19. I. Kojima, J. Adachi, and I. Yasumori, *Surface Science* **130**, 50 (1983).

Chapter 4

Synthesis and Study of Oxyfluoride Perovskites

4.1 Introduction

The search for suitable substrate materials for the growth of high temperature superconducting thin films has centered primarily upon oxides of the perovskite structure. Many binary oxide perovskites have been studied, but only a few, such as lanthanum aluminate and neodymium gallate, have been found to be suitable. Although many compounds of the general formula ABO_3 crystallize in perovskite type structures, relatively few have the correct combination of ions necessary to result in the desired cubic symmetry and good lattice matching with the superconducting materials. Even those that are commonly used do not meet all other desirable criteria, which include similar thermal expansion behavior as the superconductors, low chemical reactivity at elevated temperatures, a low dielectric constant, and low dielectric loss. Table 1.1 lists some compounds that have been tried as substrates in the past. Of the commonly used perovskite materials, only strontium titanate is cubic, and it possesses a dielectric constant prohibitively high for most electronic applications.

Fewer perovskites of the general formula ABF_3 have been tried as substrates. $LiBaF_3$ (1) and $KMgF_3$ (2) have both been suggested, although films of YBCO grown on $LiBaF_3$ lost their superconducting properties. Many other fluoride perovskites are known (3), but, as in the case of binary oxide perovskites, relatively few of them have cubic symmetry at room temperature. Simple fluorides have also been suggested and investigated. CaF_2 , MgF_2 (2), and LiF (4) have all been

either suggested or tried, but have not proven to be superior to the materials currently in use.

To increase the range of obtainable unit cell sizes with cubic symmetry, different mixed perovskite oxides of the general structure $A_2BB'O_6$ have been synthesized and characterized (5,6). The use of two ions on the B site with the correct average valence to give the perovskite stoichiometry has allowed the synthesis of several cubic compounds with close lattice matches to the superconductors, and low dielectric constants and losses. However, difficulties in growing crystals of these materials have limited their use to date.

Perovskites containing more than one type of anion have not been often reported in the literature. Roy attempted the synthesis of oxyfluoride and oxysulfide perovskites (7). To attempt the synthesis of the oxyfluoride perovskites, two approaches were taken. The first to attempt to form a solid solution between known oxide and fluoride perovskites; $KMgF_3$ and $BaTiO_3$ were chosen for the study. These two compounds proved impossible to heat to high enough temperatures together, as the fluoride was volatile, and reaction of the molten fluoride with the fused oxide did not result in a solid solution. The second approach was to determine suitable compositions by geometric considerations. $KTiO_2F$ and $BaMgOF_2$ were chosen as good candidates. Neither compound, in this study, showed the perovskite structure. However, in a later study by Chamberland (8), the $KTiO_2F$ perovskite phase was prepared by first heating anhydrous KF and high purity TiO_2 to form a monoclinic precursor, then heating this compound under high pressure to form a cubic perovskite. Other reported oxyfluoride perovskites are $KNbO_2F$ and $NaNbO_2F$ (9), and the mixed valence

thallium oxyfluoride $Tl^+Tl^{3+}OF_2$. Oxyfluorides are also known in related structures, such as the K_2NiF_4 -type compounds K_2NbO_3F (10) and Sr_2FeO_3F (11).

If the fluoride ions could be replaced in these structures by vacancies in the anion lattice, anion deficient perovskite structures may result. A variety of these have been reported in the literature. $CaFeO_{2.5}$ is an oxygen deficient perovskite that crystallizes in the orthorhombic space group $Pcmn$ (12). Layers of FeO_6 octahedra alternate along b with FeO_4 tetrahedra, and the interstitial sites between the layers, analogous to the perovskite A cation site, are occupied by the calcium ions. Brownmillerite [$Ca_2(AlFe)_2O_5$], an important component of Portland cement, has a similar structure, but crystallizes in the space group $Ibm2$ (13). $SrFeO_{2.5}$ was originally thought to be isostructural with $CaFeO_{2.5}$, but single crystal studies by Harder and Muller-Buschbaum show the substance to crystallize in the space group $Ibm2$ (14). $CaMnO_{2.5}$ was prepared and characterized by Poeppelmeier *et al*, and shown to possess a novel oxygen ordering mechanism, unlike those observed in the reduced ferrites (15). The Mn^{3+} ion is in a square pyramidal environment, due to its d^4 electronic configuration, rather than the tetrahedral and octahedral Fe^{3+} sites in the ferrites. A mixed perovskite oxygen deficient system, Sr_2FeTiO_{6-x} ($x < 8.3$), was studied and characterized by Mossbauer spectroscopy, x-ray diffraction, and neutron diffraction, by Greaves and Buker (16). X-ray diffraction implied that, unlike the $SrFeO_{2.5}$ family and the $CaMnO_{2.5}$ structure, the vacancies did not show long range order, and the cell could be indexed to a simple cubic perovskite. Most recently, Chen *et al* reported the synthesis of $SrCuO_{2.5}$. The compound is an orthorhombically distorted perovskite,

crystallizing in the space group $Pb3m$ (17). The structure is of square pyramidal CuO_5 groups, with oxygen vacancies ordering in the CuO_2 layers of the parent perovskite structure.

This chapter presents the results of the attempted synthesis of oxyfluorides of the mixed perovskite type, and one compound of the simple perovskite type. Just as the substitution of two ions on the B site of an oxide perovskite increases the number of cubic compositions possible, it was envisaged that a similar range of compositions may exist for the oxyfluoride. The general formula of the syntheses attempted is $A^{2+}B^{2+}B'^{5+}O_5F$ ($A = Ca, Sr, Ba$; $B = Mg$; $B' = Nb, Ta$). In addition to these compounds, syntheses of the oxygen deficient analogues $A^{2+}B^{2+}B'^{5+}O_{5.5}$ were attempted to see if anion deficient phases would form, and whether a different structure than the oxyfluoride would result. The same was tried with the simple perovskite, $CaAlO_2F$.

4.2 Experimental

A variety of synthetic routes to oxyfluorides are found in the literature. Typically, reactants comprised of simple oxides and fluorides of the desired metals are ground together and sealed in a gold tube in a dry box under dry O_2 before heating (18), or heated under a flow of an inert gas (19). Hydrothermal syntheses have also been reported (20), as have standard solid state syntheses carried out in air (10,11).

The syntheses of Ba_2MgNbO_5F and Ba_2MgTaO_5F , and the corresponding anion deficient compounds, were first attempted in air. Stoichiometric amounts of BaF_2 (Johnson-Matthey), $BaCO_3$ (Baker), $Mg(NO_3)_2 \cdot 6H_2O$ (EM Science, 99%), and Nb_2O_5 (Johnson-Matthey, 99.8%), or Ta_2O_5 (Alfa, 99.95%) were ground together with an agate

mortar and pestle. The powders were heated at 1.5 °C/min to 330 °C, at which temperature the magnesium nitrate decomposes, then to 850 °C at a rate of 8.3 °C/min, and held for 16 hrs. X-ray diffraction patterns were taken after each heating cycle. There was no evidence of a perovskite phase after heating to this temperature, so the samples were reground and heated to 1000 °C for 16 hours in air. By 1000 °C x-ray diffraction revealed evidence of a perovskite like phase, along with unreacted starting material. A phase pure sample was formed by further annealing at 1300 °C for 16 hours. Small peaks at low angles in the tantalum samples could be indexed to face centered and hexagonal peaks.

Refinements of these phases were attempted using the GSAS Rietveld refinement software (21). Two-theta diffraction scans from 10° to 150° were collected on a Siemens D-5000 Diffractometer using a step size of 0.02°. Difficulty was met in refining both of the oxyfluoride compounds, as the peak intensities, lattice parameters, and profiles could not be fitted successfully. In addition, the isotropic thermal parameters would assume very negative values when allowed to refine. The 2Ba/Mg/Nb/O/F mixture was heated to 1400 °C, and the same data collection routine was used to record another x-ray diffraction pattern. In this sample, a small degree of peak splitting was noticed in higher angle peaks. The type of splitting seemed to be characteristic of a two phase mixture with similar lattice constants. It appeared that a mixture of an oxyfluoride and an oxide perovskite were made through synthesis in air. Most likely, BaF₂ reacted with H₂O vapor in the air at the elevated temperatures that seem necessary to form these oxyfluorides, resulting in the loss of fluorine as HF from the reaction mixture, and the formation of a multiphase product. This would explain the difficulty in refining the

structures. Decomposition of oxyfluorides synthesized in air above 1200 °C was also reported by Galasso and Darby (10,11) in $\text{Sr}_2\text{FeO}_3\text{F}$ and $\text{K}_2\text{NbO}_3\text{F}$.

The syntheses of $\text{Ba}_2\text{MgNbO}_5\text{F}$, $\text{Ba}_2\text{MgTaO}_5\text{F}$, $\text{Ba}_2\text{MgNbO}_{5.5}$, and $\text{Ba}_2\text{MgNbO}_{5.5}$ were also attempted under flowing argon. The reactants were heated to 900 °C for 16 hours, then reground and heated to 1000 °C. Diffraction again revealed both a perovskite like phase and starting material. Two 16 hour anneals proved sufficient to yield products with minimal impurities.

Syntheses of $\text{Sr}_2\text{MgNbO}_5\text{F}$, $\text{Sr}_2\text{MgTaO}_5\text{F}$, $\text{Ca}_2\text{MgNbO}_5\text{F}$, and $\text{Ca}_2\text{MgTaO}_5\text{F}$, and the corresponding oxide of each composition, were also attempted in air. SrF_2 (Cerac, 99%), SrCO_3 (Mallinckrodt, 99.9%), CaF_2 (Baker, 99.5%), and CaCO_3 (Mallinckrodt, 99.8%) were used as the source of the A cations and fluoride ion in the respective compounds. The same reaction conditions as those for the barium compounds were used, except that temperatures of 1450 °C were necessary to remove SrF_2 impurities. Refinements of these compounds encountered the same problems as those of the barium compounds, again suggesting fluorine loss. Syntheses were therefore repeated under argon. Full reaction of SrF_2 was not achieved, although the only peaks in the x-ray pattern belonged to the tetragonally distorted perovskite product and the strontium fluoride, with no evidence of other reactants. Subsequent heatings of 900, 1100, 1200, 1250, 1300, 1300, and finally 1350 °C were necessary to remove SrF_2 impurities. It was hoped that the flowing argon ambient would prevent the loss of fluorine from these samples, but refinements on these compounds were again unsuccessful.

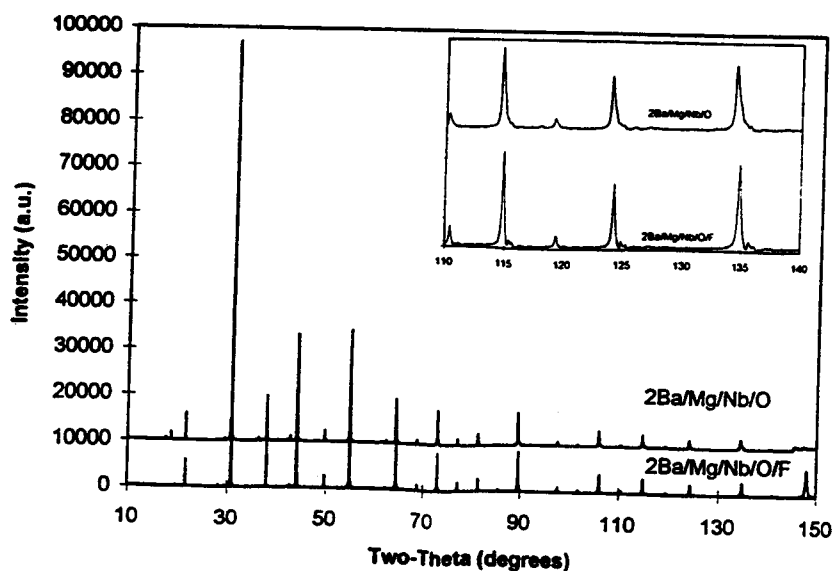
The compounds resulting from the 2Ca/Mg/Ta/O/F, 2Ca/Mg/Nb/O/F reactions, and the corresponding oxides, all appeared orthorhombic from the x-ray scans. Multiple anneals at 1425 °C failed to yield a phase pure product. As this project was attempting to identify substrate materials of higher symmetry, these compounds were not resynthesized under argon.

The binary compound attempted, CaAlO₂F, did not form a perovskite phase at temperatures as high as 1450 °C in air. The product phase indexed completely to the phase 11CaO·7Al₂O₃·CaF₂ in the JCPDS Powder Diffraction File. This further suggests that fluorine loss was a problem with air annealed samples, as the formation of this product requires the loss of approximately 85% of the initial fluorine.

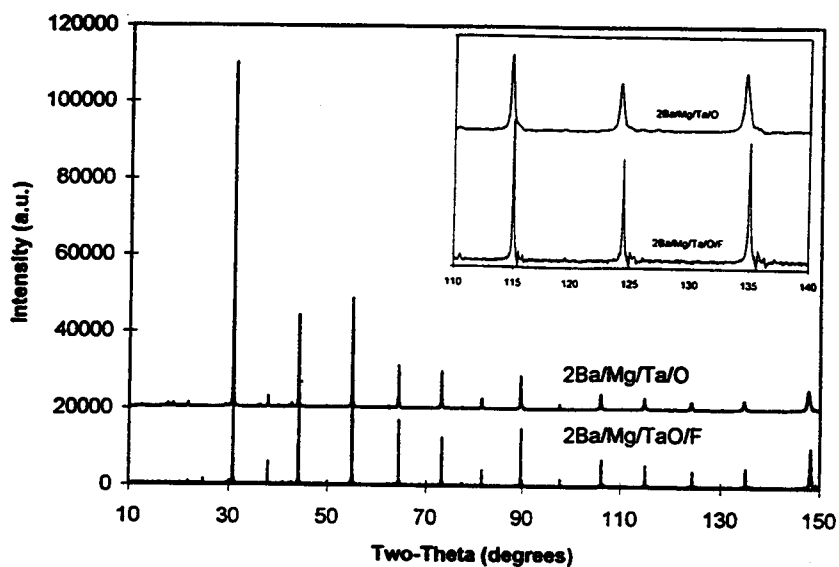
4.3 Results

4.3.1 X-ray Powder Diffraction Patterns

Figure 4.1 (a) shows a comparison between the powder x-ray diffraction patterns of the 2Ba/Mg/Nb/O/F and 2Ba/Mg/Nb/O products. The Cu K α ₂ peaks have been stripped from the plots. From the patterns, the powders both appear to have the structure of a simple perovskite. Two small impurity peaks are visible in the 2Ba/Mg/Nb/O pattern at angles of approximately 19° and 37° two-theta. These peaks do not index to doubled cell, or to a tetragonally or rhombohedrally distorted cell. Figure 4.1 (b) gives the same comparison for 2Ba/Mg/Ta/O/F and 2Ba/Mg/Ta/O products. Again, the peak positions and intensities are very similar for the two compounds. However, the oxide peaks significantly broaden with increasing angle in comparison with those of the oxyfluoride. This is not surprising, as



(a)



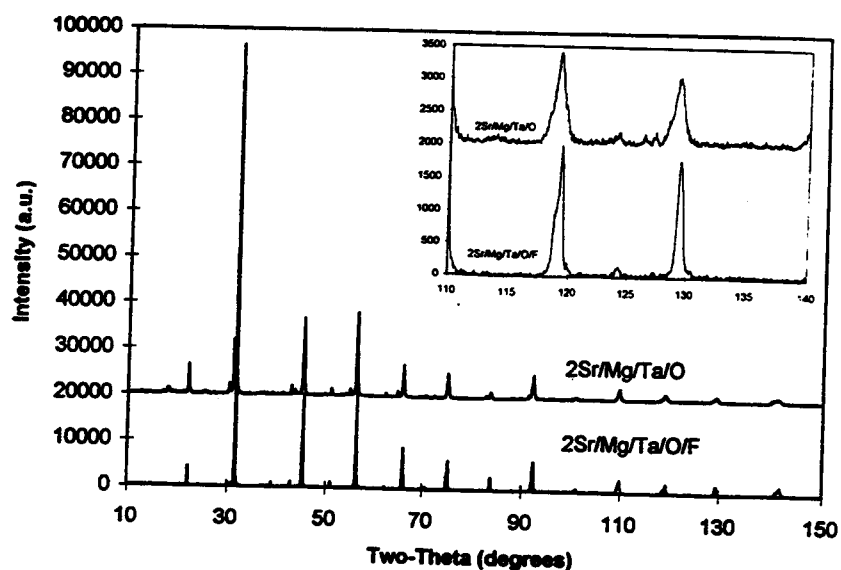
(b)

Figure 4.1 (a) X-ray powder diffraction patterns of 2Ba/Mg/Nb/O/F and 2Ba/Mg/Nb/O reaction mixtures, showing the similarities between the oxide and oxyfluoride patterns, as well as the slight peak broadening in the oxide (inset). (b) X-ray pattern of 2Ba/Mg/Ta/O/F and 2Ba/Mg/Ta/O. Peak broadening is pronounced between these two compounds.

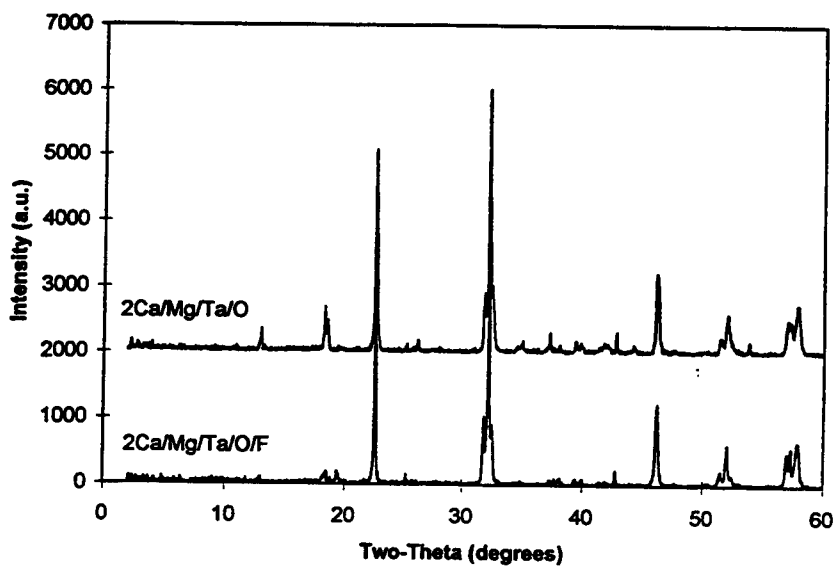
halide additions are frequently used to improve the crystallinity of oxides. Small peaks in both the barium magnesium tantalum oxyfluoride and the control sample index to a doubled face centered cell [the (111) at 18.2° , for example], but are very low in intensity.

Figure 4.2 (a) shows a comparison between the x-ray diffraction patterns of the products from the 2Sr/Mg/Ta/O/F and 2Sr/Mg/Ta/O reactions. Neither of these structures were successfully refined, although all peaks can be indexed to those of a distorted perovskite in the space group $I4/mcm$.

Figure 4.2 (b) shows the same comparison for 2Ca/Mg/Ta/O/F and 2Ca/Mg/Ta/O products. These x-ray patterns were taken after heating the samples to 1425°C . The two are very similar in appearance. The major peaks appear to belong to an orthorhombic phase, but some small peaks do not fit such a phase, pointing to the possible existence of other phases. The peak positions and widths appear similar for each pattern, although the splitting is more easily seen in the high angle peaks in the oxyfluoride sample. Due to the presence of the secondary phases, no high angle x-ray data was gathered for the calcium compounds.



(a)



(b)

Figure 4.2 X-ray powder diffraction patterns for (a) 2Sr/Mg/Ta/O/F and 2Sr/Mg/Ta/O , and (b) 2Ca/Mg/Ta/O/F and 2Ca/Mg/Ta/O . The peak broadening differences are significant in the strontium compounds. The calcium compound patterns are also similar to each other.

4.3.2 X-ray Powder Refinements

Refinements were initially attempted with two models: a fixed barium site occupancy and a variable barium site occupancy. With this approach a potential difficulty in the analysis was found, as the two schemes gave an essentially identical agreement to the observed data despite major differences in the models. Certain peaks in x-ray diffraction are sensitive only to the relative scattering power between the A and B cation sites of the perovskite structure. When both A and B site occupancies are allowed to refine freely, it is possible for the refinement to converge upon a minima other than the true minima. To solve this difficulty, chemical analysis was obtained, and used as the starting point in another series of refinements. Results from all three schemes are presented below.

4.3.2.1 *Ba/Mg/Nb/O/F*

A summary of the refinement performed on 2Ba/Mg/Nb/O/F product is given in Table 4.1, and final observed, calculated, and difference plots are given in Figure 4.3. In the first scheme, the variables allowed to refine freely in the final cycles were the isotropic thermal parameter of barium, the histogram scale factor, 3 background terms, 6 profile functions, and the zero point. The magnesium and niobium fractional occupancies were constrained give full occupancy of the B site, and the isotropic thermal parameters of multiple ions occupying one position (e.g. Mg/Nb and O/F) were constrained to have the same value. This refinement resulted in final agreement factors of $wR_p=11.93\%$, $R_p=8.37$, $R_f=2.14$, and $\chi^2=6.819$. In the second case, the fractional occupancy of barium was also allowed to refine. The third scheme again

Table 4.1**Summary of 2Ba/Mg/Nb/O/F Product Refinements**

	Fixed Ba Occupancy	Variable Ba Occupancy	Microprobe Occupancies
a (Å)	4.08552 (2)	4.08552 (2)	4.08552 (2)
Ba Occupancy	1	0.883 (6)	1
Zero point (°)	-0.0846 (7)	-0.0846 (7)	-0.0846 (7)
Space group (Number)	Pm3m (221)	Pm3m (221)	Pm3m (221)
Data range (°2θ)	10-150	10-150	10-150
Step size (°2θ)	0.02	0.02	0.02
Time per step (sec)	5.0	5.0	5.0
Number of data points	7001	7001	7001
Number of reflections	56	56	56
Number of variables	16	17	16
wR _p (%)	11.93	11.85	11.94
R _p (%)	8.37	8.30	8.46
R _f (%)	2.12	2.14	2.33
χ ²	6.819	6.723	6.828

Table 4.2

**Atomic Coordinates, Fractional Occupancies, and Thermal Parameters
from 2Ba/Mg/Nb/O/F Refinements
(Top Table from .5Mg/.5Nb Starting Occupancy, Bottom from EMPA)**

Atom	x	y	z	Scheme 1 Refined Site Occupancy	Scheme 1 U _{iso} (Å ³)	Scheme 2 Refined Site Occupancy	Scheme 2 U _{iso} (Å ³)
Ba	.5	.5	.5	1.00 (fixed)	.00314 (1)	.883 (6)	.00340 (10)
Mg	0	0	0	.411 (3)	.00226 (3)	.527 (6)	.00160 (20)
Nb	0	0	0	.589 (3)	.00226 (3)	.473 (6)	.00160 (20)
O	.5	0	0	.833 (fixed)	.00496 (6)	.833 (fixed)	.01510 (90)
F	.5	0	0	.167 (fixed)	.00496 (6)	.167 (fixed)	.01510 (90)

EMPA Data and Refinements Starting from EMPA	Site Occupancy from EMPA	→	Site Refined to (Scheme 3)	U _{iso}
Ba	1		1	.00356 (10)
Mg	.37		.371 (3)	.00239 (20)
Nb	.59		.599 (3)	.00239 (20)
O	.91		.91 (fixed)	.0191 (60)
F	.073		.07 (fixed)	.0191 (60)

fixes the barium site occupancy at 1, but starts the refinement from the site occupancies given by microprobe. All refinements resulted in statistically similar fits. The plots given in Figure 4.3 were generated by the microprobe occupancy refinement. Calculated and difference plots from the other two schemes are visually identical, and hence not given.

Atomic positions, refined isotropic thermal parameters, and refined fractional site occupations for the 2Ba/Mg/Nb/O/F product are given in Table 4.2. The magnesium and niobium fractional occupancy refined to 0.411 and 0.589 respectively when the barium occupancy was fixed at 1.0, significantly different from the ideal .5 for each ion. When the barium fractional occupancy was allowed to refine, it converged to a value of 0.883, magnesium and niobium occupancies to 0.52 and 0.48, and deviations increased in the thermal parameters. Starting from the

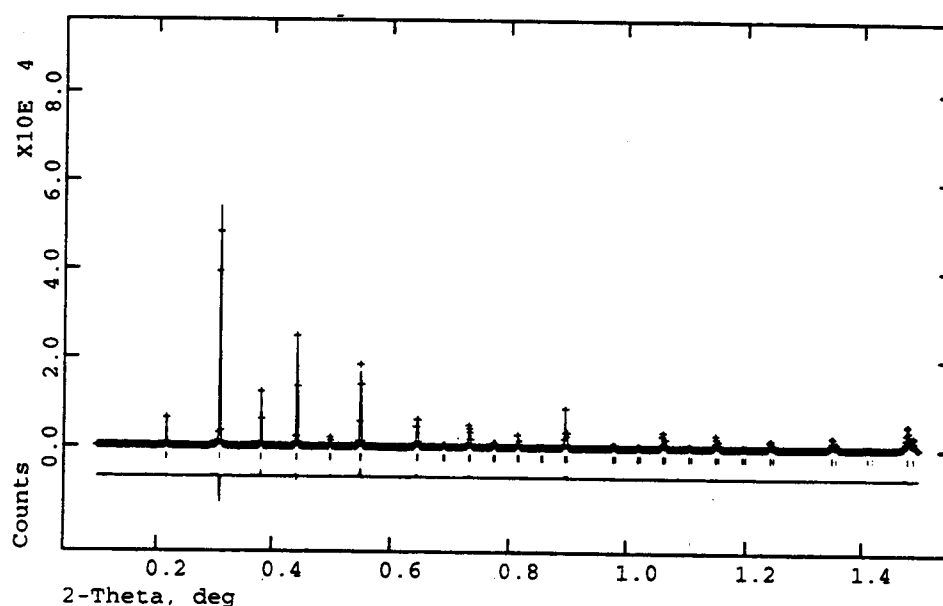


Figure 4.3 Observed (+), calculated (—), and difference (bottom) powder x-ray diffraction patterns of the 2Ba/Mg/Nb/O/F product refinement.

microprobe values, the site occupancies did not shift, strongly suggesting that the microprobe data is correct.

4.3.2.2 Ba/Mg/Ta/O/F

Summaries of the 2Ba/Mg/Ta/O/F reaction product refinements are given in Table 4.3, and atomic positions, isotropic thermal parameters, and fractional occupations refined for each scheme are given in Table 4.4, along with occupancies given by EMPA. The final observed, calculated, and difference patterns are given in Figure 4.4. As in the case of the 2Ba/Mg/Nb/O/F refinement, stable minima were reached both when the barium occupancy was fixed or allowed to vary, and good agreement with observed profiles was achieved with either model. EMPA gave B cation site occupancies close to those calculated by the initial scheme 1 refinement (Ba fixed at 1). Starting from EMPA observed occupancies resulted in convergence with essentially no shift from the

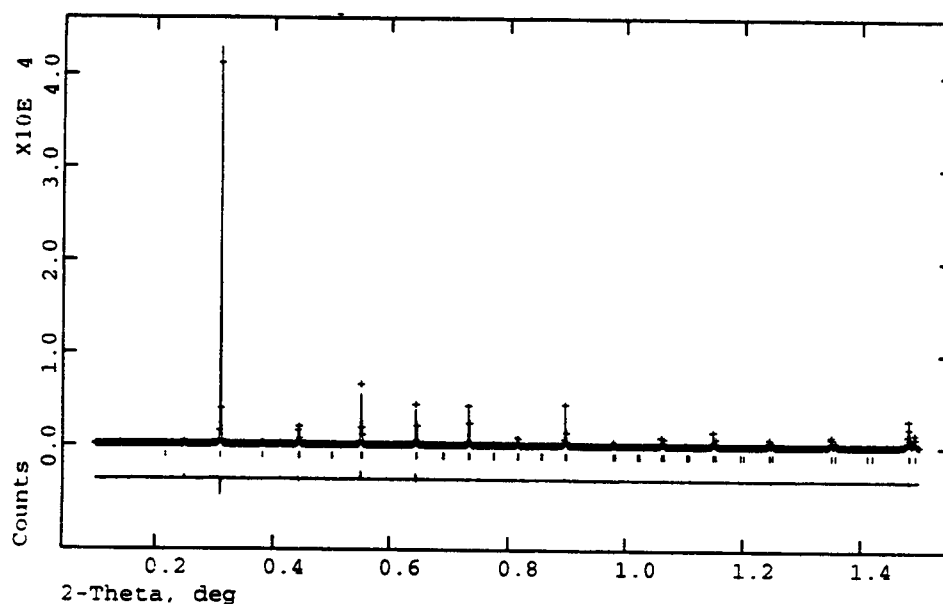


Figure 4.4 Observed (+), calculated (—), and difference (bottom) powder x-ray diffraction patterns of the 2Ba/Mg/Ta/O/F refinement.

Table 4.3**Summary of 2Ba/Mg/Ta/O/F Product Refinements**

	Fixed Ba Occupancy	Variable Ba Occupancy	Microprobe Occupancies
a (Å)	4.08393 (1)	4.08393 (1)	4.08393 (1)
Ba Occupancies	1	0.91 (2)	1
Zero point (°)	-0.0414 (2)	-0.0414 (2)	-0.0414 (2)
Space group (Number)	Pm3m (221)	Pm3m (221)	Pm3m (221)
Data range (°2θ)	10-150	10-150	10-150
Step size (°2θ)	0.02	0.02	0.02
Time per step (sec)	5.0	5.0	5.0
Number of data points	7001	7001	7001
Number of reflections	56	56	56
Number of variables	16	17	16
wR _p (%)	14.30	14.28	14.33
R _p (%)	9.98	9.96	10.01
R _f (%)	4.77	4.51	5.02
χ ²	4.72	4.713	4.745

Table 4.4

**Atomic Coordinates, Fractional Occupancies, and Thermal Parameters
from 2Ba/Mg/Ta/O/F Product Refinements
(Top Table from .5Mg/.5Ta Starting Occupancy, Bottom from EMPA)**

Atom	x	y	z	Scheme 1 Refined Site Occupancy	Scheme 1 U _{iso} (Å ²)	Scheme 2 Refined Site Occupancy	Scheme 2 U _{iso} (Å ²)
Ba	.5	.5	.5	1.00 (fixed)	.0052 (6)	.91 (2)	.0048 (6)
Mg	0	0	0	.454 (5)	-.0002 (700)	.546 (6)	.0004 (7)
Nb	0	0	0	.545 (5)	-.0002 (700)	.454 (6)	.0004 (7)
O	.5	0	0	.833 (fixed)	.006 (1)	.833 (fixed)	.012 (1)
F	.5	0	0	.167 (fixed)	.006 (1)	.167 (fixed)	.012 (1)

EMPA Data and Refinements Starting from EMPA	Site Occupancy from EMPA	→	Site Refined to (Scheme 3)	U _{iso}
Ba	1		1	.0052 (5)
Mg	.41		.420 (5)	-.02 (7)
Ta	.56		.550 (5)	-.02 (7)
O	.88		.88(fixed)	.0050 (10)
F	.11		.11 (fixed)	.0050 (10)

initial values, suggesting that the cation site occupancies given by EMPA were correct. Small peaks at low angles in the diffraction pattern indexed to a doubled face centered cell. However, the intensities of the peaks were extremely small, and the structure was not successfully refined as a face centered cell.

4.3.2.3 Ba/Mg/Nb/O

Summaries of the three refinements performed on the 2Ba/Mg/Nb/O sample are given in Table 4.5. Atomic positions, isotropic thermal parameters, microprobe data, and fractional site occupancies are given in Table 4.6, and calculated, observed and difference patterns generated from the microprobe data refinement are shown in Figure 4.5. The microprobe occupancy refinement converged to similar B site

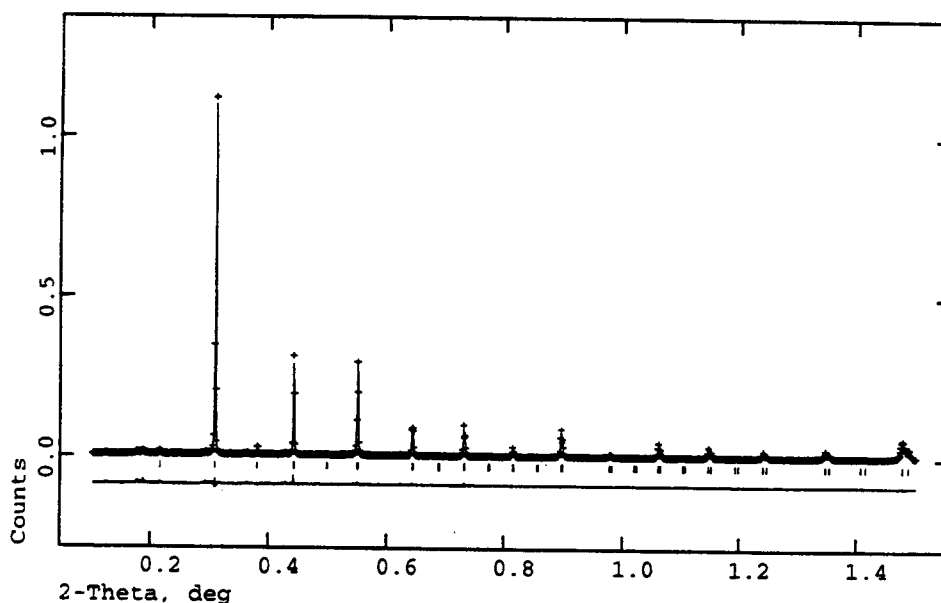


Figure 4.5 Observed (+), calculated (—), and difference (bottom) powder x-ray diffraction patterns generated from 2Ba/Mg/Nb/O reaction product.

Table 4.5
Summary of 2Ba/Mg/Nb/O Refinements

	Fixed Ba Occupancy	Variable Ba Occupancy	Microprobe Occupancies
a (Å)	4.09278 (5)	4.09278 (5)	4.09278 (5)
Ba Occupancies	1	0.91 (.01)	1
Zero point (°)	-0.0311 (6)	-0.0311 (6)	-0.0311 (6)
Space group (Number)	Pm3m (221)	Pm3m (221)	Pm3m (221)
Data range (°2θ)	10-150	10-150	10-150
Step size (°2θ)	0.02	0.02	0.02
Time per step (sec)	5.0	5.0	5.0
Number of data points	7001	7001	7001
Number of reflections	56	56	56
Number of variables	16	17	16
wR _p (%)	13.45	13.41	13.46
R _p (%)	8.10	7.97	8.21
R _f (%)	2.38	2.30	2.14
χ ²	13.30	13.21	13.32

Table 4.6

Atomic Coordinates, Fractional Occupancies, and Thermal Parameters
from 2Ba/Mg/Nb/O Refinements
(Top Table from .5Mg/.5Nb Starting Occupancy, Bottom from EMPA)

Atom	x	y	z	Site Occupancy	U _{iso} (Å ²)	Site Occupancy	U _{iso} (Å ²)
Ba	.5	.5	.5	1.00 (fixed)	.0083 (2)	.91 (1)	.0085 (3)
Mg	0	0	0	.383 (4)	.0064 (3)	.47 (1)	.0061 (4)
Nb	0	0	0	.617 (4)	.0064 (3)	.53 (1)	.0061 (4)
O	.5	0	0	.916 (fixed)	.0056 (9)	.916 (fixed)	.013 (1)

EMPA Data and Refinements Starting from EMPA	Site Occupancy from EMPA	→	Site Refined to	U _{iso} Refined to
Ba	1		1	.0083 (2)
Mg	.38		.341 (4)	.0066 (3)
Nb	.59		.629 (4)	.0066 (3)
O	.95		.95 (fixed)	.0050 (10)
F	.006		---	---

occupancies (Mg=.34, Nb=.63) as the fixed barium refinement starting from the target .5/.5 B site ratio (Mg=.38, Nb=.62). This is quite close to the known hexagonal perovskites $\text{BaMg}_{.33}\text{Nb}_{.66}\text{O}_3$ and $\text{BaMg}_{.33}\text{Ta}_{.66}\text{O}_3$ (22,23). The .33/.66 compounds appear to be metrically cubic, but the cations order along the (111) direction of the cubic pseudocell. Small reflections at low angles result from this ordering. Small reflections did exist at low angles in this sample, but did not index to either a hexagonal cell or a doubled face centered cell.

4.3.2.4 Ba/Mg/Ta/O

A summary of the refinements performed on the 2Ba/Mg/Ta/O reaction product x-ray data is given in Table 4.7; atomic positions, site occupancies, thermal parameters, and microprobe data are given in

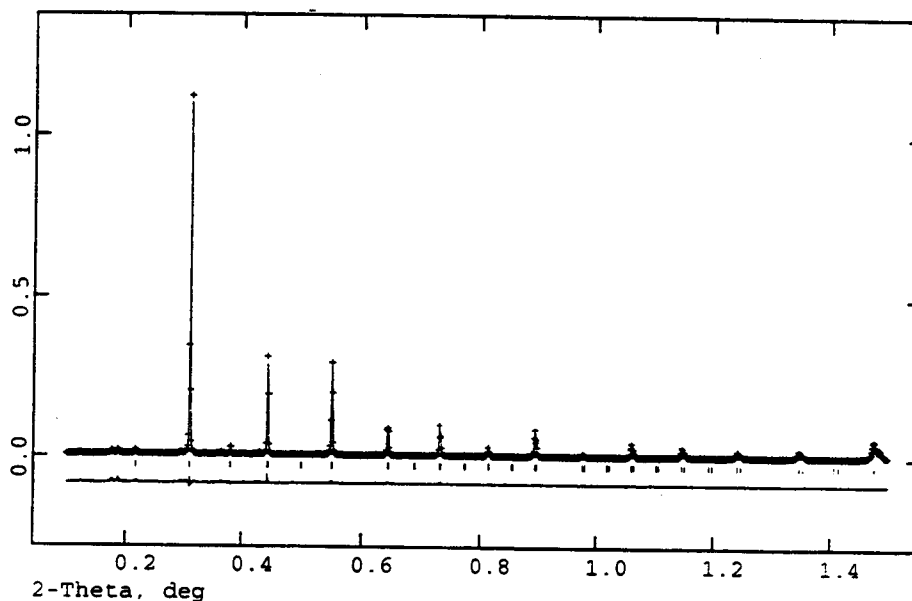


Figure 4.6 Observed (+), calculated (—), and difference (bottom) powder x-ray diffraction patterns generated from 2Ba/Mg/Ta/O product refinement.

Table 4.7

Summary of 2Ba/Mg/Ta/O Refinements

	Fixed Ba Occupancy	Variable Ba Occupancy	Microprobe Occupancies
a (Å)	4.08904 (2)	4.08904 (2)	4.08904 (2)
Ba Occupancy	1	0.92 (1)	1
Zero point (°)	-.0320 (3)	-.0320 (3)	-.0320 (3)
Space group (Number)	Pm3m (221)	Pm3m (221)	Pm3m (221)
Data range (°2θ)	10-150	10-150	10-150
Step size (°2θ)	0.02	0.02	0.02
Time per step (sec)	5.0	5.0	5.0
Number of data points	7001	7001	7001
Number of reflections	56	56	56
Number of variables	16	17	16
wR _p (%)	10.75	10.16	10.35
R _p (%)	6.60	6.68	6.33
R _f (%)	5.86	5.79	6.29
χ ²	1.310	1.274	1.215

Table 4.8Atomic Coordinates, Fractional Occupancies, and Thermal Parameters
from 2Ba/Mg/Ta/O Refinements
(Top Table from .5Mg/.5Ta Starting Occupancy, Bottom from EMPA)

Atom	x	y	z	Site Occupancy	U _{iso} (Å ²)	Site Occupancy	U _{iso} (Å ²)
Ba	.5	.5	.5	1.00 (fixed)	.0137 (6)	.92 (1)	.0130 (7)
Mg	0	0	0	.454 (4)	-.001 (6)	.486 (6)	-.0004 (60)
Ta	0	0	0	.546 (4)	-.001 (6)	.514 (6)	-.0004 (60)
O	.5	0	0	.916 (fixed)	.009 (1)	.916 (fixed)	.014 (1)

EMPA Data and Refinements Starting from EMPA	Site Occupancy from EMPA	→	Site Refined to	U _{iso} Refined to
Ba	1		1	.0083 (2)
Mg	.39		.341 (4)	.0066 (3)
Ta	.53		.629 (4)	.0066 (3)
O	.86		.86 (fixed)	.0050 (10)
F	..083		.08 (fixed)	.0050 (10)

Table 4.8; and calculated, observed, and difference x-ray powder patterns are given in Figure 4.6. This system was unique in that it showed some ordering peaks that could be indexed to a hexagonal cell, and others to a face centered doubled cell. With these two ordering schemes, the pattern was completely indexed. Both sets of ordering peaks were very small, suggesting that the cations were only partially ordered. Microprobe analysis gave the occupancy of Mg to be quite low (.39), but the occupancy of Ta to be close to .5. Refinement of these values converged to occupancies closer to the .33/.66 ratio. The partial hexagonal ordering further suggests that the ratio is closer to this, as the structure of the known .33/.66 perovskites is hexagonal. A high level of fluorine contamination was also present. This sample had been annealed in a tube furnace that had been used for many prior oxyfluoride syntheses. If a metal fluoride had been volatilized in previous syntheses, then some may have remained in the furnace upon cooling. This could possibly result in the contamination of later reactions. Almost no fluorine was found in the Ba/Mg/Nb/O sample, synthesized earlier in the same furnace, suggesting the microprobe fluorine data is correct.

4.4 Discussion

X-ray diffraction data from products of the $2\text{Sr}/\text{Mg}/(\text{Nb},\text{Ta})/\text{O}/\text{F}$ and $2\text{Sr}/\text{Mg}/(\text{Nb},\text{Ta})/\text{O}$ reactions suggest that the oxyfluoride and oxide reaction mixtures did produce different products. It is not surprising that the high angle peaks of the oxide are far more broad, and reduced in height, compared to those of the product produced from the reactants containing fluorine, as even a small amount of fluorine as an impurity can aid crystallization. Although the oxyfluoride strontium compounds

appeared to be single phase after multiple anneals at 1450 °C, and the patterns could be completely indexed to a tetragonally distorted unit cell, the structure could not be refined with powder x-ray data. The tetragonal distortion of both phases was expected from geometrical considerations. The tolerance factor of the target compound ($\text{Sr}_2\text{MgTaO}_5\text{F}$) is 0.972, and tetragonal structures are common in the tolerance factor range of approximately 0.975 to 1.00. The samples prepared without fluorine showed similar peak positions to the oxyfluoride. Peak splitting was visible in the x-ray diffraction pattern of the oxyfluoride at very high angles. This splitting, seen as a splitting of all high angle peaks into closely spaced doublets, seemed more characteristic of two phases with similar lattice constants than reduced symmetry. This suggests that refinements failed as a result of the product not being single phase.

Powder x-ray diffraction patterns of the $2\text{Ca}/\text{Mg}/(\text{Nb},\text{Ta})/\text{O}/\text{F}$ and $2\text{Ca}/\text{Mg}/(\text{Nb},\text{Ta})/\text{O}$ reaction products show an orthorhombic majority phase and other minority phases, which were not identifiable. The orthorhombic phase was expected, as the tolerance factor of the ideal products was calculated to be 0.938. Below a value of 0.975 or so, orthorhombic structures become the most common. No high angle x-ray data was taken on these compounds. It is therefore unclear whether any differences exist between the two orthorhombic products.

EMPA analysis from the barium samples seems to suggest that the true composition of these compounds is closer to the known compounds of the general formula $\text{A}^{2+}\text{B}^{2+}{}_{.33}\text{B}'^{5+}{}_{.66}\text{O}_3$ than the target $\text{A}^{2+}\text{B}^{2+}{}_{.5}\text{B}'^{5+}{}_{.5}\text{O}_{2.5}\text{F}$. X-ray refinements starting from both the target

composition and the .33/.66 composition converge to cation occupancies close to those given by microprobe.

The 2Ba/Mg/Nb/O/F refinement, starting from the microprobe occupancies, refined to essentially the same magnesium and niobium occupancies (.37 and .60) given by microprobe (.37 and .59). This is also quite close to the minimum found by refining from the ideal composition, and fixing the barium concentration (.41 Mg, .59 Nb). The statistical fit was slightly better for the refinement starting from ideal occupancies, but the differences are so slight as to have little physical significance. The presence of fluorine in this sample was verified by EMPA, and found to be approximately .22, giving a product formula of $\text{BaMg}_{.37}\text{Nb}_{.59}\text{O}_{2.72}\text{F}_{.22}$. The microprobe results did give a different oxygen content than that given in this formula. However, with the large amount of oxygen in the structure, and the difficult nature of obtaining reliable oxygen content data from microprobe analysis, it is assumed that the fluorine concentration is more certain than the oxygen. Therefore, to account for charge balance, the oxygen content was varied in the above formula from that given by EMPA. The ratio of A cations to B cations given by the microprobe analysis is 1/.96, and the occupancy on the anion site from microprobe and charge balance considerations is .98. The lattice constant for the new material was found to be approximately 4.085 (+/- .005) Å. The pseudo cubic lattice constant for the known .33Mg/.66Nb compound, calculated from the (10 $\bar{1}$ 1) d-spacing in the hexagonal structure [a=5.782, c=7.067 (11)], is 4.0857 Å. Comparison of the powder x-ray diffraction pattern of the new compound to the known $\text{BaMg}_{.33}\text{Nb}_{.66}\text{O}_3$ shows the the most intense peak in the experimental

pattern [the pseudo cubic (100)] to be of much higher intensity than that of the .33Mg/.66Nb relative to the rest of the pattern.

The good fits obtained by the variable barium refinements reveal a problem with the refinement of cation occupancies in the perovskite structure. The perovskite structure consists of only 3 atomic sites: the A and B cation sites, and the anion site. When refining peak intensities, the ratios of electron densities on these sites is varied to correctly fit the peak areas. The electron density of oxygen (or fluorine) on the anion site is relatively small compared to the cation sites, so the refinement essentially fits the peaks by varying the A and B cation site electron densities. If the two are allowed to vary simultaneously, many minima can potentially be found that do not reflect the true composition. It is possible, as demonstrated in these experiments, that the minima found by such a refinement does not reflect the true composition. It is therefore necessary to include chemical analysis in the model to differentiate between the various minima.

The composition suggested by microprobe and x-ray refinements raises the question of what happens with the excess magnesium and fluorine, as no second phases are seen in this x-ray pattern. At such high temperatures, it is possible for the fluoride ions to react with water vapor, and be lost in the gas phase as HF. It is also possible for volatile metal fluorides to be formed. The fact that all samples were magnesium deficient, yet showed no impurities in x-ray diffraction patterns, supports this hypothesis.

Similar results were found for the 2Ba/Mg/Ta/O/F refinements. Initial refinements performed on this system with the barium occupancy kept fixed found a minimum relatively close to the occupancies given by

EMPA. This refinement converged to an occupancy of .45 Mg and .55 Ta. Microprobe gave the occupancies to be .41 and .56 respectively. When these values were used as the initial conditions for another refinement, the occupancies converged at .42 and .54. As with the niobium system, the composition seems to lie somewhere between the .3Mg/.6Ta known phase and the .5Mg/.5Ta target composition. Microprobe and refinements gave the B cation ratio to be closer to .5/.5 than in the niobium analogue. This is perhaps supported by the face centered doubling peaks that appear in x-ray diffraction patterns of this compound, as a compound of the target composition would be expected to order by charge and size difference considerations. The actual composition of the product, as determined from microprobe and supported by x-ray refinements, was found to be $\text{BaMg}_{.39}\text{Ta}_{.53}\text{O}_{2.65}\text{F}_{.33}$, giving an A cation/B cation ratio of 1/.92. The anion occupancy from these calculations is .99. As with the niobate, the oxygen content was calculated from charge balance, and assumes the fluorine content to be correct. The lattice constant was found to be 4.084 (+/- .005). The pseudo cubic (100) peak in the x-ray pattern was of much higher intensity relative to the rest of the pattern than in the known .33Mg/.67Ta compound. Also, the superstructure peaks were much smaller relative to the rest of the pattern than in the .33Mg/.66Ta compound.

Interesting results were also found in the compounds prepared without fluorine. The 2Ba/Mg/Nb/O reaction mixture seemed to give an almost single phase product, with two small impurity peaks at low two-theta values. These did not index to face centred or hexagonal doubling peaks, or match any Ba/Mg/Nb/O phases in the JCPDS database.

Refinements starting from the ideal .5/.5 Ba/Nb ratio resulted in the cations readjusting their occupancies to .38 Mg and .62 Nb. This is very close to the known .33 Mg/.66 Ta perovskite. However, hexagonal doubling peaks would be expected if the compound were the .33/.66 compound. Microprobe results give the occupancies to be .38 Mg and .59 Nb, quite close to the initial refinement. Starting a new refinement from the microprobe values resulted in the occupancies converging to .34 Mg and .63 Nb, even closer to the .33/.66 compound. However, peak broadening in the x-ray scans may be supporting evidence that the compound is somewhat off of the .33/.66 composition. The oxygen content of the compound as determined by microprobe was 2.53. This is very low, and does not balance the cation charges. Therefore, the oxygen content was calculated from charge balance considerations to give a compound formula of $\text{BaMg}_{.38}\text{Nb}_{.59}\text{O}_{2.85}\text{F}_{.02}$. This gives an A/B cation ratio of 1/.97, and an anion occupancy of .95. The slight presence of fluorine possibly came from fluorine contamination in the furnace. This contamination was much more evident in the tantalum oxide, described below. The lattice constant was determined to be 4.090 (+/- .005) Å. This is about .005 Å greater than that of the fluorine containing analogue, which is just within experimental error. A lower anion occupancy could possibly result in unit cell expansion.

The results from the 2Ba/Mg/Ta/O refinements were initially somewhat different than those of the niobate. The Mg and Ta cations were found to refine to occupancies closer to the ideal .5/.5 ratio (.45 and .55), when starting from these values, than those in the niobate. Microprobe analysis, however, gave the occupancy of the magnesium to be .39, and the tantalum to be .53. When the refinement was started

with these values, the variables converged to .36 niobium and .56 tantalum, closer to the .33/.66 composition. Ordering peaks from both a hexagonal and a face centered phase were present in the x-ray pattern. These peaks were very small, however, suggesting that the sample was only partially ordered. Much more fluorine was present in this compound than the 2Ba/Mg/Nb/O product. The tantalate was synthesized at a later time, after many other oxyfluorides had been attempted, so it is likely that fluorine contamination in the furnace was greater. It is interesting that the formula given by EMPA for this compound (calculating oxygen from charge balance), $\text{BaMg}_{.39}\text{Ta}_{.53}\text{O}_{2.59}\text{F}_{.25}$, is somewhat closer to the .5/.5 B cation composition than the niobium analogue. This also gives an A cation/B cation ratio of 1/.92, and an anion occupancy of .94. The lattice constant was determined to be 4.089 (+/- .005) Å. As with the niobate, this is about .005 Å greater than the Ba/Mg/Ta/O/F compound, just within experimental error.

4.5 Conclusions

Attempts at synthesizing the mixed perovskites $\text{Ba}_2\text{MgNbO}_5\text{F}$ and $\text{Ba}_2\text{MgTaO}_5\text{F}$ were not successful, in that the target compounds were not synthesized. However, new cubic perovskites with partial substitution of fluorine for oxygen were synthesized. The actual compositions of these materials appear to be intermediate between the target compositions and the known $\text{BaMg}_{.33}(\text{Nb,Ta})_{.67}\text{O}_3$ compounds. The incorporation of fluorine into the lattice appears to allow the greater substitution of the lower charged B cation into the lattice. The anion positions seem to be more fully occupied for the compounds prepared as oxyfluorides

($A_1B_{.96}X_{2.94}$ for the 2Ba/Mg/Nb/O/F and $A_1B_{.92}X_{2.97}$ for the 2Ba/Mg/Ta/O/F) than those prepared as oxides ($A_1B_{.97}O_{2.85}$ for the 2Ba/Mg/Nb/O and $A_1B_{.92}O_{2.82}$ for the 2Ba/Mg/Ta/O), even when fluorine contamination was present, suggesting the compounds prepared as oxides were truly more anion deficient than the oxyfluorides. The results here suggest that a range of solubility between $BaMg_{.33}(Nb,Ta)_{.67}O_3$ and $BaMg_{.5}(Nb,Ta)_{.5}O_{2.5}F_{.5}$ may exist, possibly depending upon the amount of fluorine incorporated into the lattice. It would be interesting to synthesize these compounds again in an excess of fluorine to see if the target compositions can be formed, and whether or not they order. This system was shown to be cubic for the compositions synthesized, and is expected to be cubic across any possible composition range. The lattice constants are too large for the barium compounds to be a good candidate for a new substrate material. However, if a similar such system exists for the Sr/Mg/(Nb,Ta) compounds whose synthesis was unsuccessful in this work, it may still be a good candidate.

4.6 References

1. J. M. Phillips, M. P. Siegal, P. B. van Dover, T. H. Tiefel, J. H. Marshall, C. D. Brandle, G. Berkstresser, A. J. Strauss, R. E. Fahey, S. Sengupta, A. Cassanho, and H. P. Jenssen, *J. Mater. Res.* **7**, 2650 (1992).
2. R. Guo, A. S. Bhalla, L. E. Cross, and R. Roy, *J. Mater. Res.* **9**, 1644 (1994).
3. W. L. W. Ludekens and A. J. E. Welch, *Acta Cryst.* **5**, 841 (1952).
4. J. Hou, personal communication (6/94).
5. C. D. Brandle and V. J. Fratello, *J. Mater. Res.* **5**, 2160 (1990).
6. R. Guo, P. Ravindranathan, U. Selvaraj, A. S. Bhalla, L. E. Cross, and R. Roy, *J. Mater. Sci* **29**, 5054 (1994).
7. R. Roy, *J. Amer. Ceram. Soc.* **37**, 581 (1954).
8. B. L. Chamberland, *Mater. Res. Bull.* **6**, 311 (1971).
9. W. Rudorff and D. Krug, *Z. Anorg. Allg. Chem.* **329**, 211 (1964).
10. F. Galasso and W. Darby, *J. Phys. Chem.* **66**, 1318 (1962).
11. F. Galasso and W. Darby, *J. Phys. Chem.* **67**, 1451 (1963).
12. P. E. F. Bertaut, P. Blum, and A. Sagnieres, *Acta Cryst.* **12**, 149 (1959).
13. A. A. Colville and S. Geller, *Acta Cryst.* **B27**, 2311 (1971).
14. V. M. Harder and H.K. Muller-Buschbaum, *Z. Anorg. Allg. Chem.* **464**, 169 (1980).
15. K. R. Poeppelmeier, M. E. Leonowicz, and J. M. Longo, *J. Solid St. Chem.* **44**, 89 (1982).
16. C. Greaves and R. A. Buker, *Mater. Res. Bull.* **21**, 823 (1986).
17. B-H. Chen, D. Walker, B. A. Scott, and D. B. Mitzi, *J. Solid. St. Chem.* **121**, 498 (1996).
18. J-P Chaminade, M. Cervera-Marzal, J. Ravez, and P. Hagenmuller, *Mat. Res. Bull.* **21**, 1209 (1986).
19. A. R. Storm, *Mat. Res. Bull.* **5**, 973 (1970).

20. B. L. Chamberland, *Mat. Res. Bull* **6**, 425 (1971).
21. A. C. Larson and R. B. Von Dreele, *LANSCE*, Los Alamos National Lab., 1994.
22. F. Galasso and J. Pyle, *Inorg. Chem.* **2**, 482 (1963).
23. F. Galasso and J. Pyle, *J. Phys Chem.* **67**, 1561 (1963).

Chapter 5

Summary

The work presented in this thesis was performed in an attempt to develop better substrate materials for the deposition of high temperature superconducting thin films. In pursuit of this goal, a material previously unreported as a buffer layer was successfully synthesized as a thin film, the structural changes resulting from the chemical modification of a common substrate material were studied in depth, and new oxyfluoride compounds were synthesized and characterized.

An RF magnetron sputtering deposition of thin films from a target of composition $\text{Sr}_2\text{GaTaO}_6$ was developed. These films were shown to grow as highly oriented single crystals on an MgO substrate. A range of sputtering gas composition and deposition temperatures were studied to determine the optimal conditions for the growth of the most uniform film, as evidenced by AFM and SEM images. Results from chemical analyses show the film stoichiometries to differ significantly from the target, yet x-ray diffraction results suggest the film structure is similar to that of the target. Intrinsic defects resulting from cation vacancies seem to be the most probable cause of an observed lattice expansion in the films relative to the bulk phase. SGT films were grown epitaxially on thin films of $\text{YBa}_2\text{Cu}_3\text{O}_{7-x}$, and shown to possess characteristics desirable of buffer layers and interlayers. These films were shown to grow as the desired phase, with no observable chemical reactions between the superconducting film and the SGT. Films of the related compound $\text{Sr}_2\text{AlTaO}_6$ reacted chemically with the YBCO, possibly owing to the

higher temperatures necessary for optimal film growth. The SGT film protected the YBCO from chemical etching, and contained a low concentration of pinholes in the film surface.

The systematic changes in the structure of LaAlO_3 with substitutions of the slightly larger cation Sr^{2+} on the La^{3+} site had been reported in the literature previously, but not characterized in detail, nor had the system been studied as a potential substrate material. Substitutions of strontium were shown to transform the structure both metrically and positionally toward cubic; that is, both the unit cell dimensions and contents moved more toward the ideal positions. A concentration of 25% Sr seemed to result in the complete transformation of the structure to cubic from x-ray diffraction refinements, but neutron diffraction data revealed observed peaks incompatible with cubic symmetry, conclusively showing the structure to be rhombohedral. The substituted compound was found to be susceptible to reduction and oxidization by heat treatments in different gases, whereas the unsubstituted compound was not. The higher strontium concentration samples could be viable substrate materials, as the anisotropy of the dielectric constant is expected to decrease with decreases in structural distortions.

New cubic oxyfluoride perovskites with a composition intermediate between the known $\text{BaMg}_{.33}(\text{Nb},\text{Ta})_{.66}\text{O}_3$ and the intended composition of $\text{BaMg}_{.5}(\text{Nb},\text{Ta})_{.5}\text{O}_{2.5}\text{F}_{.5}$ were successfully synthesized as phase pure products. The compositions of the niobate and tantalate were found by EMPA to be $\text{BaMg}_{.37}\text{Nb}_{.59}\text{O}_{2.72}\text{F}_{.22}$ and $\text{BaMg}_{.39}\text{Ta}_{.53}\text{O}_{2.65}\text{F}_{.33}$. Results from x-ray refinements support these site occupancies. The niobate did not show any cation ordering, while the tantalate showed partial face

centered ordering. A control compound was also synthesized in the Ba/Mg/Nb system using the same cation ratios as the oxyfluoride, but no fluorine. It was found to crystallize as a cubic perovskite, with similar cation ratios as the oxyfluoride. The stoichiometry from EMPA and x-ray refinements was determined to be $\text{BaMg}_{.38}\text{Nb}_{.59}\text{O}_{2.85}\text{F}_{.02}$. The anion occupancy appears to be lower for this compound than the fluorine containing analogue. The lattice constants of all of these compounds are very close to 4.09 Å. These results suggest that a range of compounds between different perovskite compositions can be synthesized with the addition of fluorine to compensate for different cation ratios or charges.

Several questions arose during these studies that remain unanswered at the current time. Buffer layer films sputtered from targets of $\text{Sr}_2\text{GaNbO}_6$ and $\text{Sr}_2\text{AlNbO}_6$ are of interest owing to the expected low dielectric constants of such films. Preliminary results did suggest that higher temperatures were required for the synthesis of these films; this would increase the likelihood of chemical reaction with YBCO films. The solubility limit of strontium in lanthanum aluminum oxide is still unclear. It is also possible that the synthesis of the target $\text{BaMg}_{.5}(\text{Nb},\text{Ta})_{.5}\text{O}_{2.5}\text{F}_{.5}$ oxyfluorides may be possible with excess fluorine, and that the strontium analogues may be good substrate candidates if a successful synthetic route can be found.

Bibliography

- Asano, H., S. Kubo, O. Michikami, M. Satoh, and T. Konaka, *Jpn. J. Appl. Phys.* **29**, L1452 (1990).
- Barkay, Z., D. Racah, E. Grunbaum, and G. Deutscher, *J. Appl. Phys.* **73**, 7585 (1993).
- Bednorz, J. G., and K. A. Muller, *Mat. Res. Bull.* **18**, 181 (1983).
- Bednorz, J. G., and K. A. Muller, *Z. Physik* **B64**, 18 (1986).
- Bertaut, P. E. F., P. Blum, and A. Sagnieres, *Acta Cryst.* **12**, 149 (1959).
- Bish, D. L., and J. E. Post, eds., *Reviews in Mineralogy, v20: Modern Powder Diffraction*, pp. 266-268, The Mineralogical Society of America, Washington, D.C. (1989).
- Bish, D. L., and J. E. Post, eds., pp. 282-291.
- Blanton, T. N., M. Lelenthal, and C. L. Barnes, *Physica C* **184**, 119 (1991).
- Brandle, C. D., and V. J. Fratello, *J. Mater. Res.* **5**, 2160 (1990).
- Brown, I. D., and R. D. Shannon, *Acta Cryst.* **A29**, 266 (1973).
- Brown, R. V., Pendrick, D. Kalokitis, and B. H. T. Chai, *Appl. Phys. Lett.* **57**, 1351 (1991).
- Chamberland, B. L., *Mater. Res. Bull.* **6**, 311 (1971).
- Chamberland, B. L., *Mat. Res. Bull.* **6**, 425 (1971).
- Chaminade, J-P. M. Cervera-Marzal, J. Ravez, and P. Hagenmuller, *Mat. Res. Bull.* **21**, 1209 (1986).
- Chaudhari, P. R. H., Koch, R. B. Laibowitz, T. R. McGuire, and R. J. Gambino, *Phys. Rev. Lett.* **58**, 2684 (1987).
- Chen, B-H., D. Walker, B. A. Scott, and D. B. Mitzi, *J. Solid. St. Chem.* **121**, 498 (1996).
- Colville, A. A., and S. Geller, *Acta Cryst.* **B27**, 2311 (1971).
- Coutures, J., and J. P. Coutures, *J. Sol. St. Chem.* **52**, 95 (1984).

- Eom, C. B., J. Z. Sun, K. Yamamoto, A. F. Marshall, K. E. Luther, T. H. Geballe, and S. S. Laderman, *Appl. Phys. Lett.* **55**, 595 (1989).
- Feenstra, R. L., A. Boatner, J. D. Budai, D. K. Christen, M. D. Galloway, and D. P. Poler, *Appl. Phys. Lett.* **54**, 1063 (1989).
- Fergus, J., and C. B. Alcock, *Mater. Lett.* **12**, 219 (1991).
- Findikoglu, A. T., C. Doughty, S. Bhattacharya, Q. Li, X. X. Xi, T. Venkatesan, R. E. Fahey, A. J. Strauss, and J. M. Phillips, *Appl. Phys. Lett.* **61**, 1718 (1992).
- Fork, D. K., F. A. Ponce, J. C. Tramontana, N. Newman, J. M. Phillips, and T. H. Geballe, *Appl. Phys. Lett.* **58**, 2432 (1991).
- Fratello, V. J., and C. D. Brandle, *J. Mater. Res.* **9**, 2554 (1994).
- Galasso, F., and W. Darby, *J. Phys. Chem.* **66**, 1318 (1962).
- Galasso, F., and W. Darby, *J. Phys. Chem.* **67**, 1451 (1963).
- Galasso, F., and J. Pyle, *Inorg. Chem.* **2**, 482 (1963).
- Galasso, F., and J. Pyle, *J. Phys. Chem.* **67**, 1561 (1963).
- Geerk, J. G., Linker, and O. Meyer, *Materials Science Reports* **4**, 193 (1989).
- Geller, S., and V. B. Bala, *Acta Cryst.* **9**, 1019 (1956).
- Gloubokov, A., A. Klos, J. Fink-Finowiki, and A. Pajaczkowska, *Mater. Res. Bull.* **31**, 271 (1996).
- Greaves, C., and R. A. Buker, *Mater. Res. Bull.* **21**, 823 (1986).
- Guo, R., A. S. Bhalla, L. E. Cross, and R. Roy, *J. Mater. Res.* **9**, 1644 (1994).
- Guo, R., P. Ravindranathan, U. Selvaraj, A. S. Bhalla, L. E. Cross, and R. Roy, *J. Mater. Sci* **29**, 5054 (1994).
- Haefke, H., H. P. Lang, R. Sum, H. J. Guntherodt, L. Berthold, and D. Hesse, *Appl. Phys. Lett.* **61**, 2359 (1992).
- Han, B., D. A. Neumayer, B. H. Goodreau, T. J. Marks, H. Zhang, and V. P. Dravid, *Chem. Mater.* **6**, 18 (1994).
- Han, B., D. Neumayer, D. L. Schulz, T. J. Marks, H. Zhang, and V. P. Dravid, *Appl. Phys. Lett.* **61**, 3047 (1992).

- Harder, V. M., and H. K. Muller-Buschbaum, *Z. Anorg. Allg. Chem.* **464**, 169 (1980).
- Hiskes, R. S., S.A. DiCarolus, J. L. Young, S. S. Laderman, R. D. Jacowitz, and R. C. Taber, *Appl. Phys. Lett.* **59**, 606 (1991).
- Holstein, W. L., L. A. Parisi, R. B. Flippen, and D. G. Swartzfager, *J. Mater. Res.* **8**, 962 (1993).
- Hontsu, S., J. Ishii, T. Kawai, and S. Kawai, *Appl. Phys. Lett.* **59**, 2886 (1991).
- Kojima, I. J., Adachi, and I. Yasumori, *Surface Science* **130**, 50 (1983).
- Konopka, J., I. Wolff, and S. J. Lewandowski, *J. Appl. Phys.* **72**, 218 (1992).
- Kwo, J., M. Hong, D. J. Trevor, R. M. Fleming, A. E. White, R. C. Farrow, A. R. Kortan, and K. T. Short, *Appl. Phys. Lett.* **53**, 2683 (1988).
- Larson, A. C., and R. B. Von Dreele, *LANSCE*, Los Alamos National Lab., 1994.
- Laverghetta, Thomas S., *Microwave Materials and Fabrication Techniques*, pp. 11-13, Artech House, Inc., Dedham, MA (1984).
- Ludekens, W. L. W., and A. J. E. Welch, *Acta Cryst.* **5**, 841 (1952).
- Maeda, H. Y., Tanaka, M. Fukutomi, and T. Asano, *Jpn. J. Appl. Phys.* **27**, 1209 (1988).
- Mao, S. N., X. X. Xi, Q. Li, and T. Venkatesan, *J. Appl. Phys.* **75**, 2119 (1994).
- Mateika, D. H., Kohler, H. Laudan, and E. Volkel, *J. Cryst. Growth* **109**, 447 (1991).
- Mizusaki, J. I., Yasuda, J. Shimoyama, S. Yamauchi, and K. Fueki, *J. Electrochem. Soc.* **140**, 467 (1993).
- O'Bryan, H. M., P. K. Gallagher, G. W. Berkstresser, and C. D. Brandle, *J. Mater. Res.* **5**, 183 (1989).
- Olsson, E. G., Brorsson, P. Å. Nilsson, and T. Claeson, *Appl. Phys. Lett.* **63**, 1567 (1993).

- Phillips, J. M., M. P. Siegal, P. B. van Dover, T. H. Tiefel, J. H. Marshall, C. D. Brandle, G. Berkstresser, A. J. Strauss, R. E. Fahey, S. Sengupta, A. Cassanho, and H. P. Jenssen, *J. Mater. Res.* **7**, 2650 (1992).
- Poepfelmeier, K. R., M. E. Leonowicz, and J. M. Longo, *J. Solid St. Chem.* **44**, 89 (1982).
- Profile User's Guide v1.1*, Sobacim, 1995.
- Ramesh, R., A. Inam, W. A. Bonner, P. England, B. J. Williams, B. J. Meagher, L. Nazar, X. D. Wu, M. S. Hedge, C. C. Chang, and T. Venkatesan, *Appl. Phys. Lett.* **55**, 1138 (1989).
- Reagor, D., and F. Garzon, *Appl. Phys. Lett.* **58**, 2741 (1991).
- Roy, R., *J. Amer. Ceram. Soc.* **37**, 581 (1954).
- Rudorff, W., and D. Krug, *Z. Anorg. Allg. Chem.* **329**, 211 (1964).
- Sasaura, M. M. Mukaida, and S. Miyazawa, *Appl. Phys. Lett.* **57**, 2728 (1990).
- Schlenker, J. L., and B. K. Peterson, *J. Appl. Cryst.* **29**, 178 (1996).
- Schuegraf, Klaus K., ed., *Handbook of Thin-Film Deposition Processes and Techniques*, pp. 291-301, Noyes Publications, Park Ridge, New Jersey (1988).
- Shannon, R. D. *J. Appl. Phys.* **73**, 348 (1993).
- Shen, Zhi-Yuan, *High-Temperature Superconducting Microwave Circuits*, p xi, Artech House, Boston (1994).
- Sheng, Z. Z., and A. M. Herman, *Nature* **332**, 138 (1988).
- Sleight, A. W., *Science* **242**, 1519 (1988).
- Storm, A. R., *Mat. Res. Bull.* **5**, 973 (1970).
- Subramanian, M. A., C. C. Torardi, J. Gopalkrishnan, P. L. Gai, J. C. Calabrese, T. R. Askew, R. B. Flippen, and A. W. Sleight, *Science* **242**, 249 (1988).
- Tome-Rosa, C., G. Jakob, M. Maul, A Walkenhorst, M. Schmitt, P. Wagner, P. Przyslupski, and H. Adrian, *Physica C* **171**, 231 (1990).

- Torardi, C. C., M. A. Subramanian, J. C. Calabrese, J. Gopalkrishnan, K. J. Morrissey, T. R. Askew, R. B. Flippen, U. Chowdhry, and A. W. Sleight, *Science* **240**, 631 (1988).
- Vanderah, T. A., C. K. Lowe-Ma, and D. R. Gagnon, *J. Am. Ceram. Soc.* **77**, 3125 (1994).
- West, Anthony R., *Solid State Chemistry and its Applications*, pp. 534-537, John Wiley and Sons, New York (1985).
- Woodward, P. M., *Acta. Cryst. B.*, accepted for publication.
- Woodward, P., R-D. Hoffmann, and A. W. Sleight, *J. Mater. Res.* **9**, 2118 (1994).
- Wu, M. K., J. R. Ashburn, C. J. Torng, P. H. Hor, R. L. Meng, L. Gao, Z. J. Huang, Y. Q. Wang, and C. W. Chu, *Phys. Rev. Lett.* **58**, 908 (1987).
- Wu, X. D., R. C. Dye, R. E. Muenchausen, S. R. Foltyn, M. Maley, A. D. Rollett, A. R. Garcia, and N. S. Nogar, *Appl. Phys. Lett.* **58**, 2165 (1991).
- Young, K. H., G. V. Negrete, M. M. Eddy, J. Z. Sun, T. W. James, McD. Robinson, and E. J. Smith, *Thin Solid Films* **206**, 116 (1991).
- Young, K. H., and J. Z. Sun, *J. Appl Phys.* **70**, 3748 (1991).
- Zhang, J. Z., Chen, D. Cui, H. Lu, Y. Zhou, L. Li, G. Yang, N. Jiang, and J. Hao, *Appl. Phys. Lett.* **66**, 2069 (1995).

Appendix

Appendix

Operation of A. W. Sleight Research Group Sputtering System

1. Initial Start Up

- A. Turn on cooling water for sputtering guns and cryopump by turning orange valve handle behind the system to an approximately 45 degree angle.
- B. Turn on mechanical pump.
 - 1) Remove drive train cover.
 - 2) Turn drive wheel by hand a couple of turns to get lubricating oil into the pump.
 - 3) Replace cover; turn on power via toggle switch on front right of system control panels. Red light should come on.
- C. Turn on cryopump.
 - 1) Make sure cryopump power toggle on the system control panel is in the "on" position (red light on).
 - 2) On cryopump body, first turn on the compressor, then the cold head.
- D. Check gas cylinders.
 - 1) Must have 90 psi nitrogen (low or standard purity, orange tank) of gas in valve operation gas line for pump valves and vent valve to open and close properly.
 - 2) Must use pre-purified nitrogen (blue tank) for vent gas.
 - 3) Make sure sufficient argon (grade 4.8) and oxygen (grade 4.4), or other oxidant, is in cylinders for deposition.

If gas cylinders have enough pressure, then system will be ready to in 2-3 hours, after cryopump cools to <15 K (on cold head temperature monitor on top of sputtering system cabinet).

Note: Cryopump should be regenerated regularly during periods of regular operation, and should be shut down if system is to be idle for more than a few days.

2. Deposition Preparation

- A. Vent Chamber to Room Pressure
 - 1) Close high vacuum valve (red light off) or roughing pump valve (red light off). Both should be closed before venting.

2 Deposition Preparation (continued)

- 2) Open vent valve (red light on), allowing chamber to reach room pressure. Pre-purified nitrogen should be used.
- 3) After orange light (next to system control key) comes on, let vent gas flow for approximately one minute. Chamber should now be vented to ambient pressure.

B. Load substrate/target

- 1) Open chamber by depressing hoist toggle switch in "up" direction. Chamber top will automatically stop at upper limit of travel.
- 2) Load target in desired gun. US II gun is in position closest to the mechanical pump; Onyx gun is closest to wall. Load US gun by removing hex screws from anode cap, removing anode, then removing hex screws from ring holding target in place. Place target (1" ceramic pellet with silver paint on back, or machined 1" diameter metal wafer) with silver paint against the cathode. Replace target holding ring, then anode ring. It is a good idea to sand off the anode when changing targets.

Load Onyx gun by unscrewing the anode cap, then unscrewing target positioning ring. Place target in gun, screw holding ring back on until tight against target, and then screw on anode ring until the correct spacing is given by the anode spacing tool. This is a thin metal rod, approximately 5 in. long, with a 40° bend at each end, and is kept in the bottom right of the gray tool drawers. Screw in anode cap until the tool just fits between the anode and target.

Heater edge should be about 2 cm from gun.

- 3) To position heater, first turn on system power supply (large cabinet to the left of the vacuum chamber). Turn "Table Position" knob to position 2. Adjust direction of motion with "CW/CCW" toggle, and move heater with "speed" knob. Turn "Table Position" to 1 (off) once desired position is reached). Make sure RF power is routed to correct gun by selecting "Onyx" or "US II" on *chamber top control panel*.

2 *Deposition Preparation (continued)*

- 4) Load substrate. Mount with silver paint to heater. Check alignment of gun with respect to substrate. Attach thermocouple to heater with silver paint.

See appendix section 6 for on-axis/off-axis heater conversion.

C. Pump Down

- 1) Make sure chamber flange is clean and free of debris. Lower chamber top by depressing "down" on hoist toggle.
- 2) Open roughing valve and evacuate chamber to 20 mtorr by thermocouple gauge on top of system cabinet or capacitance manometer (LED display) on left control panel.
- 3) Close roughing valve.
- 4) Open high vacuum valve.
- 5) Turn on ion gauge to monitor background pressure. Turn "function" to .01; turn "mode" to emission. Press "filament" twice. Turn "function" to degas for a few minutes, then back to .01. Turn "mode" to auto.
- 6) Let background pressure decrease to $\sim 1 \times 10^{-5}$.

3. *Deposition*

- A. Turn on RF power supply for warm up. Cooling water to guns should be on.
- B. Turn on substrate heater. Ramp rate of 10° C/min is highest recommended. If heater will not work, check fuse in heater controller by removing front panel of cabinet, turning off power at strip, and removing fuse from backside of controller.
- C. Once at pressure, check background pressure, then turn off ion gauge.
- D. Close throttle valve (red light on) and introduce gas mixture by opening toggles at back of system. Red toggle is oxygen, black is argon, and blue is left for any other gas. Set individual pressures with valve knobs adjacent to toggles.

3. *Deposition (continued)*

- E. Once gas pressure has stabilized, depress RF power switch. Gradually turn up power, watching "reflected power" indicator. When this indicator begins to increase, tune the RF circuit by adjusting the "tune" (capacitance) and "load" (inductance) switches recursively to minimize reflected power. Turn up RF power until plasma ignites, then set to solid line for US II gun or dashed line for Onyx gun. These are only recommended values; RF can go as high as green dashed line for either gun. Red solid line is approximately 50 W. If plasma does not ignite, turn down RF, increase gas pressure, try igniting plasma again, and then reset desired gas pressure.
- F. Deposit for desired time.

4. *Ending Deposition*

- A. Gradually turn down RF power until knob is all the way down.
- B. Depress RF power switch to turn off power.
- C. Turn off sputtering gases at toggles.
- D. Turn off substrate heater by first setting to "hold", then decreasing dwell time to 0, and then setting back to "run". This will end the time the heater is held at deposition temperature, and will begin the ramp down to room temperature or anneal temperature. Cooling rate can be set as desired.
- E. Allow the heater to cool to 100 °C or less before venting chamber.

5. *System Shutdown--Overnight or Weekend*

- A. Leave cooling water on to guns and cryopump compressor.
- B. Let RF power supply run for 1 hour after deposition to cool, then turn off.
- C. High vac valve should be closed. Backfill chamber to a few torr pre-purified nitrogen to preserve targets.

6. *System Shutdown--Long Term*
 - A. Vent chamber to ambient pressure. Make sure RF power is off.
 - B. Turn off cryopump--first the cold head, then the compressor.
 - C. Turn off mechanical pump. Never turn off mechanical pump while cryopump is on, as mechanical pump pumps on various seals in the system.
 - D. Turn off cooling water at orange valve.
7. *On-axis to Off-axis Heater Conversion*
 - A. Change heater configuration.
 - 1) Disconnect heater leads from main copper wires, and remove heater from vacuum chamber.
 - 2) Remove back protective shield from heater.
 - 3) It's a good idea to sand the reflector in the heater at this time.
 - 4) Place heater back into vacuum chamber in off-axis configuration (heater top facing up, mounting rails fitting in the slots in the heater body).
 - 5) Reconnect leads, making sure no wires are touching heater body or vacuum chamber (this will blow a fuse).
 - B. Raise sputtering gun.
 - 1) Open wraparound side cover of the top of the sputtering system (above the vacuum chamber top).
 - 2) Locate the stem of the gun in use.
 - 3) A collar with an allen screw is used to set the lower limit of gun travel. Loosen this screw.
 - 4) Loosen vacuum nut (the seal where the gun passes into vacuum chamber) by twisting counterclockwise.
 - 5) Pull gun up high enough so that the spacer nut (just a swagelock nut) fits between the collar and vacuum nut.

7. *On-axis to Off-axis Heater Conversion (continued)*

- 6) Tighten vacuum nut and collar, and close wraparound cover.

C. Change thermocouple.

- 1) Remove on-axis thermocouple (long and curved).
- 2) Install off-axis thermocouple (shorter).
- 3) At the thermocouple feed through, it is necessary to reverse the connections (due to a wiring error in one of the thermocouple connectors). The correct connections are:

ON AXIS: 1-2, 2-1

OFF AXIS: 1-1, 2-2

To convert from off-axis to on-axis, reverse the above procedures.